This manuscript has been submitted for publication to JOURNAL OF CLIMATE (AMS). Please note that this manuscript has yet to undergo a second round of peer review or be formally accepted for publication. Subsequent versions of this manuscript may differ slightly in content.

# Efficient Estimation of Climate State and Its Uncertainty Using Kalman Filtering with Application to Policy Thresholds and Volcanism

J. Matthew Nicklas,[a] Baylor Fox-Kemper,[a] Charles Lawrence.[a]

[a] *Brown University, Providence, Rhode Island.*

*Corresponding author*: J. Matthew Nicklas, john_nicklas@brown.edu

ABSTRACT

We present the Energy Balance Model – Kalman Filter (EBM-KF), a hybrid model of the global mean surface temperature (GMST) and ocean heat content anomaly (OHCA). It combines an energy balance model with parameters drawn from the literature and a statistical Extended Kalman Filter assimilating observed and/or earth system model-simulated GMST and OHCA. Our motivation is to create an efficient and natural estimator of the climate state and its uncertainty. Our climate emulator has the physical rationale of an annual energy budget, and is compatible with an Extended Kalman Filter both because it forms a set of difference equations (involving 17 constants) and because climate models and historical records of GMST and OHCA follow nearly Gaussian distributions about their relevant means. We illustrate four applications: 1) EBM-KF generates a similar estimate to the 30-year time-averaged climate state 15 years sooner. 2) EBM-KF conveniently assesses annually the likelihood of crossing a policy threshold, e.g., 2°C over preindustrial. 3) The EBM-KF also approximates the behavior of an entire climate model large ensemble using only one or a few ensemble members. 4) The EBM-KF is sufficiently fast to allow thorough sampling from non-Gaussian probabilistic futures, e.g., the impact of rare but significant volcanic eruptions. Indeed, volcanic eruptions dominate the future uncertainty over the slowly growing GMST climate state uncertainty. This sampling with the EBM-KF better determines how future volcanism may affect when policy thresholds will be crossed and what a larger-than-large ensemble including future intermittent volcanism would reveal.

SIGNIFICANCE STATEMENT

The global average of the Earth's historical climate over the past 150 years can be explained by a thermal/radiation physics equation involving a small number of constants (17), atmospheric CO2, human-produced cloud-seeding aerosols, and dust from volcanic eruptions. Global mean surface temperature measurements vary around this climate state within a consistent normal distribution. This physics equation and statistical depiction allowed us to construct a simple model that can rapidly estimate the uncertainty in Earth's current climate, aid in policy discussions, and reduce ensemble modeling costs.

## 1. Introduction

What is the uncertainty in Earth's climate? From a measurement standpoint, this issue was resolved many decades ago. The instantaneous measurement of global mean surface temperature (GMST) is currently performed with average accuracy of 0.05°C (max 0.10°C) via arrays of infrared-sensing satellites and ground stations (Susskind, Schmidt et al. 2019), both of these datasets extend back to 1981 (Merchant, Embury et al. 2019), and the yearly seasonal fluctuation is easy to smooth with a running annual average. However, this GMST still has significant dynamical and random stochasticity, from processes like the 2-7 year quasi-periodic El Nino events (Hu and Fedorov 2017) and volcanic eruptions that intermittently affect climate for 1-2 years (Soden, Wetherald et al. 2002). True measurement errors also arise from sparse or inconsistently calibrated historical data and paleoproxies (Carré, Sachs et al. 2012; Emile-Geay, McKay et al. 2017; Kaufman, McKay et al. 2020; McClelland, Halevy et al. 2021). Internal variability dominates over climate-forced variability in most short-term signals, both in climate simulations and reality (Kirtman, Power et al. 2013; Marotzke and Forster 2015; Gulev, Thorne et al. 2021; Lee, Marotzke et al. 2021). By “simulations”, we refer to computationally expensive global coupled models (and occasionally to numerical weather model predictions). Variables other than GMST reveal steadier warming, such as Ocean Heat Content Anomaly (OHCA) where >90% of the anthropogenic energy anomaly is found (Cheng, Trenberth et al. 2017; Fox-Kemper, Hewitt et al. 2021; Gulev, Thorne et al. 2021; Cheng, von Schuckmann et al. 2022). Even radical reductions in global $CO_2$ emissions may not show an identifiable impact on GMST over a time scale of a few years (Szopa et al. 2021), posing a challenge for policy and assessment.

In 1935 the World Meteorological Association began reporting the "standard climate normal" as surface temperature averages of over an interval of 30 years ( $\overline{_{30}Y_n}$ in this paper’s notation, starting with 1901-1930). A 30-year window was chosen to minimize most internal fluctuations (such as El Nino) and short-term forcings such as single volcanoes (Guttman 1989). Fig. 1 shows this metric and emphasizes the 30-year span over which the average is taken. To generate continuous estimates of the climate, this 30-year average can be updated annually rather than decadally, forming a running mean (Supp. Fig. 2b). While standard climate normals and running means are straightforward and widely accepted definitions of climate, they involve lag: the most current 30-year unweighted average necessarily describes the average climate state of Earth over a window centered on 15 years ago. Weighted moving averaging can shift the center of this window closer toward the current year but some lag always remains. Moreover, anthropogenic climate change distorts standard statistical metrics:

most of the variance in recent 30-year periods derives from the trend rather than internal variability (Fig. 1). Averaging filters (such as a running mean) remove high-frequency signals that reflect year-to-year variations in global weather, as do other statistical approaches better-suited to removing frequencies above a particular cutoff (Smith 2003). The anthropogenic change beginning in the mid-1960s in Fig. 1 is similarly preserved by moving averages (running mean) or any lowpass filter / smoother. Example applications to GMST of statistical, as opposed to physical, filters commonly used in climate analysis are shown in supplemental Section B (Supp. Fig. 2, 3).

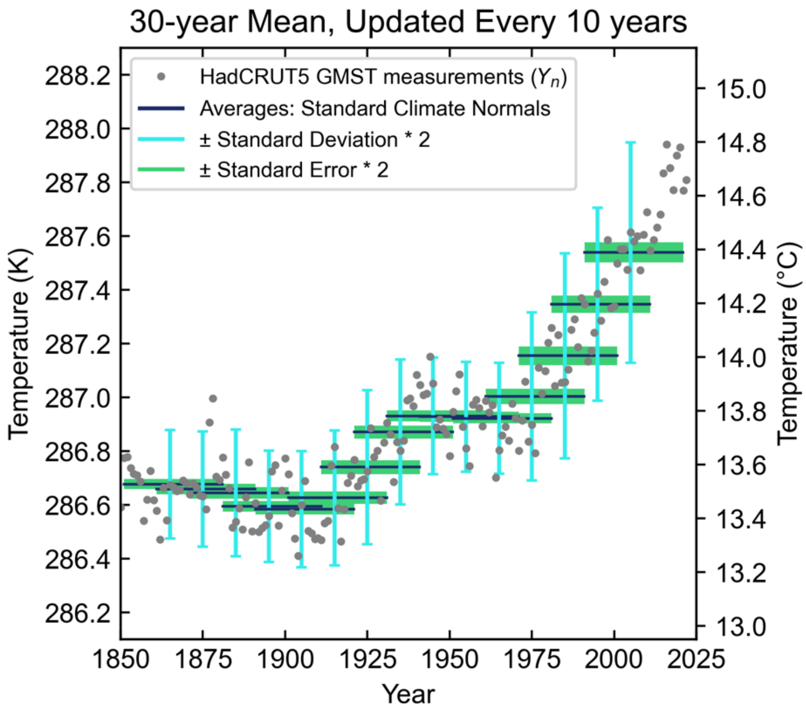


Fig. 1: Illustration of Standard Climate Normals $\overline{{}_{30}Y_n}$ (blue horizontal lines in 10-year overlapping bins) as applied to the HadCRUT5 GMST dataset (grey dots) (Morice, Kennedy et al. 2021). Twice the standard deviation (±2σ) is plotted above and below (cyan error bars), and two standard errors are also plotted (green rectangles). Note how standard deviations widen in recent decades due to the anthropogenic trend.

Policy goals often are framed via climate change staying below a particular policy threshold (e.g., 1.5°C or 2°C above pre-industrial conditions as in the Paris Agreement). Using a 30-year mean brings difficulty in determining exactly when or if a policy threshold is crossed (Lee, Marotzke et al. 2021). Policy thresholds are not system thresholds — temperature “tipping” points when the dynamics of the climate system are reorganized often abruptly or irreversibly — and so they are subject to definitional uncertainty. Relatedly, magnitudes and uncertainty ranges are meaningful only under specific averaging windows, e.g., "GMST increased by 0.85 (0.69 - 0.95) °C between 1850–1900 and 1995–2014 and by 1.09 (0.95 - 1.20)°C between 1850–1900 and 2011–2020." (Gulev, Thorne et al. 2021). Tools for assessing if a policy threshold has been crossed yet will be useful as these policy targets approach. Throughout this paper we use (a - b) notation to refer to intervals and ranges.

To overcome limited sampling of the real world, many climate studies instead investigate the climate system within globally coupled climate simulations ("coupled" refers to coupled sub-models, principally the atmosphere and ocean) or earth system models: ESMs (Meehl, Moss et al. 2014). Typically, these simulations are forced using historical records and a range of scenarios for future projections including $CO_2$ emissions, other pollutants, land use, and volcanic eruptions (Lee, Marotzke et al. 2021). The chaotic nature of weather and varying initial conditions produce an ensemble of identically-forced simulations that explore the span of outcomes consistent with forcing, such as for the CESM2 Large Ensemble (Rodgers, Lee et al. 2021), abbreviated here as LENS2 (Supp. Fig. 4). Unfortunately, each ensemble member simulation is computationally expensive and does not accurately or transparently reflect the real climate system, but only one realization of it including model errors.

Therefore, we sought an efficient and natural estimator of the uncertainty in the climate state: the EBM-KF. We combined a nonlinear energy-balance difference equation (EBM) and a statistical observation equation (KF) that brings in the available measured GMST and OHCA data, yielding a hybrid physical model – statistical filter. This data-driven climate emulator (Forster, Storelvmo et al. 2021) by construction inherits benefits from its chosen constituent models and is vastly more computational efficient than ensembles of ESMs that provide similar information. Our emulator is interpretable as a global energy budget, benefits from the mathematical similarities between an energy balance model and a Kalman filter, and allows access to proven methodologies for parameter estimation (Chen, Heckman et al. 2018; Zhang and Atia 2020 ) and uncertainty quantification (Sætrom and Omre 2013). No part of this emulator was empirically fit to the climate record: 12 of the 17 parameters within the energy-balance equation were obtained directly from literature estimates, whereas the remaining 5 parameters are inferred indirectly from assumed pre-industrial climate equilibrium and literature estimates of climate sensitivities. Our simple iterative energy-balance model has good skill at predicting the GMST and OHCA despite being by itself "blind" to all measurements (i.e., it's a "forward" model in numerical weather prediction terminology). The statistical component is an Extended Kalman Filter, which allows for incorporation of current measurements to "course-correct" under a well-understood mathematical framework. Noise covariance matrices within this statistical observation equation were constructed such that the “climate state” most closely resembles the 30-year running mean of GMST and OHCA. Hybridizing these two components yields statistical distributions of uncertainty from internal variability and a physical rationale for the filtered current climate state.

First, the EBM-KF is introduced within Section 2 in phases: the EBM in Section 2a and the structure of the Extended Kalman Filter in Section 2b. An elaboration beyond fixed assumed measurement uncertainty is detailed in Section 2c. The scope of EBM-KF is expanded to future projections including volcanic eruptions in Section 2d. Then in Section 3, EBM-KF is illustrated on four applications to historical and future climate. Section 3a shows that it estimates the 30-year mean climate normal every year, including the latest observations and without lag. Section 3b shows how it can be used to assess the probability that a policy threshold has been crossed in any particular year. Section 3c shows how it can be used to estimate the ensemble mean of an ESM Large Ensemble from only one ensemble member. Section 3d shows that the EBM-KF is sufficiently fast to allow high-density sampling of non-Gaussian probabilistic futures, e.g., directly sampling over highly intermittent distributions of future volcanic eruptions. Section 4 discusses these results, some cautionary remarks, opportunities for extension, and application to policymaking. Section 5 concludes. Extensive appendices and supplementary material convey additional detail. Throughout, a 2σ or approximately 95% confidence interval is used, indicating the *extremely likely* range in IPCC terminology.

## 2. Methods

### *a. Energy-Balance Model*

The energy-balance model is constructed by envisioning a uniform planet and capturing the principal atmospheric and surface energy fluxes (Budyko 1969; Sellers 1969). This model is "blind" with respect to observations and is inspired by other energy-budget models illustrating quantitative skill (Hu and Fedorov 2017; Kravitz, Rasch et al. 2018) at approximating both GMST and the 30-year running mean. The model includes two layers: a surface layer including thermally active soil and 86m of ocean water depth (with temperature approximating GMST), and a deep ocean layer reaching (1141+86)m depth that exchanges energy (part of OHCA) with the surface layer (Gregory 2000). These depths are chosen based on heat capacity estimates and are unrelated to observational oceanographic traditions. The overall energy fluxes into the model layers are as follows:

$$\frac{T_{n+1}-T_n}{k} C_{surf} = G_0^\star * \widetilde{d}_n * f_{\alpha A}(T_n) * f_{\alpha S}(T_n) - j^\star * \widetilde{g}_n * f_{H2O}(T_n) - \gamma * (T_n - \theta_n - \zeta) \quad (1)$$

$$\frac{\theta_{n+1}-\theta_n}{k} C_{deep} = \gamma * (T_n - \theta_n - \zeta) \quad (2)$$

$$H_n = (T_n - T_{1850}) * C_{surf0} + (\theta_n - \theta_{1850}) * C_{deep} \quad (3)$$

$T_n$ is GMST in calendar year n (e.g. 2000), whereas $\theta_n$ is the potential (or conservative) temperature of the deep ocean in that same year, and $H_n$ is OHCA including both that deep ocean layer and the surface ocean (McDougall, Barker et al. 2021). Closely related variables to GMST, such as Global Surface Air Temperature (GSAT), differ only from GMST by measurement and slightly in uncertainty (by less than our confidence intervals) but not systematically (Gulev et al. 2021). For example, GMST is easier to measure in the past, while GSAT is more easily found from future model projections, so here we do not distinguish between them. The time unit $k$ is 1 year, matching the time step of this iterative difference equation model. On the right side of the equation, both the shortwave radiative flux and longwave radiative flux take the same form: (source $G_0^\star$, $j^\star$) * (prescribed attenuation: $\widetilde{d}_n$, $\widetilde{g}_n$) * (attenuation function with feedback: $f_?(T_n)$). The overall surface heat capacity, $C_{heat}$, is 17 ± 7 W (year) $m^{-2}$ $K^{-1}$, obtained from modeling / timeseries analysis (Schwartz, 2007), including 11.7 W (year) $m^{-2}$ $K^{-1}$ or 86m of surface ocean, while there is a separate deep ocean heat sink with capacity 155.7 W (year) $m^{-2}$ $K^{-1}$ or 1141m (Geoffroy, Saint-Martin et al. 2013; Hall and Fox-Kemper 2023). $G_0^\star$ is the extraterrestrial radiance at 340.1 W/$m^2$ (optionally allowed to vary from 340.06 to 340.48 from Coddington (2017): variations are found to be insignificant to the climate). $\widetilde{d}_n$ is the prescribed shortwave radiation attenuation due to volcanic dust (values from Sato (1993), Vernier (2011), and NASA (2018)), $f_{\alpha A}(T_n)$ is the additional atmospheric shortwave attenuation due to cloud albedo incorporating anthropogenic cloud-nucleating aerosols $AC_n$, while $f_{\alpha S}(T_n)$ is the surface shortwave attenuation due to ground albedo. Infrared heat emitted from the surface is $j^\star = \sigma_{sf} T_n^4$, the ideal Planck black body radiation. $\widetilde{g}_n$ is the prescribed longwave attenuation due to $CO_2$ and other greenhouse gasses, and $f_{H2O}(T_n)$ is the additional atmospheric longwave attenuation due to water vapor and other gasses parameterized as a function of GMST. Both $AC_n$ and $\widetilde{g}_n$ are taken from Forster et. al. (2023). Several of these terms were defined to satisfy the constraints of the climate feedbacks presented in the IPCC AR6 (Forster et al. 2021; particularly Table 7.10), and all coefficients were based on observational and modeling literature values, typically with energy fluxes measured from satellites and temperature feedback coefficients determined from model results (full derivation in Appendix A). Because the Planck radiation requires absolute temperatures, we use degrees Kelvin in model calculations and convert to °C. OHCA is also approximately convertible to thermosteric sea level rise, via the 0.0121 cm/ZJ factor from analysis of 1995 to 2014 (AR6 cross-chapter box 9.1). With this factor, the estimated thermosteric sea level rises we find are consistent with observations and projections; the EBM also estimates sea level rise in this manner (Fox-Kemper, Hewitt et al. 2021). The two negative albedo attenuations $f_{\alpha A}(\mathrm{T_n}) * f_{\alpha S}(\mathrm{T_n})$ are expressed relative to 287.5K (14.35°C), the temperature in 2002. $\zeta = 10°C$ is an equilibrium temperature difference between the surface layer and deep ocean, arising because the global ocean is thermally stratified. $\gamma$ is the thermal conductivity or "efficiency" between layers of the ocean, taken from Geoffroy (2013) to be 0.67 $W/m^2/K$, the average from the CMIP5 models. The form of this parameterization of deep ocean temperature exchange follows recent work in emulating ocean heat uptake, ignoring "efficacy factor" heat loss (Gregory 2000; Winton, Takahashi et al. 2010; Geoffroy, Saint-Martin et al. 2013; Emile-Geay, McKay et al. 2017; Palmer, Harris et al. 2018).

Measurements of temperature were obtained as relative anomalies (GMST from HadCRUT5 (Morice, Kennedy et al. 2021), OHCA from Zanna et al. (2019)), and the model also assumes a preindustrial (1850) GMST of 286.7K (13.55°C), which allows the 1960-1990 "standard climate normal" of GMST HadCRUT5 measurements to fall within the range (13.7°C - 14°C) given by Jones and Harpham (2013). This choice is important regarding the determination of many nonlinear feedback functions and coefficients affecting the surface layer (eq. 5 below), particularly with respect to the Planck feedback. Similarly, the deep ocean temperature was chosen to be 276.65K in 1850, such that current deep ocean potential temperatures are about 3.8°C, but this choice only sets the equilibrium temperature difference $\zeta$, and the chosen energy balance model is linear with respect to $\theta_n$.

Overall, the blind (forward) energy-balance model (orange dashed line in Fig. 2) has 3 yearly forcing inputs ($[\mathrm{eCO_2}]_n, AOD_n, AC_n,$ and optionally $\mathrm{G}_0^\star$ ) and 17 irreducible parameters (including 1 inferred exponent, 4 inferred $\beta$ coefficients, 3 heat capacities, and 3 reference temperatures). The deep ocean potential temperature $\theta_n$ is recalculated at each time step from the GMST ($\mathrm{T_n}$) and the OHCA ($H_n$), and then these two terms are updated:

$$\theta_n = (H_n - (T_n - T_{1850}) * C_{surf0})/C_{deep} + \theta_{1850} \tag{4}$$

$$T_{n+1}=T_n+\frac{G_0^\star\ 0.758 * 9.068}{C_{surf}\ (AOD_n + 9.73)}\left(1+\beta_2(T_n\text{-}287.5) + \frac{AC_n - AC_{2002}}{G_0^\star\ \widetilde{d_{2002}}\ 0.834}\right)\left(1+\beta_3(T_n\text{-}287.5)\right)$$

$$-\frac{\sigma_{sf}\beta_1}{C_{surf}}(T_n)^{2.39}\left(1\text{-}\beta_0 \log_{10}([eCO_2]_n)\right) \quad -\frac{\gamma}{C_{surf}}(T_n - \theta_n - \zeta) \tag{5}$$

$$H_{n+1} = (T_{n+1} - T_{1850}) * C_{surf0} + \gamma * (T_n - \theta_n - \zeta) + (\theta_n - \theta_{1850}) * C_{deep} \tag{6}$$

All coefficients are constant in time, and assume the temperatures are in Kelvin, $eCO_2$ concentrations are in ppm, aerosol optical depth is unitless, and both $AC_n$ and the optional $G_0^\star$ are in $W/m^2$. For this model, the OHCA ($H_n$) is calculated in units of W*year/$m^2$ on an average of the Earth's surface, and then converted to ZJ within the ocean by multiplying by a factor of 11.42 = 3.154e7 s/year * 5.101e7 $m^2$ / Earth surface * 0.71 ocean/surface. This time-step function (4-6) and its partial derivative (see Appendix A4) will become critical parts of the Kalman filter: (9, 10) below.

This blind EBM model had good skill at predicting the GMST with $r^2$=0.902 when compared to the HadCRUT5 GMST timeseries (Morice, Kennedy et al. 2021), and OHCA with $r^2$=0.907 when compared with the inferred temperature history (Zanna, Khatiwala et al. 2019), as is demonstrated by the dashed orange lines in Fig. 2. The blind EBM has a comparably high correlation ($r^2$=0.890) with the 30-year running mean (i.e., the climate normal) of the HadCRUT5 GMST, indicating that this forward energy balance model also has skill in reproducing the climate state as determined by standard approaches, with departures due to volcanic eruptions. Thus, most observed climate change can be explained by the literature-based blind, forward EBM and measurements of greenhouse gas and stratospheric aerosol concentrations, consistent with recent forward-EBM applications (Hu and Fedorov 2017; Kravitz, Rasch et al. 2018). The distribution of residuals in the GMST record from either the 30-year running mean or the EBM has small bias and skewness (see Supp. Fig. 5). These residuals' kurtosis is slightly less than Gaussian to accommodate measurement uncertainty, as discussed in Section 3a in relation to Fig. 3 & 4. So the "weather" or "noise" empirical probability density function combining residuals and measurement uncertainty is very nearly Gaussian, and thus amenable to treatment by the Kalman filter framework (see section 2b). The Fig. 2 comparisons were made without any assimilated data, illustrating that the EBM physics alone has skill in reproducing aspects of the GMST and OHCA records. Tuning the EBM parameters may further improve skill, but the EBM is only the forward component of the hybrid data-assimilating Kalman Filter model described in the next section. The combined system is the focus of this paper.

*b. EBM-Kalman Filter: A Weighted Average of Energy Balance and Measurements*

While similar algorithms were developed in the 1880s by Thorvald Nicolai Thiele (Lauritzen 1981; Lauritzen and Thiele 2002), Kalman filtering rose to prominence due to its use in the Apollo navigation computer as proposed by Ruslan Stratonovich (1959; 1960), Peter Swerling (1959), Rudolf E. Kálmán (1960), Richard S. Bucy (1961), and implemented by Stanley Schmidt (1981). Versions of this statistical filter are universally used in aerospace guidance systems (Grewal and Andrews 2001), aspects of numerical weather prediction (Houtekamer and Mitchell 1998; Kalnay 2002; Annan, Hargreaves et al. 2005), and recently popularly as Ensemble Kalman filters (which use a Monte Carlo approximation via simulations in high-dimensional space, see below). Ensemble Kalman filters (not to be confused with Extended Kalman filters, the subject of this paper) have been instrumental to $20^{th}$ century reanalysis (Compo, Whitaker et al. 2011) and last millennium reanalysis projects (Hakim, Emile-Geay et al. 2016) of global atmospheric circulation. In the Ensemble Kalman Filter, observations sample the full gridded weather patterns (a space with hundreds to millions of dimensions) within an ensemble of ESMs. Despite the success of Ensemble Kalman filters, *Extended* Kalman filters are ineffective as the sole data assimilation tool for atmospheric weather patterns (Bouttier 1996). While many local weather processes do not sample from a Gaussian distribution, the central limit theorem states that taking the average of many independent non-Gaussian samples will produce a mean that approximates a Gaussian distribution. This is the case for both annual GMST (Montgomery and Runger 2013), which is the average of many non-Gaussian regional and daily weather patterns (Quevedo and Gonzalez 2017). Likewise, while annual OHCA is largely constrained by the subtropical pycnocline depth (Newsom, Zanna et al. 2023), it too is comprised of numerous regional and seasonal patterns (Hummels, Dengler et al. 2013; Cheng, Trenberth et al. 2017; Huguenin, Holmes et al. 2022). In this case of *global* GMST and OHCA, an Extended Kalman filter works because both measurement and dynamical noise are approximately Gaussian (to be verified in Section 3), and the energy-balance equation (Section 2a) has a continuous and bounded gradient (see Appendix A4), so it can be locally linearized. Careful construction of the EBM with $T^2$ in the shortwave term and $T^{2.39}$ in the counteracting longwave term in (Eqs. 1 & 5) ensures the derivative (Eqs. A37-41) does not change significantly over the relevant range of temperatures (286 - 291)K, effective $CO_2$ concentrations (278 - 2000) ppm, AOD (0 - 0.15), and $\tilde{q}_n$ anthropogenic cloud forcing (-1 - 0) W/m$^2$. This approximate linearity means that more complex realizations of the Kalman filter, particularly the Unscented Kalman Filter (Julier and Uhlmann 1997; Wan and Van Der Merwe 2000) are not necessary (see Supplement Section C). Thus, the EBM-Kalman Filter (EBM-KF) can be built from an Extended Kalman Filter combined with an Energy Balance Model.

In-depth derivations and tutorials for constructing Kalman filters have been published elsewhere (Miller 1996; Lacey 1998; Särkkä 2013; Benhamou 2018; Youngjoo and Hyochoong 2018; Ogorek 2019). Here we describe enough for basic intuition, although page 281 of Kalnay (2002) may be more familiar. Initially, there is some estimated *state vector* (GMST and OHCA within this paper) $\hat{\mathbf{x}}_{\mathbf{n-1}}$ and a Gaussian uncertainty envelope around this vector defined by a *state covariance matrix* $\mathbf{P_{n-1}}$. These can be projected *a priori* (without observations) into the future using a *dynamic model Jacobian matrix* $\boldsymbol{\Phi}$ (for our climate system this is extended to the function F (7), which is just the forward energy balance model equations (3)-(6)). The projected covariance enlarges by an additional *assumed model error covariance* $\mathbf{Q}$, yielding $\mathbf{P_{n|n-1}}$ (8). To arrive at *a posteriori* (including observations) information a *measurement vector* $\mathbf{y_n}$ is considered (9). The probabilistic range of discrepancies between $\boldsymbol{\Phi}\hat{\mathbf{x}}_{\mathbf{n-1}}$ and $\mathbf{y_n}$ is given by the *innovation covariance matrix* $\mathbf{S_n}$, which is the sum of $\mathbf{P_{n|n-1}}$ and an *assumed measurement covariance* $\mathbf{R}$ (10). The *a posteriori estimate* for the state $\hat{\mathbf{x}}_{\mathbf{n}}$ is found by taking a weighted average of $\boldsymbol{\Phi}\hat{\mathbf{x}}_{\mathbf{n-1}}$ and $\mathbf{y_n}$ (12), with the weight on $\mathbf{y_n}$ given by $\mathbf{P_{n|n-1}}(\mathbf{S_n})^{-1}$, a product known as the *Kalman gain* (11). To reflect the greater certainty in the state vector because of this correction, $\mathbf{P_n}$, the *a posteriori covariance matrix*, is $\mathbf{P_{n|n-1}}$ shrunk by a factor of **I**-minus-the-Kalman-gain (13). Within the context of Bayesian probability, the *prior distribution* is given by projecting $\mathcal{N}(\hat{\mathbf{x}}_{\mathbf{n-1}}, \mathbf{P_{n-1}})$ into the future using the Jacobian matrix $\boldsymbol{\Phi}$, which is multiplied by the support of $\mathbf{y_n}$ to give a *posterior distribution* $\mathcal{N}(\hat{\mathbf{x}}_{\mathbf{n}}, \mathbf{P_n})$.

$$\Phi_n = \frac{\partial \mathbf{F}(x;u_n)}{\partial x}\Big|_{x=\hat{x}_{n-1}} \qquad \text{linearization at timepoint n} \tag{7}$$

$$\begin{cases} \boldsymbol{x_n} = \mathbf{F}(x_{n-1};u_n) + w_n & \text{dynamic model, error: } \quad \mathrm{Q} = \mathrm{Cov}(w_n) \\ \boldsymbol{y_n} = \boldsymbol{x_n} + v_n & \text{measurements, error: } \quad \mathrm{R} = \mathrm{Cov}(v_n) \end{cases} \tag{8}$$

$$\hat{\boldsymbol{x}}_{n|n-1} = \mathbf{F}(\hat{\boldsymbol{x}}_{n-1};u_n) \qquad \text{a priori estimated state projection} \tag{9}$$

$$\mathrm{P}_{n|n-1} = \Phi_n \mathrm{P}_{n-1} (\Phi_n)^T + \mathrm{Q} \qquad \text{a priori state variance projection} \tag{10}$$

| | | |
|---|---|---|
| $\boldsymbol{c}_n=\boldsymbol{y}_n-\hat{\boldsymbol{x}}_{n\vert n-1}$ | innovation residual | (11) |
| $S_n=P_{n\vert n-1}+R_n$ | innovation covariance | (12) |
| $K_n=P_{n\vert n-1}(S_n)^{-1}$ | Kalman gain | (13) |
| $\hat{\boldsymbol{x}}_n=\hat{\boldsymbol{x}}_{n\vert n-1}+K_n\mathbf{c}_n$ | a posteriori estimated state | (14) |
| $P_n=(\mathbf{I}-K_n)P_{n\vert n-1}$ | a posteriori state covariance | (15) |

For the climate state, we consider an ideal two-dimensional pair of GMST and OHCA: $x_n = [T_n\,, H_n]$. Throughout this paper, we use brackets to show matrices. If $\mathbf{y_n}$ is an indirect measurement of the state vector $\mathbf{x_n}$ (for instance GMST and OHCA approximated by a set of point measurements across the globe), an observation (a.k.a. emission) matrix **H** further complicates the procedure (details in the references above). Here we consider only "observations" of GMST and OHCA making mapping and interpolation errors implicit and the observation matrix $\mathbf{H} = \mathbf{I} = 1$, and we use italics to indicate this choice.

The abstract unknown state $\boldsymbol{x_n}$ is the climate state of GMST and OHCA, filtering out weather and internal variability. The noisy measurements $\boldsymbol{y}_n = [Y_n, \psi_n]$ are the yearly time series of GMST and OHCA, and $\hat{\boldsymbol{x}}_n = [\hat{T}_n\,, \hat{H}_n]$ is the estimate of the unknown 2-dimensional climate state, expressed in degrees Kelvin and $\frac{W\,yr}{m^2}$. The energy-balance model F (8) governing $\hat{T}_n$ is nonlinear (with $T^2$ and $T^{2.385}$ terms due to albedo and Planck feedbacks) (Friedrich, Timmermann et al. 2016), which necessitates an Extended Kalman filter: the *a priori* estimated state projection (9) is given by (3,5) above and $\Phi_n$ for the *a priori* state covariance projection (10) is a time-varying linearization (4,6). This energy-conserving difference equation thus resembles a first-order Taylor series approximation of a differential energy-balance model (if discretization errors are considered part of the tendency), or the integral form of a conservative discretization in time (if shortwave and longwave fluxes are taken as a model for their time-integrated value), and the Kalman Filter re-approximates a GMST and OHCA climate state every year. The initial estimated state uncertainty is intentionally overestimated at $P_{1850}=\begin{bmatrix} 1K^2 & 1\,K\frac{W\,yr}{m^2} \\ 1\,K\frac{W\,yr}{m^2} & 20\,\left(\frac{W\,yr}{m^2}\right)^2 \end{bmatrix}$ and then $P_n$ rapidly converges (within 15 years) in the EBM-KF to $P_{1865}=\begin{bmatrix} 0.0017\,K^2 & 0.035\,K\frac{W\,yr}{m^2} \\ 0.035\,K\frac{W\,yr}{m^2} & 4.0\,\left(\frac{W\,yr}{m^2}\right)^2 \end{bmatrix}$, and then continues to slowly shrink with time as more accurate measurements are made. For convenience we form confidence intervals for GMST and OHCA climate state by taking twice the square root of the diagonal elements of $P_n$. Both are symbolized as $2\sqrt{P_n}$ in context. For instance,

$$\text{95\% CI of GMST in 1965: } \hat{\mathrm{T}}_{1865} \pm 2\sqrt{\mathrm{P}_{1865}} = 286.66\mathrm{K} \pm 2\sqrt{0.0017\mathrm{K}^2} = 286.66 \pm 0.07\mathrm{K} \quad (16)$$

Similarly, we use the diagonal elements of $S_n$ to form confidence intervals of next-year measurements about $\hat{\boldsymbol{x}}_{n|n-1}$. The extended Kalman Filter implicitly assumes that Gaussian "model" noise is added to this climate state at each time step, and additional Gaussian "measurement" noise causes the climate state to emit annual weather.

The EBM-KF climate state $\hat{\boldsymbol{x}}_{\boldsymbol{n}}$ and state covariance $\mathrm{P}_n$ only access information from the measurements taken prior to and at year $n$: $\{\boldsymbol{y}_{1850}, \boldsymbol{y}_{1851}, \dots \boldsymbol{y}_n\}$. This past-to-present Kalman Filter (7-15) can be extended into a RTS smoother (Rauch, Tung et al. 1965) by additional steps (see Supp. Section A), which melds information from all measurements in the time window $\{\boldsymbol{y}_{1850}, \boldsymbol{y}_{1851}, \dots \boldsymbol{y}_{2022}\}$into each re-estimated state $\hat{\hat{x}}_n$ and state covariance $\hat{\hat{P}}_n$ by running backward from the latest EBM-KF state estimates ($\hat{\boldsymbol{x}}_{\boldsymbol{2022}}$ and $\mathrm{P}_{2022}$). In the 1850 to present application, this extension has little effect on $\hat{\hat{x}}_n$ (see Supp. Fig. 1), but there is more certainty in this state: $\hat{\hat{P}}_n$ shrinks relative to $P_n$ (see Supp. Fig. 13) by factors of 2.25 and 2.84 for the GMST and OHCA components respectively.

In summary, the Extended Kalman filter projects forward one year into the future based on the unbalanced fluxes of the energy balance model equation, and then takes a weighted average of this projection with the annual GMST measurement (the data assimilation increment). Thus, even though the EBM conserves energy (by construction), the combined EBM-KF does not, unlike other alternative data assimilation approaches (Wunsch and Heimbach 2007). The state estimates from this EBM-KF (in navy blue in Fig. 2) often lie between the blind EBM (in dashed orange in Fig. 2) and the annual temperature measurements (scattered gray dots in Fig. 2), a corrective effect that can be seen most clearly within the GMST measurements in Fig. 2a from 1900 to 1945 and within the OHCA measurements in Fig. 2b from 1940 to 1970. It is possible for the EBM-KF state estimates to escape these bounds for a short time, for instance from 1945 to 1950 in Fig. 2a or after 2007 in Fig 2b. Both the "blind" EBM predictions $[\tilde{T}_{n+1}, \tilde{H}_{n+1}] = \boldsymbol{F}(\tilde{T}_n, \tilde{H}_n, u_n)$ and EBM-KF state estimates $\hat{\boldsymbol{x}}_n = [\hat{T}_n, \hat{H}_n]$ dip down with each major volcanic eruption within the AOD record (see Fig. 10 in the discussion, Section 4). These volcanic dips are far more pronounced for the GMST component than for OHCA (see Fig. 2) and are present only as flat spots in the deep ocean potential temperature curve (see Supp. Fig. 7).

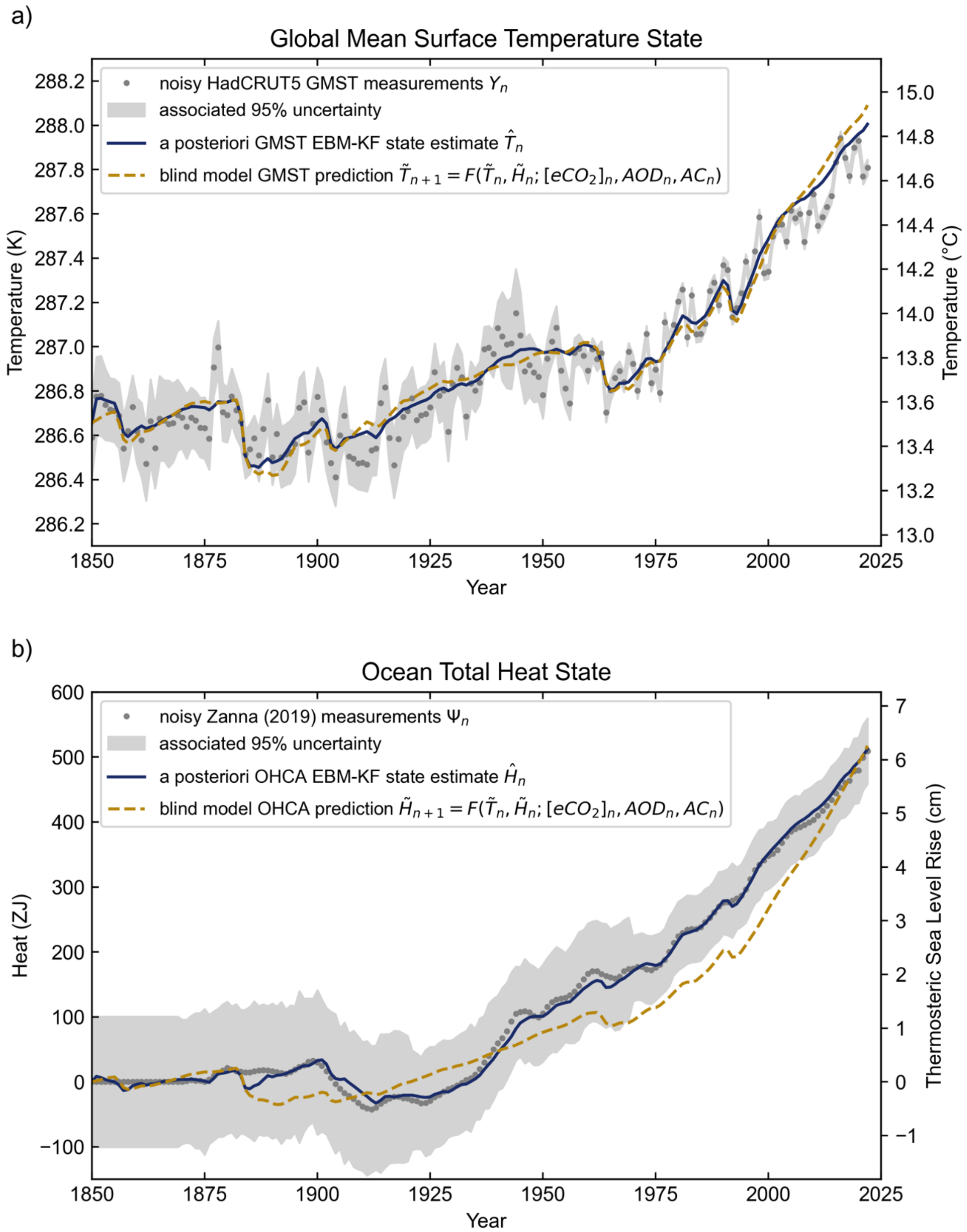


Fig. 2: Behavior of the EBM-KF state in relation to blind EBM projections and the stochastic measurements of GMST and OHCA. Panel a) shows GMST prediction and b) the OHCA prediction. The blind model (dashed orange) and Kalman filter state estimate (navy blue) use EBM dynamics to project from the previous state to the current state, but the state estimate also assimilates observations (grey dots; GMST from HadCRUT5 (Morice, Kennedy et al.

2021) and OHCA from Zanna et al. (2019)). Incorporation of these observations makes only small modifications to the EBM-KF's GMST state in a), whereas in b) there is an impressive difference between the blind EMB's OHCA projections and the EBM-KF's OHCA state - the latter sticks close to observations.

*c. Selection of Model Uncertainty and Time-Varying Measurement Uncertainty*

Fig. 2 also demonstrates the accuracy associated with each of the temperature measurements. The uncertainty in the climate state $P_n$ automatically responds to unexpected values of the measured temperature (Wunsch 2020). The HadCRUT5 GMST decreases in reported measurement standard deviation from 0.079K in the 1850-1879 window to 0.017K in the 1990-2019 window (Morice, Kennedy et al. 2021), primarily reflecting a lack of observations in the Southern hemisphere before the satellite age. The inferred deep ocean heat content taken from a hybrid model-observation reconstruction (Zanna, Khatiwala et al. 2019) has a very wide confidence interval before the introduction of modern sampling methods in the 1970s. We choose to use the Zanna et al. (2019) hybrid product due to its long duration of OHCA estimates (based on surface forcing in early years) rather than the shorter direct measurement products (e.g., (Ishii, Fukuda et al. 2017)), although both could be assimilated simultaneously within EBM-KF if desired (as discussed in Section 4c). Our EBM-KF incorporates these known physical measurement uncertainties in the HadCRUT5 measurements of GMST and the OHCA reconstruction as $R_n^{var}$. The total assumed measurement covariance $R_n$ (in Eq. 12) is composed of two components: the time-varying physical measurement uncertainty $R_n^{var}$, and the constant uncertainty reflecting internal variability due to chaos $R^{const}$. We assume that $R_n^{var}$ is diagonal and simply sum the two variance matrices to obtain a time-varying value:

$$R_n = R_n^{var} + R^{const} \tag{17}$$

The realization of the EBM-KF shown in Fig. 2 also has a measurement uncertainty $R^{const}$ that is constant in time and based on the [HadCRUT5's GMST, Zanna OHCA] residual co-variance with respect to their 30-year running means. In other words, we computed

$$R^{const} = \mathrm{Cov}(\boldsymbol{y_n} - {}_{30}\overline{\boldsymbol{y}}_{\boldsymbol{n}}) = \begin{bmatrix} 0.01107\,K^2 & 0.04627\,K\,\frac{W\,yr}{m^2} \\ 0.04627\,K\,\frac{W\,yr}{m^2} & 1.17278\,\left(\frac{W\,yr}{m^2}\right)^2 \end{bmatrix} = 30*Q \tag{18}$$

The assumed model covariance, Q (see Eq. 10), is set to $R^{const}/30$ to emulate the 30-year running average definition of climate state (Guttman 1989), thus we assume that the random noise contained within the climate model has a variance that is 1/30th as large as the variance in the "weather" measurements. By this simple method, the data-assimilating EBM-KF is tuned to match the "standard climate normal", as a 30-member sample average has a variance 1/30th as large as the annual measurements' variance (assuming yearly anomalies are uncorrelated). Variance in these annual measurements arises due to chaos within the climate system, so this $R^{const}$ contribution to the model and measurement uncertainty would exist even if all measurements could be made with arbitrary accuracy.

*d. Non-Gaussian Future Projection and Sampling of Volcanic Activity*

The EBM-KF can project into the future, given greenhouse gas and aerosol concentrations, without any new measurements using only the forward model to obtain *a priori* estimates (Eq. 9 & 10). Then the *a posteriori* state and *a posteriori* covariance are set equal to the *a priori* (projected) state and *a priori* covariance, i.e., an *a posteriori* unaffected by any new observations: $\mathbf{\hat{x}_n}=\mathbf{F}(\mathbf{\hat{x}_{n-1}})$ and $P_n=\Phi_n P_{n-1}(\Phi_n)^T+Q$ . Future projections along the shared socioeconomic pathways (SSPs) for the EBM-KF also require the concentrations of greenhouse gasses including carbon dioxide ($[CO_2]_n$), stratospheric aerosol optical depth due to volcanic dust and human emissions ($AOD_n$), and reflective flux from anthropogenic clouds ($AC_n$). ESMs typically simulate the carbon cycle and thus find $CO_2$ concentrations from $CO_2$ fluxes, but our EBM-KF does not have this capability. Future greenhouse gas concentrations and anthropogenic cloud forcings are instead taken from a conversion of anthropogenic fluxes by the MAGIC7.0 carbon cycle emulator (Meinshausen, Nicholls et al. 2020), as reported by Smith (Smith, Forster et al. 2021). For instance, SSP1-2.6 and SSP3-7.0 are shown in Fig. 8 & 9, which flank the most likely result of current environmental policies (Pielke Jr, Burgess et al. 2022). Projection of anthropogenic forcings from Nazarenko et. al. (2022) using the NASA GISS ESM yield very similar future curves (not shown).

Future volcanic eruptions require modeling as well. Volcanic eruptions determining $AOD_n$ are inherently stochastic, but the time intervals between eruptions can be approximated using exponential distributions (Papale 2018). In standard ESMs, future volcanism is usually included by a steady "background" volcanism, neglecting volcanism's intermittency and the associated exponential distributions. Even though the EBM-KF assumes Gaussian error and thus cannot include exponential distributions in the same way as measurement and internal chaotic variability, it is so computationally inexpensive that it can be rerun to sample over complex non-Gaussian distributions. This ability to include future volcanoes illustrates a major advantage of this system: thousands of future scenario inputs can be generated and utilized within minutes on a laptop, while each ESM of the LENS2 ensemble took over a week to run on a supercomputer (roughly a billion times more effort per ensemble member) limiting the ensemble size and thus motivating only a background constant level of volcanism to isolate the stochastic effects of weather with repeated simulations. No single exponential distribution fits well to the observed series of volcano eruption intervals, so an exponential mixture with two components was found to be the best fit to the data using the decomposed normalized maximum likelihood (Okada, Yamanishi et al. 2020). See Appendix B for further details. While these distribution approximations may be improved by better volcanology, they provide reasonable future aerosol optical depths to be fed into the EBM-KF.

# 3. Results

## *a. EBM-KF Climate State (1850-Present) as an Estimator of the 30-year Running Average*

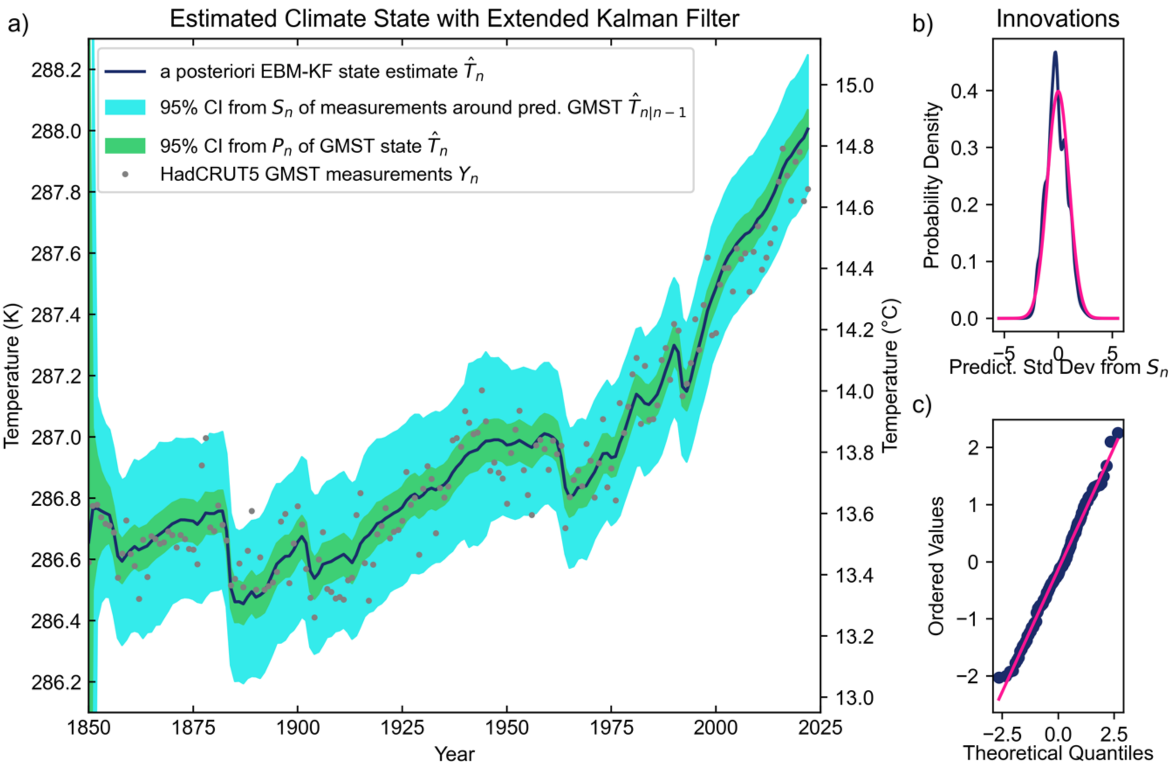


Fig. 3: EBM-KF and associated uncertainties. a) The EBM-KF climate state estimate (navy blue line) is drawn with a 95% or *extremely likely* confidence interval (light green area) from the GMST-GMST component of $2\sqrt{P_n}$. Annual-mean HadCRUT5 GMST measurements are assimilated (gray dots). A 95% confidence interval (or 95% CI in light blue) from the innovation covariance (GMST-GMST component of $2\sqrt{P_n}$ or forecast uncertainty) is drawn

around the a priori estimated GMST state projection $\hat{T}_{n|n-1}$, showing where the Kalman filter expects the subsequent year's temperature measurement to be. b) The deviation between the projected climate state (pink) and Gaussian mixture of measurements with associated uncertainty (purple), with horizontal axis labeled with the ideal distribution from the square root of the GMST-GMST component of the innovation covariance. c) Quantile-quantile plot of these innovations.

A primary product of this paper is the EBM-KF climate state. Recall that the forward EBM uses published literature values: this is not an empirical fit to GMST and OHCA data, but rather the EBM-KF assimilates these data. We first examine the GMST component $\hat{T}_n$ of the Kalman-filtered climate state $\hat{\boldsymbol{x}}_{\mathrm{n}}$. There are two distinct Gaussian distributions relevant to climate science: the uncertainty in the current GMST climate state, as graphed in narrow green envelope in Fig. 3a, and the uncertainty window of possible next-year GMST measurements, as graphed in the light blue wider envelope in Fig. 3a. Further examination of the difference between projected states $\hat{T}_{n|n-1}$ and *a posteriori* estimated states $\hat{T}_n$ reveals that in any individual year after 1855, assimilation of the GMST measurement only shifts the a priori GMST state projection $\hat{T}_{n|n-1}$ by ±0.007K on average, range (-0.0198 - 0.0224)K. This update value is miniscule compared with the GMST adjustment in $\tilde{T}_n$ from the blind, forward EBM contribution of forced climate state change of ±0.0206K annually, up to (-0.1909 - 0.0533)K in a single year. However, as in Fig. 2, repeated small increments of this magnitude by consistently lower or higher than expected GMST measurements can drift $\hat{T}_n$ away from $\tilde{T}_n$ by as much as (-0.0858 - 0.0620)K. he measurements have nearly equal warming and cooling contributions to the underlying $\hat{T}_n$ climate state, forming the expected Gaussian distribution as demonstrated over the entire timeseries in Fig 3b and in every 50-year period in Supp. Fig. 8. The GMST observations since 2000 slightly cool the EBM (right column in Supp. Fig. 8), which could be rectified with parameter adjustment, see Section 4c. After an initial convergence period of about a decade, the GMST-GMST component of the state uncertainty $2\sqrt{\mathrm{P}_n}$ slightly shrinks from ~0.067K in the late 1800s to 0.063K in the early 2000s. Meanwhile the GMST-GMST innovation covariance, which we also term forecast uncertainty, $2\sqrt{\mathrm{S}_n}$ converges from ~0.26K to 0.224K. The empirical projection probability distribution (a Gaussian mixture of all measurement uncertainties relative to the EBM-KF predictive distribution) and ideal probability distributions (the Gaussian EBM-KF predictive distribution) closely match (Fig. 3b), confirming that the annual measurements of GMST can be interpreted as Gaussian noise around an underlying climate state approximating the "standard climate normal" 30-year mean. In the quantile-quantile plot (Fig. 3c), the innovation data follows a straight line, showing good support for the Kalman filter assumption of Gaussian residuals.

The EBM-KF GMST climate state estimate over 1850 to present is not substantively different from the 30-year moving average except for the impact of volcanoes (see Fig. 10a, $r^2$=0.922), thus $\widehat{T}_n \approx \overline{{}_{30}Y_n}$. Both depart from LENS2 in the interval from 1940 – 2000 (see Fig. 10a, $r^2$=0.902 between EBM-KF and LENS2), more so than the EBM-KF state estimate of GMST departs from the blind, forward EBM (Fig. 2, $r^2$=0.992). The performance of the GMST and OHCA portions of EBM-KF model do vary; the most noticeable biases are that the blind OHCA is significantly corrected toward the Zanna reconstruction of OHCA from 1875-2005 (Fig. 2), but these correction periods are not evident as persistent biases in the EBM-KF (Fig. 4). Forward model biases may be ameliorated by adjusting various parameters away from literature values. Automated, optimized tuning of parameters is addressed in Section 5c and is well-studied in Kalman filter applications (Zhang and Atia 2020); the potential adoption of these tools to climate science is a key advantage of the EBM-KF hybrid.

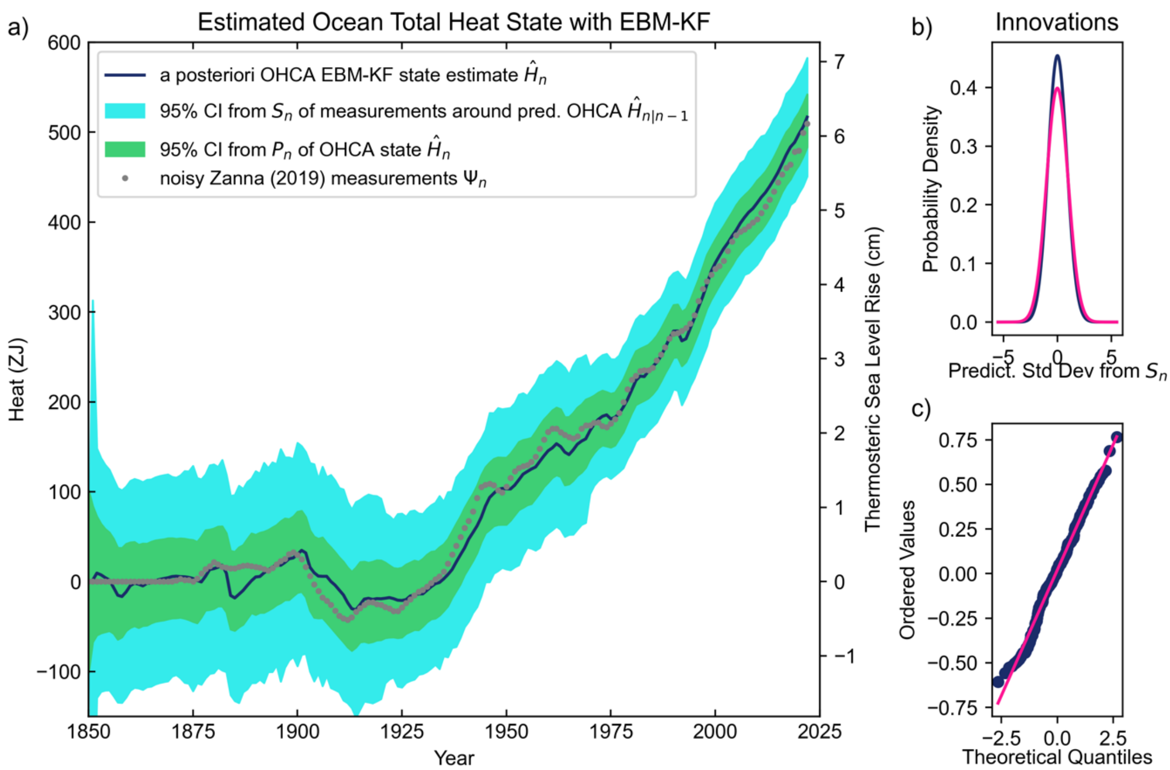


Fig. 4: EBM-KF state estimate for deep ocean OHCA in units of mean potential temperature from the same EBM-KF run as in Fig. 3. Annual-mean Zanna et al. (2019) reconstructions are assimilated (grey dots). Panels and colors as in Fig. 3.

Fig. 4 shows the deep OHCA component of the EBM-KF and its associated uncertainties. While the OCHA measurements from the Zanna et al. (2019) hybrid product are more autocorrelated than the HadCRUT5 GMST, the innovations for OHCA are again approximately Gaussian (panels 4b, 4c). In the context of this empirical probability distribution, each member of the Gaussian mixture has a larger σ given by the measurement uncertainties in the OHCA dataset relative to the predictive distribution. To average out to the nearly-Gaussian empirical probability distribution, it is unsurprising that nearly all autocorrelated OHCA measurements are also very close to the EBM-KF estimated state, rather than filling the full (light blue) predictive distribution as in Fig. 3. Rather than relying mostly on the blind EBM (see Fig. 2), the OHCA component of the EBM-KF pays much more attention to these measurements: shifting the OHCA state projection $\widehat{\mathrm{H}}_{n|n-1}$ by ±3.04 ZJ on average, range (-8.11 – 9.78ZJ); comparable with the OHCA adjustment in $\widetilde{\mathrm{H}}_{n}$ from the blind, forward EBM contribution ±4.46ZJ, up to (-25.31 – 14.40ZJ). Unsurprisingly, the blind EBM takes a substantially different track, lagging up to 91.4ZJ colder than the EMB-KF in 1998. Reflecting this improvement in measurement accuracy (as incorporated via $\mathrm{R}_{n}^{var}$), the OHCA-OHCA components of both state uncertainty $2\sqrt{P_n}$ and forecast uncertainty $2\sqrt{S_n}$ shrinks dramatically over the 173 year run. $2\sqrt{P_n}$, the envelope for the OHCA climate state estimate, has a very slow initial convergence that reaches 45.2ZJ by 1865 and then gradually falls to 29.5ZJ by 2000. $2\sqrt{S_n}$, the 95% predictive envelope for OHCA, drops from ~115.1ZJ by 1865 to 66.9ZJ by 1985 and then remains near this value through the present.

*b. Using the EBM-KF to determine Policy Threshold Crossing*

A single GMST measurement is not an accurate measurement of anthropogenic climate change due to the large internal variability of the system, and so a single annual temperature above a particular policy threshold is not a guarantee of the climate state crossing that threshold. One interpretation of "crossing" is when the uncertain climate state of GMST (here estimated to match the "standard climate normal", or 30-year mean GMST) is determined with a given probability to have passed a policy threshold. This "climate state above" the threshold definition was used by Tebaldi and Knutti (2018) for regional thresholds and the IPCC AR6 (Lee, Marotzke et al.) who state "the time of GSAT exceedance is determined as the first year at which 21-year running averages of GSAT exceed the given policy threshold." We use a 30-year averaging window nearly everywhere, but for consistency with these practices we use a 21-year averaging window for raw ESM simulations (only in Fig. 11 and Supp. Fig. 9). A second interpretation would be the chance that next year's annual-mean GMST will exceed the policy threshold, or "annual temperature forecast above" the threshold. The EBM-KF generates probability distributions for both the "climate state above" and the "annual temperature forecast above" interpretations of whether a policy threshold has been crossed.

This climate state threshold, as in the IPCC definition, is given in the EBM-KF by a Gaussian distribution (green in Fig. 5a) about the state $\hat{T}_n$ with a variance given by the GMST-GMST component of $P_n$. The IPCC has an ensemble of models to draw upon over both the historical period and future projections, so the fraction of the climate states (21-year means) of each of the ensemble members found above a given policy threshold determines the overall probability that the climate policy threshold was crossed. This ensemble interpretation assumes the ensemble spread is a good representation of GMST uncertainty – recent IPCC reports discount the 90% ensemble spread to a 66% confidence range because coarse climate models under-represent internal variability and model uncertainty as described in Box 4.1 (Collins, Knutti et al. 2013; Lee, Marotzke et al.). The EBM-KF does not require a future projection to arrive at a present-day climate state, because it already provides an instantaneous and continual estimate of $\hat{T}_n$. The uncertainty $2\sqrt{P_n}$ around *a posteriori* climate state $\hat{T}_n$ builds the probability of threshold crossing (see Fig. 5). So, the probability of the climate state exceeding the policy threshold is the integral of all probability density of the GMST climate state below that policy threshold. This is simply a Gaussian cumulative distribution function centered at $\hat{T}_n$ with variance set to the GMST-GMST component of $P_n$. The EBM-KF climate state covariance is chosen to reflect the uncertainty in the 30-year average of real-world GMST (see Section 2c)—using $R^{const}$ and Q matrices reflecting the 21-year means to match the IPCC definition would be a trivial modification.

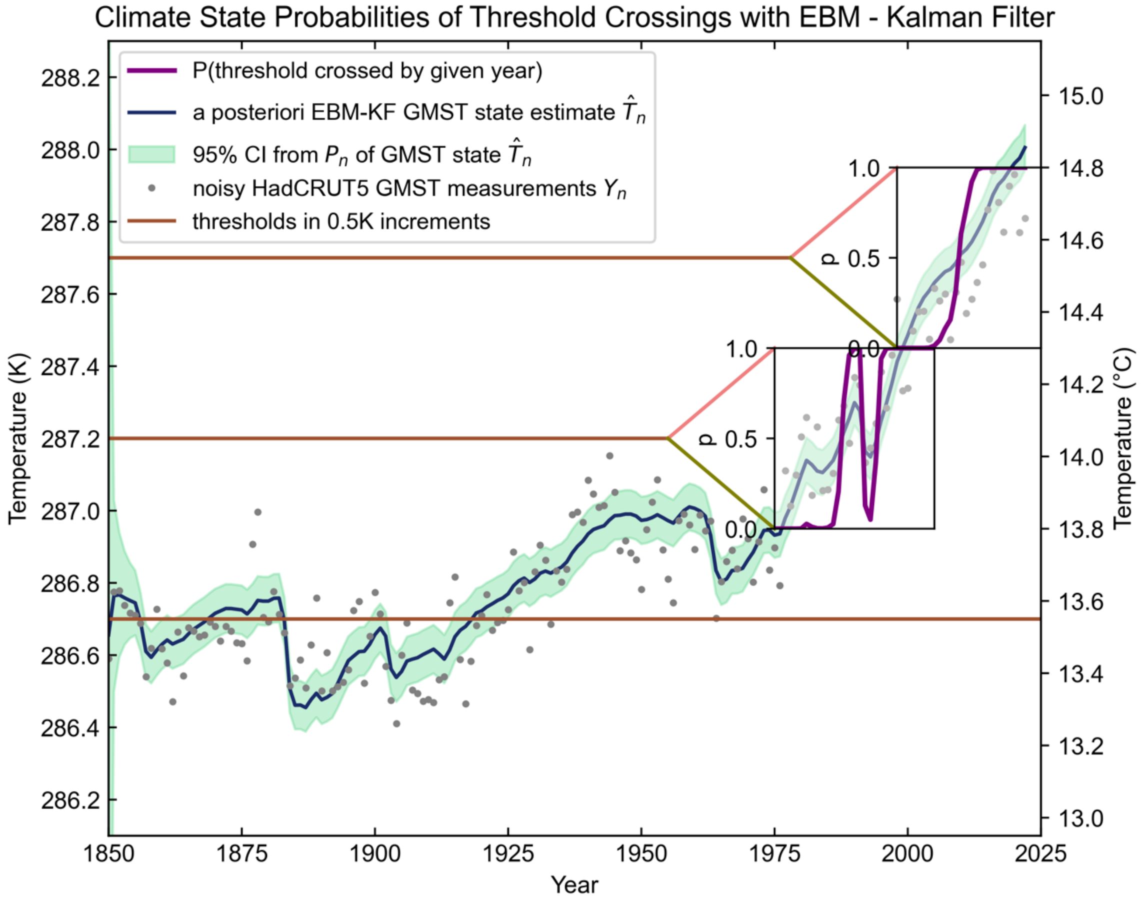


Fig. 5: EBM-KF and climate state crossing policy thresholds: As in Fig. 3, there are the EBM-KF GMST state estimate (navy blue line) $\hat{T}_n$, confidence interval of the climate state (light green) $2\sqrt{P_n}$, and GMST measurements (gray dots) $Y_n$. Additionally, policy thresholds (brown lines) are shown at 286.7K (+0K), 287.2K (+0.5K), and 287.7K (+1.0K) compared to the preindustrial baseline. Two inset boxes indicate threshold crossing probability, with a y-axis of cumulative probability (purple; from 0 to 1) and the x-axis in time (years).

For the second interpretation of temperature forecast above the policy threshold, the EBM-KF predicts a relevant window (blue in Fig. 6) of possible next-year GMST measurements. It is a Gaussian distribution centered at the projected state $\hat{T}_{n|n-1}$ with a variance given by the innovation covariance ($S_n$): in other words, a simulated draw from the *a priori* state. This uncertainty range reflects and encapsulates actual GMST measurements, not the uncertainty in the climate. For an ensemble of ESMs, the analogous temperature forecast probability is the fraction of ESMs at year $n$ that are warmer than the policy threshold (see Supp. Fig. 10).

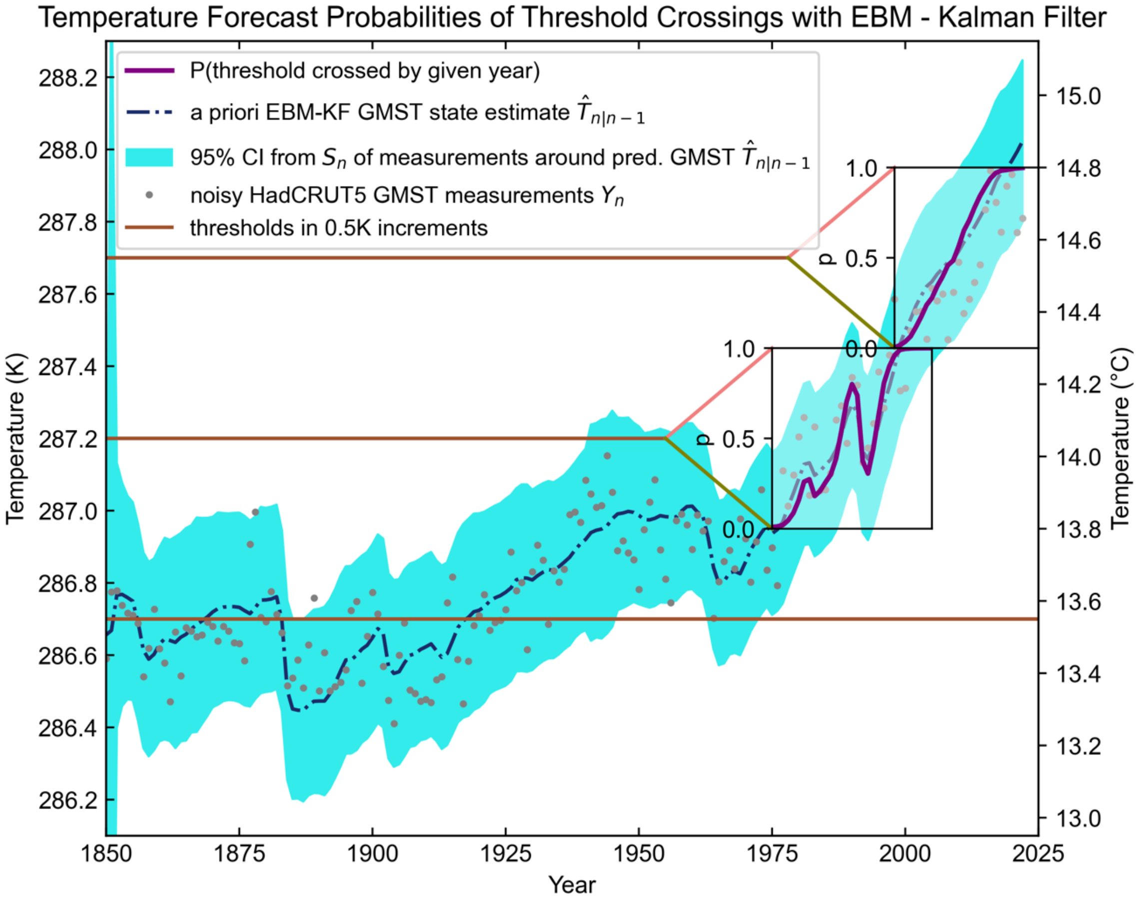


Fig. 6: The projected GMST "weather" 95% confidence window $2\sqrt{S_n}$ is shown in light blue around the a priori EBM-KF GMST state estimate (navy blue dashed-dotted line) $\hat{T}_{n|n-1}$ . Actual GMST measurements (gray dots) $Y_n$ are also shown. The two inset boxes indicate the likelihood that the actual GMST measurement will be above a particular policy threshold based on this projection, a y-axis of cumulative probability (purple; from 0 to 1) and the x-axis in time (years).

There is additional ambiguity regarding whether "crossing a policy threshold" should specify an instant or a brief period. Here we define (based on the 1σ confidence interval, or the *likely* range in IPCC terminology) the "policy threshold crossing period" to span from the earliest year when ≥15.9% of climate states or temperature forecasts exceed the policy threshold to the latest year when ≤84.1% of climate states or temperature forecasts exceed that policy threshold. A "policy threshold crossing instant" is the year when the probability of exceeding the policy threshold is nearest to 50% while continuing to increase (or *as likely as not* to have crossed the policy threshold in IPCC terminology). Regardless of whether an ESM ensemble (see Supp. Fig. 9) or EBM-KF (see Fig. 5) is used, the temperature forecast above threshold period has a longer duration than the climate state above period because the uncertainty/ensemble spread in the annual forecasts is wider than the uncertainty/ensemble spread of the time-averaged states. Both ESM ensemble and EBM-KF methods report similar policy threshold crossing instants (Fig. 11). The Mt. Pinatubo eruption in 1991 resets the +0.5K threshold crossing repeatedly in both the EBM-KF and ESM ensemble (Fig. 5 & 11d) by its perturbation of elevated aerosols.

Fig. 5 & 6 quantify the probability of crossing policy thresholds as a function of time (purple), inset on top of the relevant GMST timeseries and spread. The EBM-KF climate state estimate in Fig. 5 and annual temperature forecast in Fig. 6 are fairly aligned by year, although these two quantities are in entirely different probability domains. As the EBM-KF state estimate approaches any given policy threshold, the cumulative temperature policy threshold approaches 0.5, or 50% at a "policy threshold crossing instant". The +0.5K policy threshold had crossing instants in 1988, 1992, and 1994, while the +1.0K policy threshold's crossing instant was in 2010. For the annual temperature forecast in Fig. 6, the policy threshold crossing periods were 1980-1997 for +0.5K, and 2003-2015 for +1.0K. The policy threshold crossing periods for the climate state in Fig. 5 are briefer: 1986-1995 for +0.5K and 2008-2012 for +1.0K. For comparison using LENS2 the analogous climate state thresholds are plotted in Supp. Fig. 9 and temperature forecast thresholds are plotted in Supp. Fig. 10. All threshold crossing periods and instants including future projections under SSP3-7.0 are compared directly in Fig. 11.

*c. The spread from one member – using EBM-KF to generate an analog for an ESM large ensemble spread*

There are many more past and future climate scenarios that researchers wish to investigate than there are computational resources to run a full large ensemble for each scenario. Fortunately, the EBM-KF allows for one or a handful of ESM simulations to approximate the distribution of an entire ensemble spread (similar to an approach taken for ensembles of ice sheet models in (Edwards, Nowicki et al. 2021; van Katwyk, Fox-Kemper et al. 2023). Any GMST "LENS2 climate state uncertainty window" $(\hat{T}_n)_i \pm 2(\sqrt{P_n})_i$ assimilating one model ensemble member $i$ roughly covers the spread of "climate states" $(\hat{T}_n)_j$ within the entire hindcast LENS2 simulation ensemble (Fig 6a,e). In other words, considering any one ensemble member simulation (run $i$) within LENS2, if we run the EBM-KF treating the global average of simulated surface temperatures and deep ocean temperatures as measurements $(\boldsymbol{y}_n)_j$, the resulting estimated GMST state uncertainty timeseries $(\sqrt{P_n})_i$ has a specific meaning regarding all other EBM-KF states $(\hat{T}_n)_j$ if this procedure is repeated for every other run $j$. In particular, all simulated EBM-KF states $(\hat{T}_n)_j$ are distributed with a standard deviation that is only 1.22 times larger than the average estimated GMST state uncertainty $\overline{(\sqrt{P_n})_i}$ and at worst 1.54 times larger than any particular $(\sqrt{P_n})_i$ (see Fig. 7d). Although the expected difference across an entire simulation run between $(\hat{T}_n)_i$ and the ensemble mean state $\overline{(\hat{T}_n)_j}$ is ±0.227$(\sqrt{P_n})_i$ with range (-0.731 - 0.817), or ±0.007K with range (-0.0265 - 0.0268)K, taking the average of multiple simulations will quickly approach the ensemble mean because of the central limit theorem. So, the EBM-KF approximates what "state uncertainty" intuitively means within the context of a large ensemble, a result especially remarkable because the error terms ($R_n$ and Q) were based on the HadCRUT5 dataset alone, not LENS2. Indeed, the EBM-KF using the real HadCRUT5 measurements can also roughly approximate LENS2 (see Fig. 7a,b,c), although this necessitates doubling (or enlarging by 2.5) the GMST state uncertainty $\sqrt{P_n}$ to cover the whole ensemble (see Fig. 7b). This adjustment is primarily necessary because the LENS2 runs are more similar to each other than to the real Earth, especially regarding outputs such as OHCA (see Supp. Fig. 11) and Arctic or Antarctic sea ice extent (Rosenblum and Eisenman 2017; Roach, Dörr et al. 2020; Horvat 2021). Also, the current generation of ESMs tend to underestimate the appropriate full spread of climate variability. For instance, some weather models use stochastic noise to push their distribution wider than dynamic variation alone (Buizza, Milleer et al. 1999), and other numerical climate models perturb parameters to achieve the same distribution-widening effect (Keil, Schmidt et al. 2021; Duffy, Medeiros et al. 2023). There are inter-annual differences which persist between runs of the ensemble and skew some climate states $(\hat{T}_n)_j$ cooler and others warmer (Fig. 7d), an effect not captured by the Kalman Filter framework.

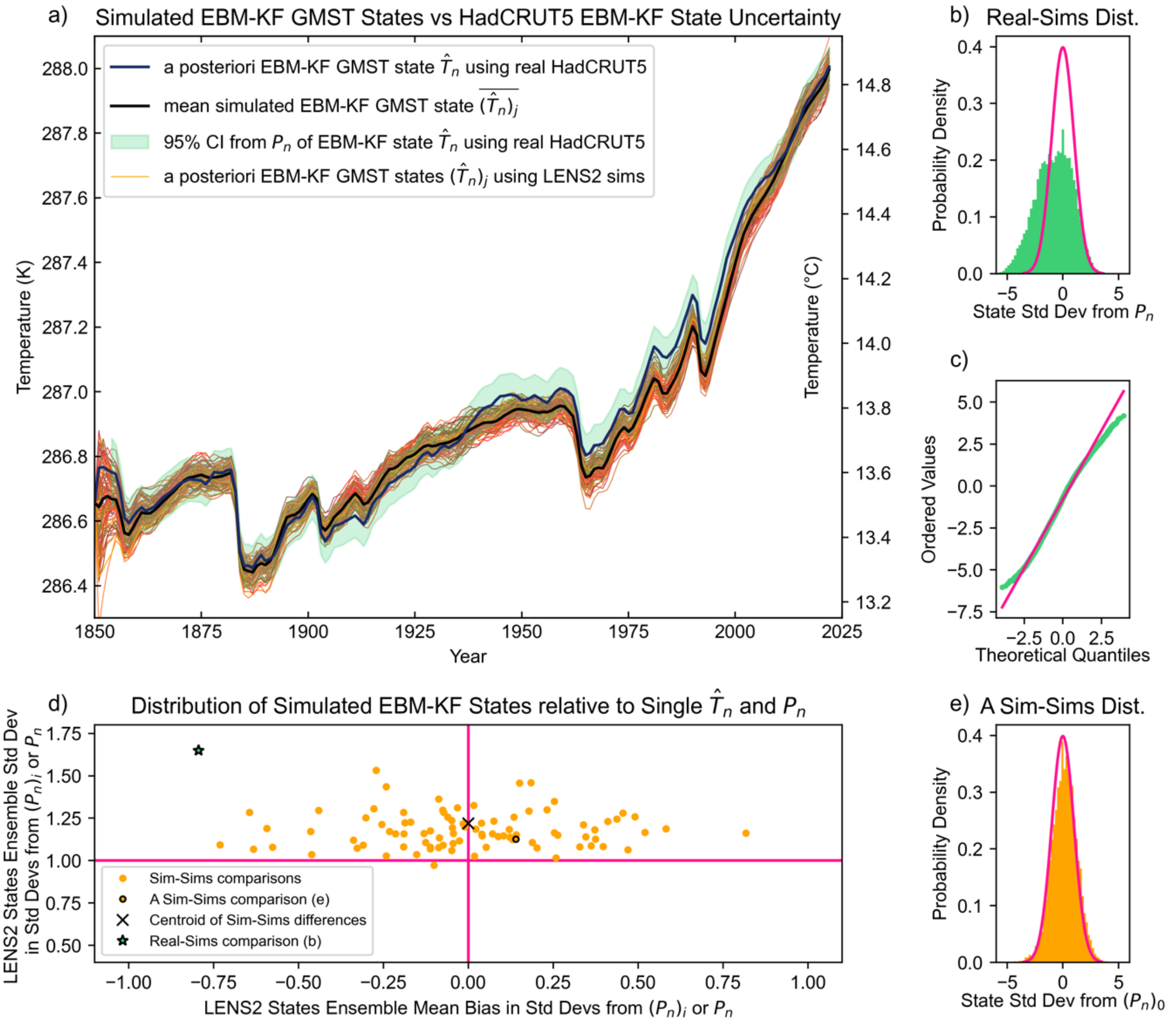


Fig. 7: Comparison of the GMST Kalman Filter states across the LENS2 ensemble. a) The EBM-KF *a posteriori* HadCRUT5 state estimate (thick blue) and its 95% confidence interval (light green), along with EBM-KF state estimates for each individual CESM2 ensemble member (orange lines) and their mean (thick black line). b) The differences between the "real" measurement based HadCRUT5 climate state and all LENS2 climate states, scaled by the state standard deviation and plotted against the ideal normal distribution. c) In the quantile-quantile plot, these differences between the "real" measurement based HadCRUT5 climate state and all LENS2 climate states distributions agree. d) Climate states and associated uncertainties arising from each of 90 LENS2 simulations and HadCRUT5 are compared to all other LENS2 climate states, and the relative bias and standard deviation of the resulting empirical distributions with respect to a particular $(\sqrt{P_n})_i$ are plotted. e) An example of these empirical distributions is graphed, indicated by the point circled in black within the scatterplot.

Fig. 7 shows that the EBM-KF climate state based on HadCRUT5 temperatures and EBM-KF climate states based any one of the LENS2 ensemble members show the expected level of consistency and Gaussian differences. The GMST was estimated from the GSAT of each LENS2 ensemble member. Thus, the EBM-KF on observations or on any one of the ensemble members does a good job of estimating the climate state (i.e., averaged over internal variability) and its uncertainty as simulated by the LENS2.

### *d. Sampling Future Projections from a Non-Gaussian Volcanic Distribution*

In standard climate assessments (e.g., IPCC 2021), future volcanism has long been singled out as an unknown aspect of projected climate change in any given future year, particularly regarding tropical eruptions' contribution to planetary albedo (Marshall et al. 2022). The forcing of historical-period climate models includes the effects of known past volcanoes, while the forcing of future climate models includes only "background forcing from volcanoes", i.e., an expected average forcing value in future years. Because of the nonlinearities and feedbacks in the climate system, applying an average forcing is not the same as averaging over individual events (compare blue line to black lines in Fig. 8). Individual volcanoes can also shift policy thresholds (as seen from Pinatubo in Fig. 5). However, running an ESM ensemble of sufficient size to explore the low probability of a large volcanic eruption in any potential year is not computationally feasible using traditional ESMs–it is easily accomplished with the EBM-KF. The added contribution of $CO_2$ and other greenhouse gases from volcanic eruptions is not included in this analysis, both because all volcanoes at all latitudes make this contribution (and so it is a different, less intermittent distribution), and because this annual contribution is miniscule compared to anthropogenic greenhouse gasses: 20x smaller in 1900, 130x smaller in 2010) (Gerlach 2011).

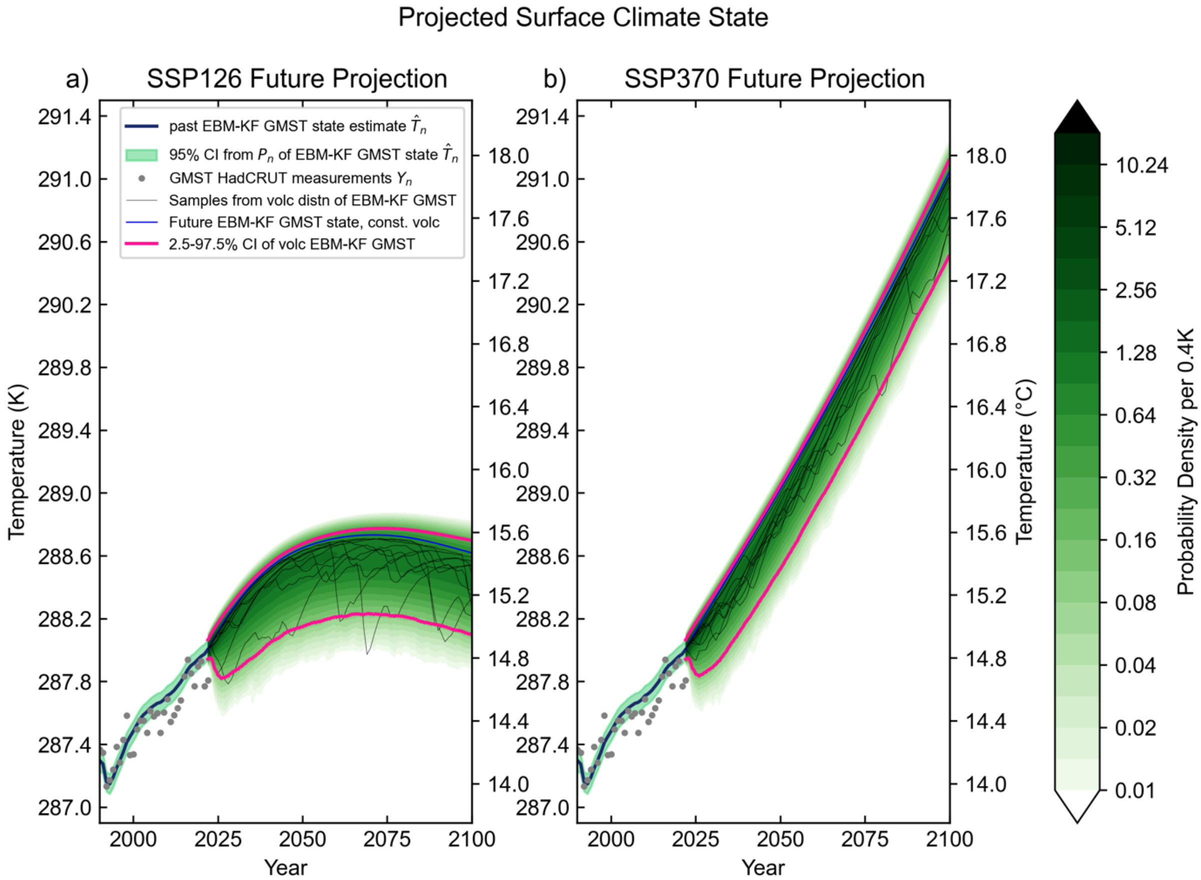


Fig. 8: Future GMST projections of SSP1-2.6 (a) and SSP3-7.0 (b) scenarios using sampled measures of volcanic activity and greenhouse gas concentrations calculated according to MAGICC7.0 (Meinshausen, Nicholls et al. 2020). The historical Mt. Pinatubo eruption in 1991 is shown in the lower left corner of both graphs for scale. 10 of the sampled 6000 potential future climate states from the volcanic probability distribution are graphed (thin black), along with a future climate state projection that uses constant volcanism with average AOD (blue). The probability density function formed by taking the summation of all sampled Gaussian kernels at each time point is shaded in green on a logarithmic scale (note these probability densities are not probabilities so they can exceed 1). Pink lines show the 2.5-97.5% confidence interval of these asymmetrical probability density functions.

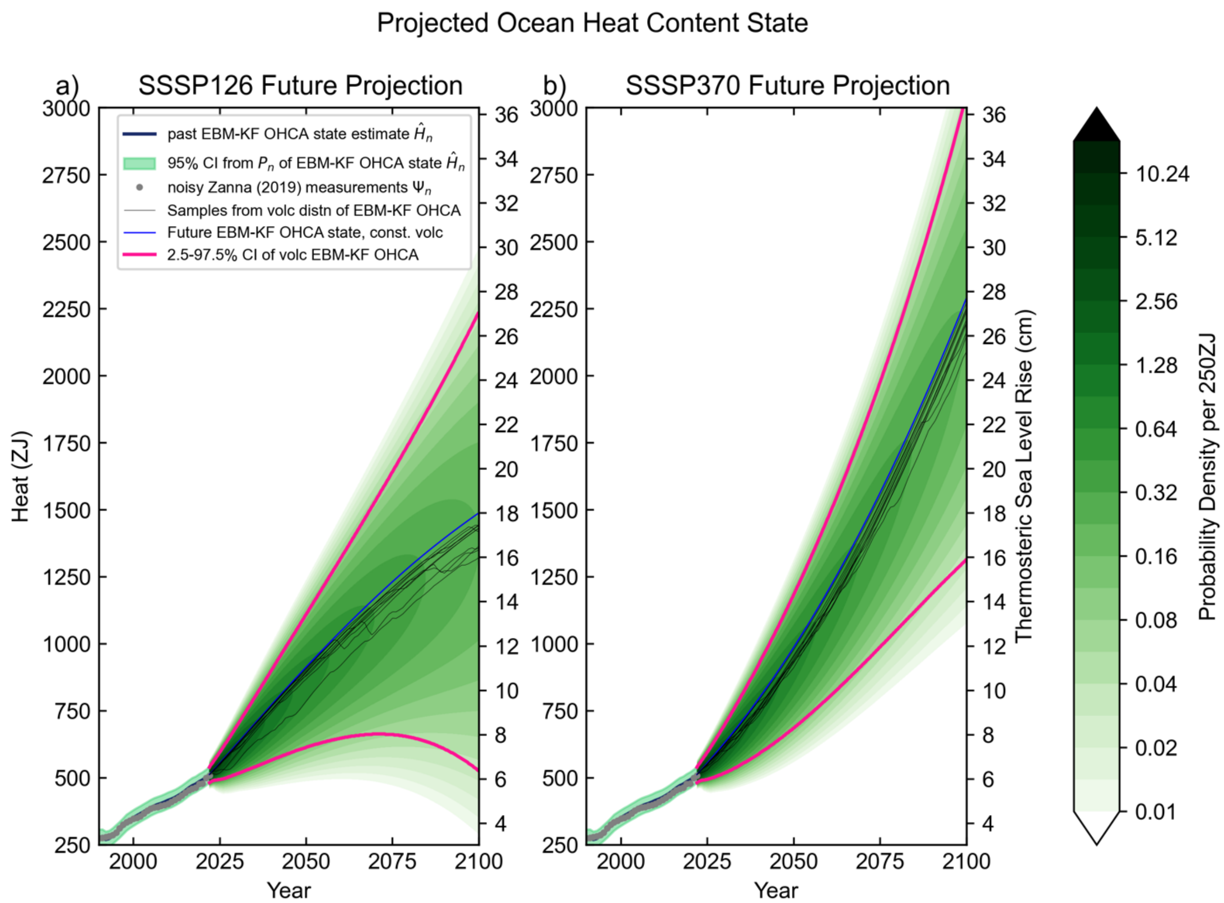


Fig. 9: Future OHCA projections of SSP1-2.6 (a) and SSP3-7.0 (b) scenarios using sampled measures of volcanic activity and greenhouse gas concentrations calculated according to MAGICC7.0 (Meinshausen, Nicholls et al. 2020). 10 of the sampled 6000 potential future climate states from the volcanic probability distribution are graphed (thin black), along with a future climate state projection that uses constant volcanism with average AOD (blue). The probability density function formed by taking the summation of all sampled Gaussian kernels at each time point is shaded in green on a logarithmic scale (note these probability densities are not probabilities so they can exceed 1). Pink lines show the 2.5-97.5% confidence interval of these asymmetrical probability density functions.

Fig. 8 shows the future projections of GMST using EBM-KF, including sampling from future volcanoes for two scenarios, and the corresponding projections of OHCA are in Fig. 9. SSP1-2.6 in Fig 7a is has $CO_2$ emissions that sharply decline after 2020 to keep GMST rise below 2K (van Vuuren, den Elzen et al. 2007; van Vuuren, Stehfest et al. 2017). SSP3-7.0 in Fig. 8b is a higher emission scenario in which $CO_2$ emissions double by 2100 (Fujimori, Hasegawa et al. 2017). Note that the volcanic ensemble probability density is not symmetrical for GMST - there is a much more gradual tapering off on the cooler side because of intermittent cooling by volcanic eruptions. In Fig. 8 the cooler side of the distribution takes a few years to fully expand out because large eruptions generally did not produce their maximal effect on AOD (and thus the GMST climate state) until 1-2 years after the eruption began, and there are no major eruptions ongoing at present. Indeed, the volcanic eruptions dominate the future uncertainty over the slowly growing state uncertainty and rival or exceed the scenario uncertainty up until about 2060. By contrast, the LENS2 using "constant background" future volcanism has a symmetrical distribution for future projections of the same SSPs (Supp Fig. 9).

Across many future simulations the dynamic model Jacobian matrix $\Phi_n$ happens to remain nearly constant at values of: $\Phi_n \approx \begin{bmatrix} 0.893 & 0.000253\ K/\frac{W\,yr}{m^2} \\ 11.1\ \frac{W\,yr}{m^2}/K & 0.999 \end{bmatrix}$, nearly unit triangular. Due to this Jacobian matrix shape and the 0.893 factor, the GMST-GMST component of the state covariance $P_n$ grows sub-linearly, with yearly growth less than the GMST-GMST component of $Q = 0.00037\ K^2$. Over a 78-year future projection (2023-2100) the GMST state 95% confidence interval $2\sigma = 2\sqrt{P_n}$ only grows from 0.0625K to between 0.1757K and 0.1792K. This 2.8-fold increase is small over the 21st century compared to the GMST dips that occur under volcanic eruptions (see Fig. 8). The effect of volcanoes on historical state (Fig. 2) and future projections (Fig. 8) is therefore worthy of specialized treatment in addition to measurement uncertainty and internal chaotic variability (see Section 3d). In contrast, the OHCA component of the state uncertainty 95% confidence interval $2\sigma = 2\sqrt{P_n}$ grows exponentially due to the 11.1 value in $\Phi_n$, and volcanoes have a negligible effect on of projected OHCA trajectories (see Fig. 9). The ocean state uncertainty 95% CI $2\sqrt{P_n}$, initially at $2.57\frac{\mathrm{W\,yr}}{\mathrm{m}^2}$ (29.4 ZJ) in 2023, balloons to $76.1\text{-}77.1\frac{\mathrm{W\,yr}}{\mathrm{m}^2}$ (870-880 ZJ) by 2100.

Regarding future policy threshold crossings, the uncertainty regarding volcanic eruptions lessens the difference between the climate state threshold crossing interval and the temperature prediction threshold crossing interval.

## 4. Discussion

The EBM-KF climate state estimate resembles other standard estimates of climate state, but it has advantages they do not share. The EBM-KF algorithm, because of its relationship to a forward or "blind" EBM, can be projected forward in time without temperature observations and thus can be used in many situations. Unlike an ESM, the EBM-KF benefits from data assimilation due to its Kalman filter nature and thus remains close to observations or synthetic data (e.g., the ensemble of potential volcanic activity futures in Section 4d). This is especially true for the OHCA component (see Fig. 2), largely because of reduced understanding of the ocean dynamics that drive deep ocean heat uptake compared to atmospheric radiative feedbacks and our correspondingly simpler model of this process within the EBM. Unlike an Ensemble Kalman filter approach that can reweight a full-physics ESM ensemble toward observations, the EBM-KF has negligible computational cost and can thus examine rare, long-tailed events such as volcanoes with the necessary number of samples (Section 4d). Additionally, tuning of the EBM parameters and uncertainty quantification of these results can benefit from the literature and algorithms to optimize Kalman filter parameters.

*a. Comparison to Previous Estimation Methods of the Climate State*

In a direct comparison (Fig. 10) of the state estimated from the EBM-KF (Fig. 3) and that estimated by the 30-year running mean (Fig. 1) and the LENS2 ensemble (Supp. Fig. 4), the EBM-KF has slightly more year-to-year variation than the 30-year mean and less than LENS2. Departures from the main Gaussian cloud in all methods represent volcanoes. The 5 largest eruptions which caused the largest dip in EBM-KF state are labeled in Fig. 10, corresponding to the 5 peaks in AOD $\geq 0.06$ plotted in Fig. B1a in the appendix. The climate effects of these major tropical volcanic eruptions have been studied extensively (McCormick, Thomason et al. 1995; Jones and Kelly 1996 ). Note for the eruptions listed, plus many others, the dips in the EBM-KF mean state correspond with dips in the sample mean of the LENS2 simulations. However, the earliest AOD values provided by Sato (1993) also demonstrate a major spike at 1856, which is not reflected in the LENS2 simulations. This may correspond to either the 1956 eruptions of Komaga-take, Japan or Mt. Awu, Indonesia, and we labeled this with the latter eruption because tropical volcanic eruptions typically have a much larger climate impact (Marshall et al. 2022).

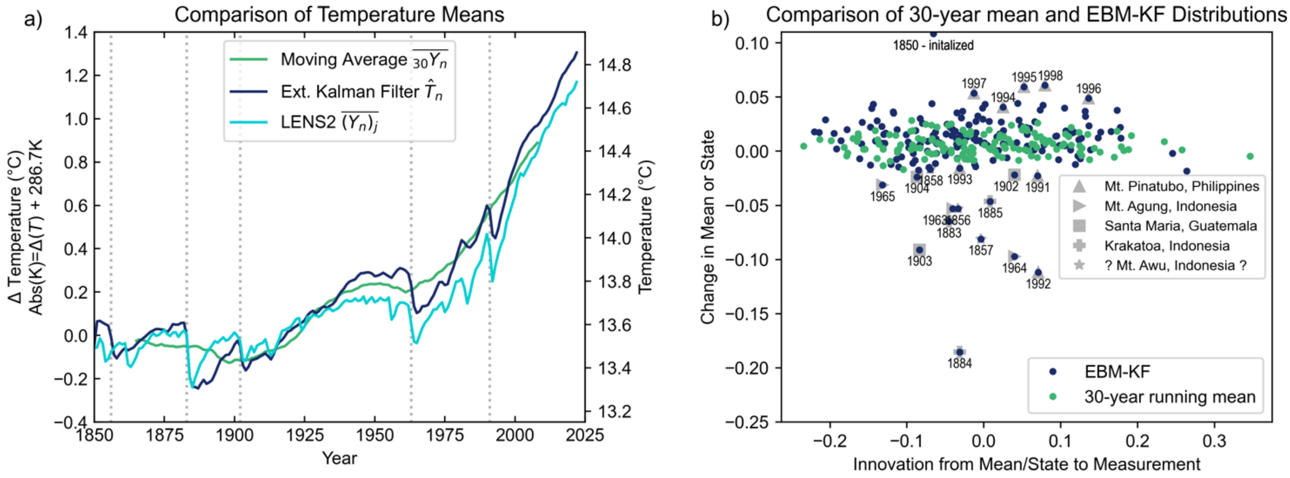


Fig. 10 a: Direct GMST "climate state" comparison of the 30-year averaged GMST (green), the EBM-KF state (navy blue), and the ensemble mean of GSAT in the LENS2 simulations (blue). b) For both the 30-year averaged GMST (green) and the EBM-KF state (blue), the distribution of innovations is plotted against the distribution of differences between the state estimate and instantaneous GMST measurements. Major volcanic eruptions are labeled with light grey symbols in b), and the corresponding eruption times are drawn in dotted vertical light grey lines in a). Change 3 years after all eruptions are marked in b), except Mt. Pinatubo which was marked for 8 years to demonstrate the rapid warming rebound in the EBM-KF state.

It is beyond the scope of this paper to detail the characteristics of the large and growing variety of "mean state" definitions, but a summary is useful. For all methods we have examined (30-year mean – Fig. 1, EBM-KF – Fig. 3, LENS2 model ensemble mean – Supp. Fig. 4, purely statistical methods – Supp. Fig. 2c, 2d, 3), the differences in the estimated climate state are relatively small in available years (on the order of 0.1K – see Supp. Fig. 12, column 1). The largest differences seen between these methods lie in the spread of the changes from year to year (see Supp. Fig. 12, column 2) and persistent mean anomalies relative to observations, particularly so in the forward, blind LENS2 ensemble (see Supp. Fig. 12, column 4).

The primary distinction of our EBM-KF method and all existing alternative definitions is the integrated quantification of uncertainty. While many methods exhibit a relationship between the "mean state" and "sample" that varies in time, the EBM-KF (and the related RTS) quickly converge to a stable state uncertainty of 0.034K (and 0.023K for the RTS, see Supp. Fig. 13). Our choice of method was motivated by the mathematical compatibility between the governing equation for a Kalman filter and that of an EBM, which is not true of many alternatives, e.g., a Butterworth filter or changepoint analysis and an EBM.

*b. Comparison to a Large Ensemble of an Earth System Model – CESM2*

The chief advantage of EBM-KF over an ensemble of ESMs is that it replicates most statistical features while being trivial to compute. Fig. 7 suggested that any of the ensemble members or the observed temperature record could be used together with EBM-KF to recreate the climate state, but now we examine if we can anticipate or improve on the ensemble statistics *without the ensemble*.

First, we examine the basic statistical character of LENS2. The distribution of annual differences of all ESM trajectories from the ensemble mean are remarkably close to Gaussian (see Supp. Fig. 6a). Therefore, again due to the central limit theorem, this fundamental assumption of the EBM-KF is also met by GSAT in the CESM2. The standard deviation does insignificantly rise with time in LENS2 over the entire simulation duration (p=0.168). Before 2065 this rise is significant ($p=1.2*10^{-6}$, see Supp. Fig. 6b) while relatively small (linear trend $r^2=0.105$ and only 8.9% rise in $\sigma$ from 1850-2065). The time-averaged standard deviation 0.127K was close to both the square root of the chosen total GMST-GMST measurement noise from $R_n$ (range 0.107 – 0.136K, see section 2c) and half the converged values in the EBM-KF of the GMST prediction standard deviation from $S_n$: 0.13K in 1865, later 0.112K in 2000. Examining skewness and kurtosis, the distribution of simulations about the LENS2 GSAT ensemble mean is not meaningfully altered as the climate warms (see Supp. Fig. 6c,d).

Next, we evaluated how well this LENS2 captures the overall shape of the observed HadCRUT5 temperatures, given that it is not constrained directly by these observations. The absolute temperature of the LENS2 runs had to be revised down by a full 1.75K to match its ensemble 1850-1950 100-year average GMST to HadCRUT5. Other authors have also noted this high absolute temperature as well as the high climate sensitivity of CESM2, the model used in LENS2 (Gettelman, Hannay et al. 2019; Feng, Otto-Bliesner et al. 2020; Zhu, Otto-Bliesner et al. 2022). Recall HadCRUT5 was recalibrated to a 1960-1990 30-year climate normal (Jones and Harpham 2013) of 13.85°C (287.00K), and the LENS2 average has a slightly lower temperature during this 30-year climate normal of 13.71°C (286.86K).

We also compared EBM-KF projections (Fig. 8) with LENS2 projections (Supp. Fig. 4). Both Fig 7b and the right side of Supp. Fig. 4 trace out roughly the same shapes, as both are forced by the SSP3-7.0 projections. The largely symmetric variation in the LENS2 is driven by dynamical instability. This is fundamentally different from the EBM-KF, which samples a noisy distribution of volcanic eruptions, yielding an asymmetrical distribution. LENS2 projections based on SSP3-7.0 achieve a slightly higher mean temperature in 2100

(291.3K, +4.6K warming) than the equivalent EBM-KF projection (290.9K, +4.2K warming, see Fig. 8b), despite the LENS2 simulations being cooler throughout most of the 20$^{th}$ century and early 21$^{st}$ century (see Fig. 10a). This reflects the high climate sensitivity of CESM2. Across all CMIP6 models (Lee, Marotzke et al. 2021; Tebaldi, Debeire et al. 2021) the projected warming is under this scenario is 3.9K with 5-95% range (+2.8K, +5.5K), closer to the EBM-KF projection.

Regarding the various types of climate policy thresholds, the LENS2 can be used to generate very similar results to the EBM-KF (Supp. Fig. 9, Fig. 11). Differences in absolute probability and policy threshold crossing instants reflect differences in the modeled climate states: particularly that the LENS2 ensemble was slightly cooler than the EBM-KF model after correcting to the same preindustrial temperature, so policy thresholds were crossed 3-5 years later (Fig. 11). The eruption of Mt. Pinatubo caused the policy threshold of +0.5K to be crossed in three instants within the EBM-KF model, because this eruption temporarily cooled the climate state back below the threshold temperature. The first of these EBM-KF crossings coincides very closely with the (single) policy threshold crossing instant of the 30-year running mean (indicated by orange asterisks). The 21-year running averages of the LENS2 simulations only crossed the 0.5K threshold once, illustrating how the EBM-KF state estimate fundamentally differs from a running mean. Future threshold crossings (1.5K, 2.0K, 2.5K) under the SSP3-7.0 projection scenario show close temporal alignment in the threshold instants between LENS2 and the EBM-KF estimates that sample for volcanic uncertainty. Although shifted, the overall shapes of these cumulative distribution functions and spans of the threshold crossing windows are more similar between LENS2 and a single EBM-KF future estimate that like LENS2 keeps AOD constant (see Fig. 11).

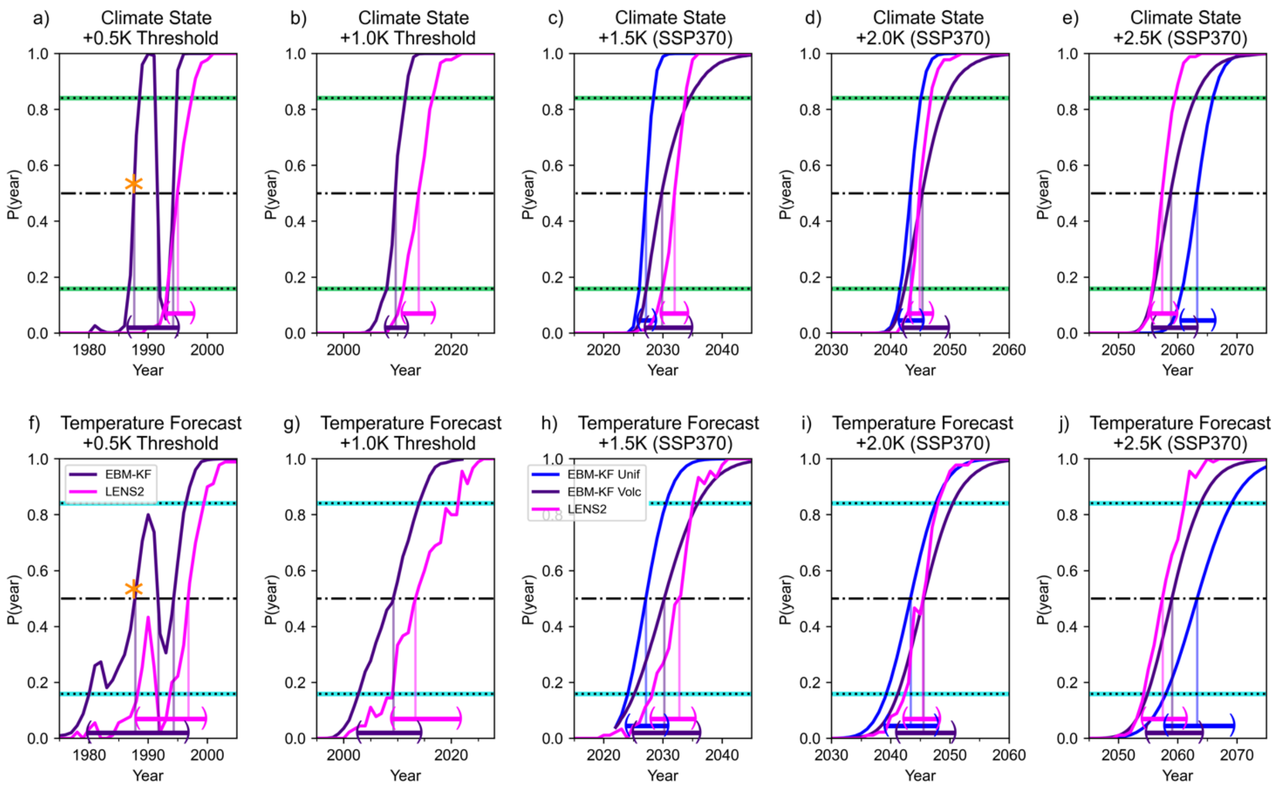


Fig. 11: Comparison of 0.5-2.5K GMST policy threshold crossing probabilities for the EBM-KF and CESM2 LENS simulations (pink). Recall from Section 3b that these are the integrals of all probability densities of the GMST climate states or temperature forecasts below that policy threshold. Historical EBM-KF estimates are in purple, reproduced from Fig. 4 & 5 insets in a,b,f,g. Two versions of future EBM-KF state estimates are shown in c,d,e,h,i,j: an amalgamation of samples in purple from the volcanic distribution shown in Fig. 8, and a single run in blue with uniform AOD mirroring how LENS2 treats volcanism. The top row a-e compares climate states in the EBM-KF with 21-year averages of the LENS2 simulations. The bottom row f-j compares next-year temperature forecasts from the EBM-KF directly with the LENS2 simulations. Policy threshold crossing instants (intersecting horizontal and vertical lines) and crossing windows (arrows at bottom) are also shown. An orange asterisk indicates 1987 in a) and f), the year that the true 30-year running mean of HadCRUT5 GMST crossed the +0.5K policy threshold, the +1.0K and later crossing instants of this 30-year running mean cannot be determined as it is within 15 years of the present.

### *c. Potential Issues with the EBM-KF and Future Extensions*

This first climate Kalman filter does not generate regional temperatures nor other essential climate variables, such as precipitation. These variables are often highly non-Gaussian and may require an understanding of regional “tipping points” or other important nonlinear process aspects of climate change. Therefore, this first EBM-KF is far from generating the information required to replace many aspects of large ensembles. An expanded global climate state vector, including precipitation, seasonal temperature, or eigenvalues of spatially decomposed principal components (e.g., El Nino / Southern Oscillation) might be appended into this statistical framework with appropriate physical forward modeling (Yang, Li et al. 2018).

Astute readers may note the estimated climate state and covariance within the EBM-KF is influenced by the choice of reconstructed HadCRUT 5 GMST and Zanna et al. (2019) OHCA. With only minor modifications, the EBM-KF method could be used with multiple annual reconstructions at the same time, e.g., GISTEMP GMST (Lenssen, Schmidt et al. 2019) or other OHCA reconstructions (Cheng, Trenberth et al. 2017; Ishii, Fukuda et al. 2017), considering each as only an estimate of the true GMST or OHCA (Willner, Chang et al. 1977). Reconstructions of sea level rise could be used from different sources as measurements of OHCA (Fox-Kemper, Hewitt et al. 2021).

Here we use pre-selected, constant parameters at their published values in the EBM-KF. However, methods for tuning parameters, including time-dependent parameters, within Kalman filters are much more extensively studied mathematically (Chen, Heckman et al. 2018 ; Zhang and Atia 2020 ; Chen, Heckman et al. 2021) than the methods thus far applied in climate sciences to diagnose parameter variations within energy balance models (e.g., the regional effects diagnosed from CCSM4 in (Armour, Bitz et al. 2013; Gregory and Andrews 2016)). Our EBM-KF hybrid presents an opportunity to adopt KF parameter optimization methods for the GMST, OHCA projection optimization problem. In a preliminary experiment with Bayesian parameter search to give better estimates of the coefficients in the blind EBM, the prior distributions of these coefficients (rather than point estimates) were extracted from climate science literature, followed by a Metropolis-Hastings search. Several parameters required further care or tuning to achieve desired constraints (e.g., balanced energy transfer in the preindustrial climate), such as the main longwave radiation coefficient and the temperature exponent. However, identifiability and overfitting are challenges of this approach and deserve more attention than the scope of this paper allows. In this first illustration of the system, opportune imperfections in the point estimates given by literature sources allow demonstration of the course-corrective properties of the EBM-KF (Fig. 4).

*d. Policy Utility*

Real-time, accurate knowledge of policy threshold crossing will allow for more prudent planning and more comprehensible communication of climate science to the public. For instance, while the "Climate Clock" (https://climateclock.world) intends to communicate the urgency of the climate crisis with a countdown to the estimated expenditure of our remaining carbon budget, only a static date informs it. In contrast, an EBM-KF threshold countdown would reflect the most recently measured state of the Earth system and up-to-date emissions and present limits on future emissions. Climate modeling with ESMs is slow, computationally expensive, and typically performed with blind models that do not respond to the latest observations. The relatively simple question, "How did the COVID-19 lockdowns and the 8% reduction in $CO_2$ emissions impact the near-term climate?" required hundreds of ESM simulations to yield a statistically insignificant answer (Jones, Hickman et al. 2021). That sort of modeling effort, arriving months or years after the question was posed, is an unsatisfactory prize for many aspects of communication and decision making for the annual profit or election term. The EBM-KF can produce the result that an 8% emissions reduction over 2 years cools the climate state by ~0.0017K and pushes back subsequent threshold crossing time by 1.2 months – an insufficient reduction in climate change, but at least precisely and rapidly quantified. The EBM-KF is sufficiently fast that, once fully calibrated, it could be easily embedded as an interactive web tool for such exploration.

Additionally, Kalman filters are often used for process control (Myers and Luecke 1991; Lee and Ricker 1994), and in this case an EBM-KF could be used to optimize climate change mitigation or intervention strategies (Filar, Gaertner et al. 1996; MacMartin, Kravitz et al. 2014; Kravitz, MacMartin et al. 2016). Once a space of potential climate solutions has been defined, the EBM-KF can work seamlessly with a variety of optimizers to find the maximum climate benefit at the lowest societal cost.

## 5. Conclusion

The EBM-KF presented in this paper takes the best features from a 30-year running average of GMST (the historical definition of climate) and state-of-the-art ESM large ensembles such as CESM2 LENS. The EBM-KF GMST climate state, which also tracks the ocean heat content anomaly (OHCA), is constructed to be very close to that of a running 30-year mean but generates this climate state 15 years sooner: it has no lag in reporting after annual observations are collected.. This filtered climate state does an excellent job in describing the overall shape of the 30-year means of measured GMST ($r^2 = 0.922$) and OHCA ($r^2 = 0.989$). In comparison to the ensemble spread of a hindcast ensemble of an ESM (LENS2), which is the state-of-the-art method for quantifying internal variability and probabilistic futures, the EBM-KF provides a similar Gaussian distribution. Using this distribution, EBM-KF can annually assess the likelihood of if a policy threshold, e.g., 2°C over preindustrial, has been crossed. The EBM-KF is also accurate at inferring the behavior of an entire climate model large ensemble using only one or a few ensemble members. In future projections of climate under SSP trajectories, the efficiency of the EBM-KF allows for sampling non-Gaussian probabilistic futures, e.g., the impact of rare but significant events such as future volcanic eruptions. An exponential mixture model of future volcanic eruptions causes the EBM-KF GMST climate states to be negatively skewed, unlike LENS2 which remains Gaussian.

The EBM-KF approach has transparent, clean physical parameters of the EBM that can be directly measured or taken from estimates in modeling literature, leading to trivial uncertainty quantification by the Kalman filter machinery under fixed parameters. This uncertainty quantification revealed important aspects of GMST and OHCA uncertainty, both in hindcast and future projections contexts, with and without volcanoes. We discussed if the EBM-KF needs time-varying EBM parameters or other extensions, although a thorough treatment is left for future work. While the EBM-KF does not predict all climate variables of interest, it is a powerful, transparent, and inexpensive tool that may be readily combined with other approaches.

*Acknowledgments.*

BFK was funded by ONR N00014-17-1-2393 and NOAA NA19OAR4310366. JMN was funded by a Brown University Fellowship and Brown OVPR Seed Award. Conversations with Jochem Marotzke, Piers Forster, Lorraine E. Lisiecki, Zebedee Nicholls, Larissa Nazarenko, and Jung-Eun Lee helped to focus this work.

*Data Availability Statement.*

This study performed re-analysis of existing datasets openly available at locations provided in Appendix A regarding historical $CO_2$ and AOD, for SSP projections at https://greenhousegases.science.unimelb.edu.au/, and for LENS2 at https://www.earthsystemgrid.org/dataset/ucar.cgd.cesm2le.atm.proc.monthly_ave.TS.html. For critical measurements of the climate state, GMST via HadCRUT5 is at https://www.metoffice.gov.uk/hadobs/HadCRUT5/data/current/download.html and OHCA from Zanna et. al. (2019) is at https://zenodo.org/record/4603700#.ZDuFNxXMI88. Further documentation about data processing, copies of the utilized datasets, and EBM-KF Python code is available through Harvard Dataverse at http://doi.org/10.7910/DVN/XLY8C2.

# APPENDICES

## Appendix A: *Derivation of the Blind Energy-Balance Model*

### *A1: Overall Structure of the Model*

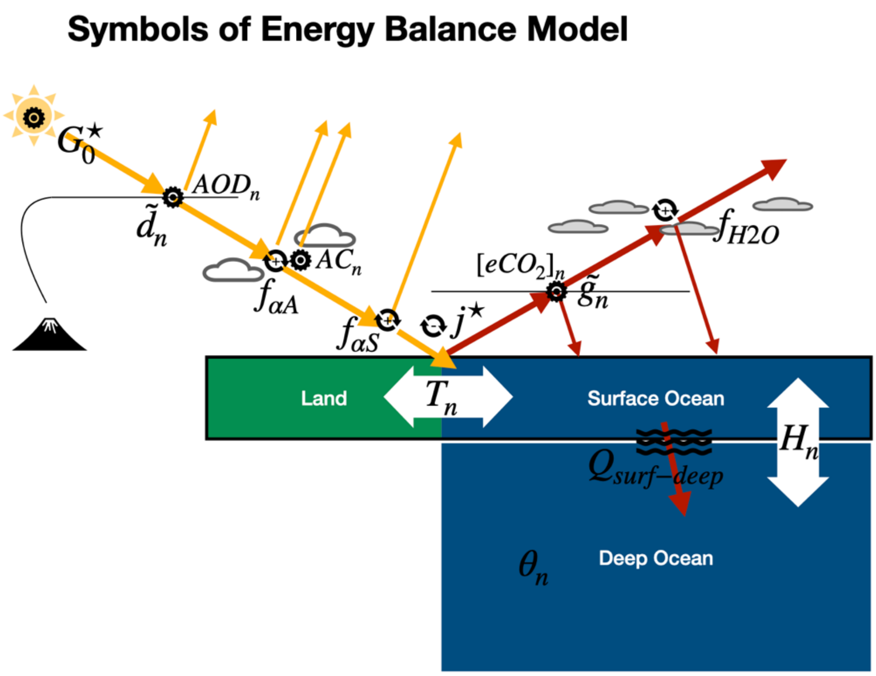


Fig. A1: Diagram listing the symbols in the energy balance model and its basic structure.

In the schematic diagram above, one stream of incoming solar shortwave energy $G_0^\star$ is successively fractionated by three reflective layers until a portion warms the ground and surface ocean. Then this surface layer radiates longwave infrared energy back to space $j^\star$, again with greenhouse "reflection" in two layers. The surface ocean warms the deep ocean with set thermal insulation between them.

Temperature-dependent feedbacks are shown as cyclical arrows, with positive and negative feedback indicated relative to the overall energy balance. Positive feedbacks increase the energy flowing to the surface at higher surface temperatures $T_n$ either by decreasing the fraction of shortwave reflection or increasing the greenhouse "reflection". Prescribed forcings are indicated by gear symbols. Unknown coefficients $\beta_0\,\beta_1\,\beta_2\,\beta_3$ exist respectively within the terms: $\tilde{g}_n$, $f_{H20}$ , $f_{\alpha A}$ , $f_{\alpha S}$. All these symbols are defined below.

Reiterating the overall structure in the model with equations, $T_n$ is the temperature of the surface in calendar year n (e.g. 2000), $\theta_n$ is the potential (or conservative) temperature of the deep ocean in that same year, and $H_n$ is the total ocean heat content combining the heat in the surface ocean and deep ocean. The calendar year (or index since 1850) is represented by n, and k is 1 year, the time step of this iterative model. Units are omitted in this section for brevity.

$$\Delta\text{Energy\_total} = \phi_{SW}(\text{in}) - \phi_{LW}(\text{out}) \tag{A1}$$

$$\Delta\text{Energy\_surf} = \phi_{SW}(\text{in}) - \phi_{LW}(\text{out}) - Q_{\text{surf}_\text{d}\text{eep}} \tag{A2}$$

$$\frac{T_{n+1}-T_n}{k} C_{surf} = G_0^\star * \widetilde{d_n} * f_{\alpha A}(T_n) * f_{\alpha S}(T_n) - j^\star(T_n) * \widetilde{g_n} * f_{H2O}(T_n) - \gamma * (T_n - \theta_n - \zeta) \tag{A3}$$

$$\frac{\theta_{n+1}-\theta_n}{k} C_{deep} = \gamma * (T_n - \theta_n - \zeta) \tag{A4}$$

$$H_n = (T_n - T_{1850}) * C_{surf0} + (\theta_n - \theta_{1850}) * C_{deep} \tag{A5}$$

$$\theta_n = (H_n - (T_n - T_{1850}) * C_{surf0})/C_{deep} + \theta_{1850} \tag{A6}$$

$$H_{n+1} = (T_{n+1} - T_{1850}) * C_{surf0} + \gamma * (T_n - \theta_n - \zeta) + (\theta_n - \theta_{1850}) * C_{deep} \tag{A7}$$

$$H_{n+1} - H_n = (T_{n+1} - T_n) * C_{surf0} + \gamma * (T_n - \theta_n - \zeta) \tag{A8}$$

Derivatives of $\theta_n$: $\frac{\partial \theta_n}{\partial H_n} = 1/C_{deep}$ (A9a) $\quad \frac{\boldsymbol{\partial \theta_n}}{\boldsymbol{\partial T_n}} = C_{surf0}/C_{deep}$ (A9b)

On the right side of equation A3, both the shortwave radiative flux $\phi_{SW}(\text{in})$ and longwave radiative flux $\phi_{LW}(\text{out})$ take the same form: (source $\{\mathbf{G_0^\star}, j^\star(T_n)\}$) * (prescribed attenuation $\{\widetilde{d_n}, \widetilde{g_n}\}$) * (attenuations with feedback $\{f_{\alpha A}(T_n) * f_{\alpha S}(T_n), f_{H2O}(T_n)\}$). $C_{surf}$, the heat capacity of the surface (including the atmosphere, thermally active soil, and an 86m upper layer of the ocean), was known least precisely of all coefficients: 17 ± 7 W (year) $m^{-2}$ $K^{-1}$, (Schwartz 2007). The deep ocean layer (technically the zone where most of the ocean warming occurs) was chosen for the purpose of heat capacity estimation to be an additional 1141m within the 71% of area covered by ocean based on previous work of this heat transfer process. (Geoffroy, Saint-Martin et al. 2013; Hall and Fox-Kemper 2023). This gives $C_{deep}$ = 1141m *0.71 * 1030kg/$m^3$ * 4180Ws/kg/K * 1 yr/ (3.154*$10^7$s) = 155.7 W (year) $m^{-2}$ $K^{-1}$. Constants $\boldsymbol{\gamma, \zeta}$ form a linear heat flux $Q_{\text{surf}_\text{d}\text{eep}}$ into the deep ocean, as discussed below. Radiative fluxes are signified in this text by the symbol $\phi$, followed by specific details of that flux.

***A2: Individual Functional Parts and Derivation***

$G_0^{\star}$ is the extraterrestrial radiance, taken for the purposes of this model derivation to be (solar radiance)/4 =1360 W/m$^2$ / 4 = 340 W/m$^2$. Estimates of actual annual extraterrestrial radiance (total solar irradiance) indicate that it has varied since 1850 between 340.06 W/m$^2$ and 340.49 W/m$^2$ according to the Naval Research Laboratory 2 solar irradiance model (NRLTSI2_v02r01 (Coddington, Lean et al. 2017)). Within the hindcast EBM-KF model these NRL2 estimates were used, but this had a negligible effect on the model results compared to a constant 340 W/m$^2$ value.

$\widetilde{d_n}$ is the prescribed shortwave radiation attenuation due to volcanic dust, the direct radiative effect of anthropogenic aerosols, and non-cloud atmospheric effects. This stochastically varying quantity can be calculated from the (unitless) stratospheric optical depth $AOD_n$ (Sato, Hansen et al. 1993; Vernier, Thomason et al. 2011), according to the formula given by Harshvardan and King (1993; Schwartz, Harshvardhan et al. 2002). (g=0.853 is the middle of the given range). The $AOD_n$ values used are forcings for the GISS climate model from 1850 – 1978 (https://data.giss.nasa.gov/modelforce/strataer/tau.line_2012.12.txt, $AOD_n$ at 550nm) and globally averaged measurements from the GloSSAC_V2 satellite measurement product (Nasa/Larc/Sd/Asdc 2018) from 1979 – 2021 (https://asdc.larc.nasa.gov/project/GloSSAC/GloSSAC_2.0, $AOD_n$ at 525nm). These wavelengths are at the shorter end of the 0.25-4 μm range of incoming solar shortwave energy $\phi_{SW}$, allowing satellites to detect dust reflectance.

$$\widetilde{d_n} = \frac{1.33}{AOD_n * (1\text{-}g) + 1.43}, \quad g \in [0.834, 0.872] \tag{A10}$$

$$\widetilde{d_n} \approx \frac{9.07}{AOD_n + 9.73} \tag{A11}$$

Utilizing the equation above to calculate the dry-atmosphere reflected energy during a relatively aerosol-free period (2000-2005), when the aerosol optical depth was about 0.002m:

$$\phi_{SW_{clearsky}}^{refl\ by\ dryatm} = G_0^{\star} * (1 - \widetilde{d_{2002}}) = 340\,\frac{W}{m^2}\,\left(1 - \frac{9.07}{0.002+9.73}\right) = 23.1\,\frac{W}{m^2} \tag{A12}$$

This value agrees with the clear-sky reflected energy (53 [52-55] W/m$^2$) minus reflected surface energy (33 [31-34] W/m$^2$), of 20 [18-24] W/m$^2$ reported by Wild, Hakuba et. al. (2019). Furthermore, the measured and inferred aerosol optical depth measurements already include those contributions from the anthropogenic sources.

$f_{\alpha A}(T_n)$ is the additional atmospheric shortwave attenuation due to cloud albedo, while $f_{\alpha S}(T_n)$ is the surface shortwave attenuation due to ground albedo. A portion of this varying cloud albedo is direct thermal feedback, whereas another portion is due to cloud seeding by anthropogenic aerosols. To contain the EBM model's complexity, the changing ground albedo is assumed to be only thermal feedback: the shortwave aspect of land use changes are neglected. Taken together, these two terms and $\widetilde{d_n}$ yield an overall absorption of 0.707 as measured from March 2000 to February 2005 by the CERES satellite (Wielicki, Barkstrom et al. 1996; Loeb, Wielicki et al. 2009), or equivalently a top-of-atmosphere, all-sky albedo of 0.293. Decomposition of this overall albedo into its clear-sky component (0.153) yields a ground * dry atmosphere absorption fraction of 0.847.

$$0.847 = \widetilde{d_{2002}} * f_{\alpha S}(T_{2002}) = 0.932 * f_{\alpha S}(T_{2002}), \quad \text{thus} \quad f_{\alpha S}(T_{2002}) = 0.909 \quad \text{(A13)}$$

$$0.707 = \widetilde{d_{2002}} * f_{\alpha A}(T_{2002}) * f_{\alpha S}(T_{2002}) = 0.847 * f_{\alpha A}(T_{2002}), \quad f_{\alpha A}(T_{2002}) = 0.834 \quad \text{(A14)}$$

Verifying the reflected energies:

$$\phi_{SW_{clearsky}}^{refl\ by\ gnd} = G_0^{\star} * \widetilde{d_{2002}} * \left(1 - f_{\alpha S}(T_{2002})\right) = 340 \frac{W}{m^2} * 0.932 * 0.091 = 28.8 \frac{W}{m^2} \quad \text{(A15)}$$

$$\phi_{SW_{allsky}}^{refl\ by\ gnd} = G_0^{\star} * \widetilde{d_{2002}} * f_{\alpha A}(T_{2002}) * \left(1 - f_{\alpha S}(T_{2002})\right) = 24.1 \frac{W}{m^2} \quad \text{(A16)}$$

$$\phi_{SW_{allsky}}^{refl\ by\ clouds} = G_0^{\star} * \widetilde{d_{2002}} * \left(1 - f_{\alpha A}(T_{2002})\right) = 52.6 \frac{W}{m^2} \quad \text{(A17)}$$

There is a slight discrepancy in the clear-sky ground-reflected energy relative to the literature value (33 [31-34] W/m$^2$), but the all-sky reflected energies are much more closely aligned: the ground reported value is 25 [23-26] W/m$^2$, and the dry atmosphere + cloud reported value is 75 [71-77] W/m$^2$, compared to this inferred value of 52.6 + 24.1 = 76.7 W/m$^2$. (Wild, Folini et al. 2015) Note that this shortwave flux equation does not consider shortwave energy absorbed into the atmosphere, a substantial simplification.

$j^{\star}(T_n) = \sigma_{sf} T_n^4$ is the ideal black body radiation or Planck feedback, which derives from quantum mechanics, particularly the Stefan-Boltzmann law (Boltzmann 1884), which gives the Stefan-Boltzman constant $\sigma_{sf}$ = 5.670 $10^{-8}$Wm$^2$K$^{-4}$ as a coefficient. For the Earth, because the temperature is in the neighborhood of 287K, this black body radiation is primarily in the infrared spectrum, between 200 and 1200 cm$^{-1}$ (Zhong and Haigh 2013).

$\tilde{g}_n$ is the prescribed longwave attenuation due to $CO_2$ and other anthropogenic greenhouse gases ($CH_4$, $NO_2$, $O_3$, halogens), which is half of the fraction of radiative energy absorbed by those gases (because half is re-emitted upwards and half downwards). This absorbed, downwards-emitted fraction increases linearly by a factor of $\beta_0$ with respect to the logarithm of the $CO_2$ concentration measured in ppm (see Figure 6b of (Zhong and Haigh 2013)). $CO_2$ concentrations were taken as the historical concentrations used in the NASA GISS climate model 1850-1979 (https://data.giss.nasa.gov/modelforce/ghgases/Fig1A.ext.txt) and the NOAA global averages from 1980-2021 (https://gml.noaa.gov/webdata/ccgg/trends/co2/co2_annmean_gl.txt).

$$\phi_{LW}(\text{out}) = j^{\star}(T_n) - \frac{\phi_{LW}(\text{absorbed})}{2} = j^{\star}(T_n) * \tilde{g}_n * f_{H2O}(T_n) \qquad (A18)$$

$$\tilde{g}_n * f_{H2O}(T_n) = \left(1 - \frac{\phi_{LW}(\text{CO2 absorb})}{2\, j^{\star}(T_n)}\right) * \left(1 - \frac{\phi_{LW}(\text{H2O absorb})}{2\, j^{\star}(T_n)}\right) \approx \left(1 - \frac{\phi_{LW}(\text{CO2 absorb}) + \phi_{LW}(\text{H2O absorb})}{2\, j^{\star}(T_n)}\right) \qquad (A19)$$

$$\tilde{g}_n = 1 - \beta_0 \log_{10}([CO_2]_n) < 1 \qquad (A20)$$

Equation A18 refers to a single-layer atmosphere assumed by prior researchers such as Kravitz, Rasch, et. al. (2018). While the technically correct separation of A18 is shown on the right hand side of A12, the form for the product of $\tilde{g}_n * f_{H2O}(T_n)$ was chosen specifically to resemble the previous shortwave energy expressions, essentially representing $CO_2$ in an atmospheric layer above $H_2O$ (sequential filtering). Relating these two representations demands the simplification that both the longwave radiative fluxes absorbed by $CO_2$ and $H_2O$ are each smaller than twice the total ground-emitted longwave radiative flux, so their product is yet smaller and can be neglected. Indeed, for $CO_2$ this ratio $\frac{\phi_{LW}(\text{CO2 absorb})}{2\, j^{\star}(T_n)} = \beta_0 \log_{10}([CO_2]_n)$ is in the range [0.165, 0.176] and for $H_2O$ the analogous ratio is in the range [0.250, 0.259] so their product (the difference between the RHS and LHS of A12) is at most 0.045. This difference in energy flux would be large enough to cause significant inaccuracies in the energy balance model (larger than the anthropogenic global warming signal), should parameters from a single-layer atmosphere be used in a sequential filter model. Thus, the critical parameters $\beta_0$ and $\beta_1$ must be calculated within the framework of the chosen model (here a sequential filter – see below), after which this distinction only matters to the higher-order terms of the deviations from the preindustrial energy flux (0.176-0.165) * (0.259-0.250) $\approx 0.0001$, a negligible fraction.

More complex functions for $\tilde{g}_n$ exist involving functions for each individual greenhouse gas (Meinshausen, Nicholls et al. 2020) but for the purposes of simplifying this energy balance model, only one "effective greenhouse" concentration is used. Our "effective greenhouse gas concentration" includes $CH_4$, $N_2O$, $O_3$, contrails, stratospheric water vapor, land use, and black carbon on snow but excluding anthropogenic atmospheric aerosols (Forster, Smith et al. 2023). Formally, land use and black carbon on snow should be included as a prescribed change to the $f_{\alpha S}$ function on the shortwave side but in combination these two amount to within -0.15 W/m$^2$, less in absolute value than all the other aforementioned "combined greenhouse forcing" components aside from contrails and stratospheric water vapor. Similarly, the prescribed contribution of stratospheric water vapor should formally be within the $f_{H2O}(\mathrm{T_n})$ function not lumped with the other greenhouse gases, but as this represents only 0.05 W/m$^2$ at most, this is inconsequential (variations in incoming solar insolation are of a similar magnitude). We determined the "effective CO2 concentration" by first fitting a function relating CO2 concentrations reported above to the CO2 forcings reported by Forster (2023).

$$\phi_{LW}^{CO2} = 12.74\ \log_{10}([\mathrm{eCO_2}]) - 31.55 \quad \text{(A21)}$$

Then by summing all "effective greenhouse gas" reported energy fluxes, the above function was inverted to determine the "effective CO2 concentration." These ranged from 278 ppm (or $\log_{10}([\mathrm{eCO_2}]) = 2.444$ when there was no "effective greenhouse gas" energy flux to 558.7ppm or $\log_{10}([\mathrm{eCO_2}]) = 2.747$ in 2022.

$f_{\mathrm{H2O}}(\mathrm{T_n})$ is the additional atmospheric longwave attenuation due to water vapor and other gasses, including both lapse rate and relative humidity. The precise functional form of this feedback function is unknown, as is the functional form of the two shortwave feedbacks, partially due to disagreements between paleoclimate inferences and ESMs. We thus introduced the following 3 functions, which incorporate an additional 3 positive $\beta$ coefficients and 1 exponent. (Note $f_{H2O}(\mathrm{T_n})$ can be either linearized into a form like these other feedbacks or rewritten in the $\left(1- \frac{\phi_{\mathrm{LW}}(\mathrm{H2O\ absorb})}{2\,\mathrm{j}^{*}(\mathrm{T_n})}\right)$ form.)

$$f_{H2O}(\mathrm{T_n}) \doteq \beta_1 (1/\mathrm{T_n})^{\mathrm{p_1}} \approx 1-\left(1+\beta_1 (\mathrm{T_{2002}})^{-\mathrm{p_1}} - \beta_1 \mathrm{p_1} (\mathrm{T_{2002}})^{-\mathrm{p_1}-1} * (\mathrm{T_n}-\mathrm{T_{2002}})\right) \quad \text{(A22)}$$

$$f_{\alpha A}(\mathrm{T_n}) \doteq 0.834\left(1+\beta_2(\mathrm{T_n}-\mathrm{T_{2002}})\right)+\frac{AC_n-AC_{2002}}{\mathrm{G}_0^{\star}\,\widetilde{\mathrm{d}_{2002}}} \qquad \text{(A23)}$$

$$f_{\alpha S}(\mathrm{T_n}) \doteq 0.909\left(1+\beta_3(\mathrm{T_n}-\mathrm{T_{2002}})\right) \qquad \text{(A24)}$$

Finally returning to the heat flux between the surface and the deeper layer of the ocean, other researchers have modeled this $Q_{\text{surf-deep}}$ as a simple thermal conductivity $\gamma$ multiplied by the difference in deviation temperatures between the surface ($\Delta\,\mathrm{T_n} - \Delta\,\theta_\mathrm{n}$), with these deviations measured relative to the pre-industrial equilibrium.

$$Q_{surf-deep} = \gamma(\Delta\,\mathrm{T_n} - \Delta\,\theta_\mathrm{n}) = \gamma * (\mathrm{T_n} - \theta_\mathrm{n} - \mathrm{T_{1850}} + \theta_{1850}) \qquad \text{(A25)}$$

If we take $\mathrm{T_{1850}}$ = 286.7K = 13.55°C and $\theta_{1850}$ = 276.7K = 3.55°C, then $\zeta = 10\mathrm{K}$. This consistent equilibrium temperature difference exists because the ocean is temperature stratified. We used $\gamma$ from the CMIP5 reported by Geoffroy (2013) to be 0.67±0.15 $\mathrm{W/m^2/K}$. Estimates of $\gamma$ from the CMIP6 coupled model comparison project were almost unchanged, 0.64±0.14 $\mathrm{W/m^2/K}$ (Hall and Fox-Kemper 2023). The deep ocean heat content record was extended back from 1850-1869 by prepending zero values. Since this is an equilibrium value, the deviation from the equilibrium deep ocean temperature $\theta_{1850}$ = 276.7K is given by the deviation from this baseline heat content.

### *A3: Solving for unknown β coefficients:*

Following the definition of climate feedback of w as $\partial N/\partial \mathrm{w}$ * dw/dT, where *N* is the TOA radiative flux (the entire EBM model), we equated the climate feedbacks of each of the three *f* feedback functions and the Planck response $\mathrm{j}^\star$, with the values (in $\mathrm{W/m^2/K}$) reported in Table 7.10 and Figure 7.10 of AR6 (Forster, Storelvmo et al. 2021).

$$\frac{\partial N}{\partial \mathrm{j}^\star} * \frac{\mathrm{d\,j}^\star}{\mathrm{dT_n}} = -\tilde{\mathrm{g}}_\mathrm{n} * \mathrm{f_{H2O}}(\mathrm{T_n}) * 4\sigma_\mathrm{sf}(\mathrm{T_n})^3 = -3.22 \qquad \text{(A26)}$$

$$\frac{\partial N}{\partial f_{H2O}(\mathrm{T_n})} * \frac{\mathrm{d}f_{H20}(\mathrm{T_n})}{\mathrm{dT_n}} = -\mathrm{j}^\star * \tilde{\mathrm{g}}_\mathrm{n} * -\beta_1 \mathrm{p_1}(\mathrm{T_n})^{-\mathrm{p_1}-1} = 1.30 \qquad \text{(A27)}$$

$$\frac{\partial N}{\partial f_{\alpha A}(\mathrm{T_n})} * \frac{\mathrm{d}f_{\alpha A}(\mathrm{T_n})}{\mathrm{dT_n}} = 340 * \tilde{\mathrm{d}}_\mathrm{n} * \mathrm{f_{\alpha S}}(\mathrm{T_n}) * 0.834\,\beta_2 = 0.35 \qquad \text{(A28)}$$

$$\frac{\partial N}{\partial f_{\alpha S}(\mathrm{T_n})} * \frac{\mathrm{d}f_{\alpha S}(\mathrm{T_n})}{\mathrm{dT_n}} = 340 * \tilde{\mathrm{d}}_\mathrm{n} * \mathrm{f_{\alpha A}}(\mathrm{T_n}) * 0.909\,\beta_3 = 0.42 \qquad \text{(A29)}$$

Solving for the exponent by taking the ratio of the first two equations yielded $\mathrm{p_1}$=1.615. Furthermore, based on the CERES measurements from 2000-2005, everything to the left of both $\beta_2$ (A13) and $\beta_3$ (A14) is the overall absorbed SW radiance of 340*0.707=240.5 W/m$^2$, so $\beta_2 = 0.00136$ K$^{-1}$ and $\beta_3 = 0.00163$ K$^{-1}$.

Figure 3.3 from Zhong and Haigh (2013) shows that per log10 order of magnitude of [CO2] increase, an additional 15.45 W/m$^2$ is absorbed. However, Forster (2023), the “greenhouse gas” absorption increases by 12.74 W/m$^2$ per log10 order of magnitude of effective [CO2] increase (eq. A21). This measurement approximating a partial derivative was presumably made recently, so we used the more recent 2002 temperature of ~287.5K (14.4°C), but this choice is relatively inconsequential: $\beta_0\beta_1$ would be only 0.66% larger if the pre-industrial temperature were used instead. In the pre-industrial climate, we assumed a steady-state equilibrium with a constant black body temperature of 286.66K (13.6°C) and a log10([effective CO2]) ≈ 2.444. This allows us to solve for $\beta_0$ and $\beta_1$ as follows:

$$12.74 = \frac{\partial N}{\partial \widetilde{g}_n} * \frac{\mathrm{d}\,\widetilde{g}_n}{\mathrm{d}\,\log_{10}([\mathrm{eCO_2}]_n)} = -\sigma_{sf}(T_n)^4 \beta_1 (T_n)^{-1.61}\left(-\beta_0\right) \quad \text{(A30)}$$

$$307.24 = \beta_1\beta_0 \quad \text{using} \quad T_{2002} = 287.5 \quad \text{(A31)}$$

$$0 = 340 * \widetilde{d}_n * f_{\alpha A}(T_{1850}) * f_{\alpha S}(T_{1850}) - \sigma_{sf}(T_{1850})^4 \beta_1 (T_{1850})^{-1.61}\left(1-\beta_0(2.444)\right) \quad \text{(A32)}$$

$$240.56 = \sigma_{sf}(286.7)^{2.39}\left(\beta_1\right)\left(1-\beta_0(2.444)\right) \quad \text{(A33)}$$

$$5842.68 = \left(\beta_1\right)\left(1-\beta_0(2.4)\right) \quad \text{(A34)}$$

$$6593.57 \approx \beta_1 \quad \text{and} \quad 0.04660 \approx \beta_0 \quad \text{(A35)}$$

Checking that Planck partial derivative is accurate, we obtained a value for climate sensitivity of j★ to be -3.34 W/m$^2$/K at current conditions and the sensitivity of $f_{H2O}$ to be 1.35 W/m$^2$/K, within the likely range of AR6. With an instantaneous doubling or quadrupling of $CO_2$ the sensitivity of j★ becomes -3.30 W/m$^2$/K or -3.22 W/m$^2$/K respectively, matching the reported value. Because they were defined to have proportional climate sensitivities, $f_{H2O}$ exactly matches AR6 in a 4x$CO_2$ scenario, with 1.30 W/m$^2$/K.

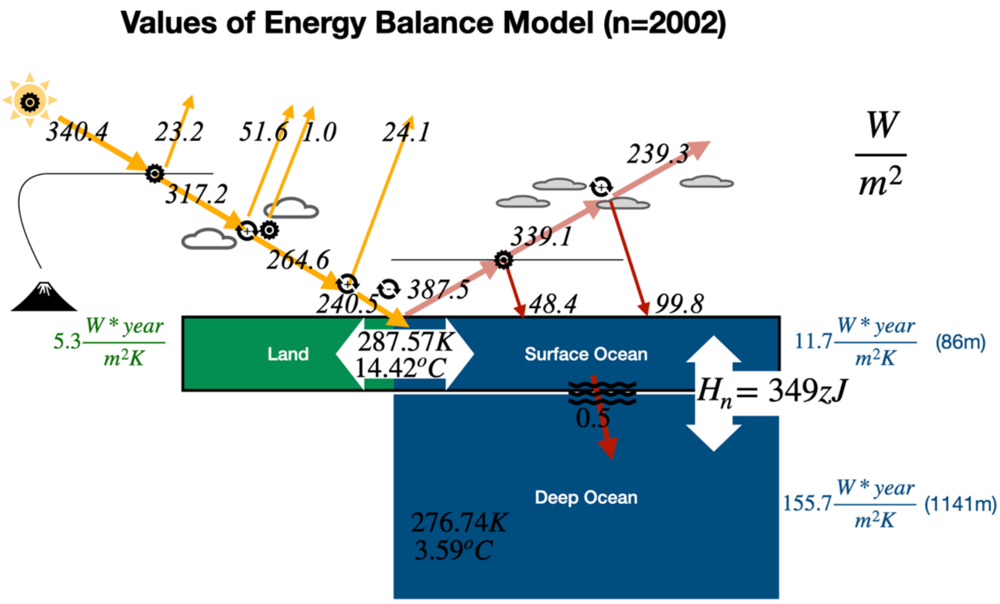


Fig. A2: Diagram with energy fluxes, temperatures, and total ocean heat content for the blind run of energy balance model in 2002 (when many of the reflectivity values were first measured by satellite).

### *A4: Differentiating to Find the Jacobian Matrix*

This yielded a blind energy-balance model with good skill at predicting the GMST (orange dashed line in Fig. 2), $r^2 = 0.902$. Rewriting the overall model with $\beta$ coefficients,

$$\mathrm{T_{n+1}}=\mathrm{T_n}+\frac{257.9 * 9.068}{17\,(AOD_n+9.73)}\left(1+\beta_2(\mathrm{T_n}\text{-}287.5)+\frac{AC_n-AC_{2002}}{\mathrm{G_0^\star}\ \widetilde{\mathrm{d}_{2002}}\ 0.834}\right)\left(1+\beta_3(\mathrm{T_n}\text{-}287.5)\right)$$
$$-\frac{\sigma_{sf}\beta_1}{\mathrm{C_{surf}}}(\mathrm{T_n})^{2.39}\left(1\text{-}\beta_0\log_{10}([\mathrm{eCO_2}]_\mathrm{n})\right)\quad-\frac{\gamma}{\mathrm{C_{surf}}}(\mathrm{T_n}-\theta_\mathrm{n}-10)\qquad \text{(A36)}$$

Derivatives of $\theta_\mathrm{n}$: $\frac{\partial\theta_\mathrm{n}}{\partial H_n}=1/\mathrm{C_{deep}}$ (A9a) $\qquad \frac{\partial\theta_\mathrm{n}}{\partial T_n}=\mathrm{C_{surf0}}/\mathrm{C_{deep}}$ (A9b)

$$\frac{\partial\mathrm{T_{n+1}}}{\partial\mathrm{T_n}}=1+\frac{137.6}{\mathrm{AOD_n}+9.73}\left(\beta_2+\beta_3+2\beta_2\beta_3(\mathrm{T_n}\text{-}287.5)+\beta_3\frac{\widetilde{\mathrm{q_n}}-\widetilde{\mathrm{q}_{2002}}}{\mathrm{G_0^\star}\ \widetilde{\mathrm{d}_{2002}}\ 0.834}\right)$$
$$-\frac{2.39\,\sigma_{sf}\beta_1}{\mathrm{C_{surf}}}(\mathrm{T_n})^{1.39}\left(1\text{-}\beta_0\log_{10}([\mathrm{eCO_2}]_\mathrm{n})\right)-\frac{\gamma}{\mathrm{C_{surf}}}\left(1\text{-}\mathrm{C_{surf0}}/\mathrm{C_{deep}}\right)\qquad \text{(A37)}$$

$$\frac{\partial\mathrm{T_{n+1}}}{\partial\mathrm{H_n}}=\frac{\gamma}{\mathrm{C_{surf}}}*\frac{\partial\theta_\mathrm{n}}{\partial H_n}=\frac{\gamma}{\mathrm{C_{surf}\,C_{deep}}}\qquad \text{(A38)}$$

The ocean heat content update equation ($r^2 = 0.907$ blind) and related partial derivates are:

$$H_{n+1}=(T_{n+1}-T_{1850})*\mathrm{C_{surf0}}+\gamma*(\mathrm{T_n}-\theta_\mathrm{n}-\zeta)+(\theta_\mathrm{n}-\theta_{1850})*\mathrm{C_{deep}}\qquad \text{(A39)}$$

$$\frac{\partial \mathrm{H_{n+1}}}{\partial \mathrm{H_n}} = \mathrm{C_{surf0}}\,\frac{\partial \mathrm{T_{n+1}}}{\partial \mathrm{H_n}} + \gamma * \left(0 - \frac{\partial \theta_\mathrm{n}}{\partial H_n}\right) + \mathrm{C_{deep}}\,\frac{\partial \theta_\mathrm{n}}{\partial H_n} = \frac{\gamma}{\mathrm{C_{deep}}} * \left(\frac{\mathrm{C_{surf0}}}{\mathrm{C_{surf}}} - 1\right)\left(\frac{\mathrm{C_{surf0}}}{\mathrm{C_{surf}}} - 1\right) + 1 \tag{A40}$$

$$\frac{\partial \mathrm{H_{n+1}}}{\partial \mathrm{T_n}} = \mathrm{C_{surf0}} * \frac{\partial \mathrm{T_{n+1}}}{\partial \mathrm{T_n}} + \gamma * \left(1 - \frac{\mathrm{C_{surf0}}}{\mathrm{C_{deep}}}\right) + \mathrm{C_{surf0}} \tag{A41}$$

## Appendix B: *Generation of Volcanic Eruption Samplings*

As can be appreciated in Fig. B1a, long periods of no major volcanic eruptions (for instance 1935-1960) alternated with periods of many eruptions occurring in rapid succession (1883-1914, 1960-1994). Perhaps this observed pattern has some relation to magma or tectonic dynamics, but it prevented one Poisson distribution from describing the data well.

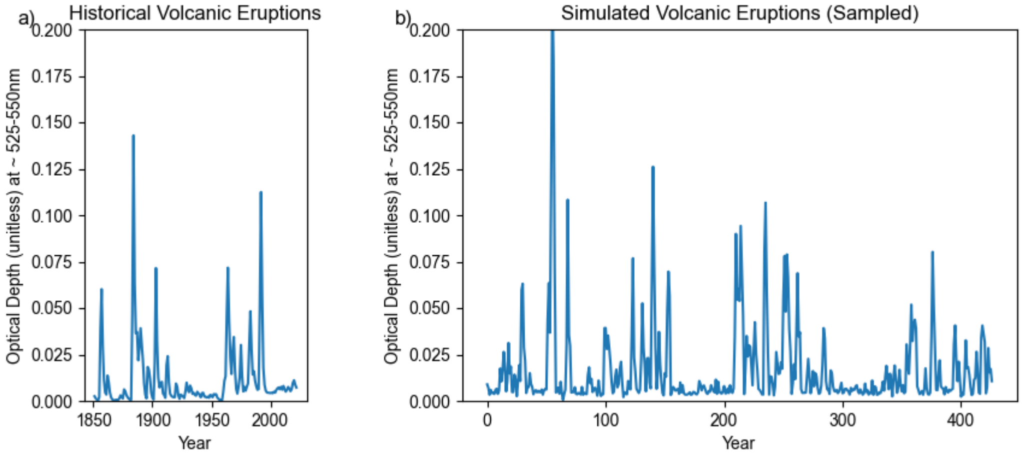


Fig. B1: Comparison of Historical Volcanic Eruptions (B1a) with Simulated Volcanic Eruptions (B1b), generated from a combination of several probability distributions.

Eruptions that occurred within 3 years were indistinguishable in the historical dataset, so the minimum time interval between simulated volcanic eruptions was 2.6 years plus a sample (Table B1) from the exponential mixture model $i_n$ (Okada, Yamanishi et al. 2020). These intervals were rounded to integers. Similarly, the size of each volcanic eruption $h_n$ was approximated using another shifted exponential distribution. The preceding year and two years following the eruption peak were positive fractions of the maximum aerosol optical depth, with gaussian blur. Similarly, non-volcanic years were positive gaussian noise (Table B2). Fig. B1b shows a sample from this combined generating function.

| **Exponential Distribution** | **Rand. Var.** | **Scale (units)** | **P(if mixture)** |
|---|---|---|---|
| Interval Between: round($i_{n,0} + 2.6$) | $i_{n,0} \sim$ Exp | 2.263 (years) | 88.9% |
| Interval Between: round($i_{n,1} + 2.6$) | $i_{n,1} \sim$ Exp | 24.2 (years) | 11.1% |
| Peak Size: $AOD_n = h_n + 0.0082$ | $h_n \sim$ Exp | 0.0339 (m) | |

Table B1. Exponential Parameters of Volcano Generating Function. This generating function starts with a list of zero values for all $AOD_n$, and first samples several of these n years to be major volcanic eruptions. "Interval Between" refers to the interval in years between two successive major volcanic eruptions.

| **Gaussian Distribution** | **Rand. Var.** | **Mean μ (units)** | **Std Dev σ** |
|---|---|---|---|
| Pre-Peak: $AOD_{n-1} = a_{-1} * E_n$ | $a_{-1}$ ~ Norm>0 | 0.51 | 0.25 |
| Post-Peak 1: $AOD_{n+1} = a_1 * E_n$ | $a_1$ ~ Norm >0 | 0.61 | 0.16 |
| Post-Peak 2: $AOD_{n+2} = a_2 * E_n$ | $a_2$ ~ Norm >0 | 0.32 | 0.16 |
| Other Years: $AOD_n = a_0$ | $a_0$ ~ Norm >0 | 0.00371 (m) | 0.00286 (m) |

Table B2. Gaussian Parameters of Volcano Generating Function. These distributions are sampled after the major eruptions have already been filled in by the exponential distributions in Table B1.

## Appendix C: *Glossary of Mathematical Symbols and Notation*

| **Symbol** | **Meaning** | **Context** | **Units** |
|---|---|---|---|
| p | Probability of the observed result for a particular hypothesis test (e.g. that the slope is positive) | Statistics | (0-1) |
| $r^2$ | Coefficient of determination: fraction of variance explained by a model | Statistics | (0-1) |
| σ<br>2σ = 95% CI | Standard deviation (√Variance)<br>95% confidence interval (extremely likely) under Gaussian distribution | Statistics | any |
| Cov() | Covariance of a random vector (here length 2) | Statistics | sq. matrix |
| n, k | Time index, time step | KF, EBM | year |
| $T_n$ | GMST surface temperature climate state, idealized | EBM-KF | K (°C) |
| $\theta_n$ | Deep ocean potential temperature state, idealized | EBM-KF | K |
| $H_n$ | Ocean heat content anomaly | EBM-KF | $\frac{W\ yr}{m^2}$ (ZJ) |
| $u_n=[CO_2]_n, AOD_n, AC_n$ | Time-varying concentrations in the atmosphere | EBM | ppm, ∅, W/m$^2$ |
| $[\tilde{T}_{n+1}, \tilde{H}_{n+1}] = \boldsymbol{F}(\tilde{T}_n, \tilde{H}_n, u_n)$ | Blind energy balance model, which is entirely deterministic based on prior climate state | EBM | $[\mathrm{K}, \frac{W\ yr}{m^2}]$ |
| $\Phi_n = \frac{\partial \mathbf{F}(\boldsymbol{x};u_n)}{\partial \boldsymbol{x}}\Big\vert_{x=\hat{x}_{n-1}}$ | Linearized tensor derivative of the (blind) EBM model | EBM-KF | $\begin{bmatrix} \varnothing & \mathrm{K} / \frac{W\ yr}{m^2} \\ \frac{W\ yr}{m^2}/K & \varnothing \end{bmatrix}$ |
| $\boldsymbol{x_n}=[T_n, H_n]$ | Idealized true climate state, with dynamic model noise | EBM -KF | $[\mathrm{K}, \frac{W\ yr}{m^2}]$ |
| $\hat{\boldsymbol{x}}_n = [\hat{T}_n, \hat{H}_n]$ | Estimate of the underlying climate state | EBM -KF | $[\mathrm{K}, \frac{W\ yr}{m^2}]$ |
| $\boldsymbol{y}_n = [Y_n, \psi_n]$ | Measurements with noise of the climate state, from HadCRUT5 and Zanna 2019. | EBM -KF | $[\mathrm{K}, \frac{W\ yr}{m^2}]$ |
| Q=COV$[w_n]$ | Assumed dynamic model error and model covariance matrix | KF | $\begin{bmatrix} K^2 & K\frac{W\ yr}{m^2} \\ K\frac{W\ yr}{m^2} & \left(\frac{W\ yr}{m^2}\right)^2 \end{bmatrix}$ |

| | | | |
|---|---|---|---|
| R=COV[$v_n$] | Assumed measurement error and measurement covariance matrix | KF | $\begin{bmatrix} K^2 & K\frac{W\,yr}{m^2} \\ K\frac{W\,yr}{m^2} & \left(\frac{W\,yr}{m^2}\right)^2 \end{bmatrix}$ |
| $\overline{_{30}\boldsymbol{y}_n}$<br>$\overline{_{30}Y_n}$ | 30-year running mean of measurements, undefined before 1865 or after 2008 | Prior climate methods | [K, $\frac{W\,yr}{m^2}$]<br>K |
| R$_n$= $R_n^{var} + R^{const}$<br>Q= $R^{const}/30$ | Actual covariance matrices used in the EBM-KF, defined to mimic the statistics of the 30-year running mean | EBM-KF | $\begin{bmatrix} K^2 & K\frac{W\,yr}{m^2} \\ K\frac{W\,yr}{m^2} & \left(\frac{W\,yr}{m^2}\right)^2 \end{bmatrix}$ |
| $\hat{\boldsymbol{x}}_{n\mid n-1}$<br>P$_{n\mid n-1}$ | KF a priori estimated state projection and state variance projection (before new measurement) | KF | [K, $\frac{W\,yr}{m^2}$]<br>$\begin{bmatrix} K^2 & K\frac{W\,yr}{m^2} \\ K\frac{W\,yr}{m^2} & \left(\frac{W\,yr}{m^2}\right)^2 \end{bmatrix}$ |
| $\boldsymbol{c}_n$<br>S$_n$ | Innovation residual,<br>Innovation covariance | KF | [K, $\frac{W\,yr}{m^2}$]<br>$\begin{bmatrix} K^2 & K\frac{W\,yr}{m^2} \\ K\frac{W\,yr}{m^2} & \left(\frac{W\,yr}{m^2}\right)^2 \end{bmatrix}$ |
| K$_n$ | Kalman gain: weight on innovation to correct state | KF | $\begin{bmatrix} \varnothing & \varnothing \\ \varnothing & \varnothing \end{bmatrix}$ |
| $\hat{\boldsymbol{x}}_n$<br>P$_n$ | KF a posteriori estimated state projection and state variance (after measurement) | KF | [K, $\frac{W\,yr}{m^2}$]<br>$\begin{bmatrix} K^2 & K\frac{W\,yr}{m^2} \\ K\frac{W\,yr}{m^2} & \left(\frac{W\,yr}{m^2}\right)^2 \end{bmatrix}$ |
| $\hat{\hat{K}}_n$ , $\hat{\hat{x}}_n$ , $\hat{\hat{P}}_n$ | RTS re-estimated Kalman gain, state estimate, and state covariance, following backward sweep | RTS | as above |

| | | | |
|---|---|---|---|
| $\gamma$ | Thermal conductivity between layers of the ocean | EBM | $\frac{W\ yr}{m^2\ K}$ |
| $\phi_{SW}$ , $\phi_{LW}$ | Net radiative fluxes (shortwave and longwave) at the top of the atmosphere | EBM | W |
| $\Delta$Energy_surf $Q_{\mathrm{surf_deep}}$ | Net heat flow into the surface and deep ocean layers respectively | EBM | W |
| $C_{surf}$ ; $C_{surf0}$ ; $C_{deep}$ | Heat capacities of the surface, surface ocean, and deep layers | EBM | $\frac{W\ yr}{m^2\ K}$ |
| $G_0^{\star}, j^{\star}(T_n)$ | Sources of shortwave (total solar radiance) and longwave (blackbody or Planck feedback) | EBM | $\frac{W}{m^2}$ |
| $\tilde{d}_n, \tilde{g}_n$ | Prescribed, time-varying attenuations from atmospheric dust and longwave radiation respectively | EBM | ∅ |
| $f_{\alpha A}(T_n) * f_{\alpha S}(T_n), f_{H2O}(T_n)$ | Attenuations due to albedo of the atmosphere, albedo of the surface, and longwave absorbing water vapor (all with feedback from $T_n$) | EBM | ∅ |
| $\zeta$ | Equilibrium temperature difference between the surface and deep ocean. | EBN | K |
| $\sigma_{sf}$ | Stefan-Boltzman constant = 5.670 $10^{-8}$ | EBM | $\frac{W\ m^2}{K^4}$ |
| $\beta_0$ | Solved coefficient on $\log_{10}([CO_2]_n)$ within a sequential filter atmosphere approximation | EBM | ∅ |

| | | | |
|---|---|---|---|
| $\beta_1$, $p_1$ | Solved coefficient and exponent for the $f_{H2O}(T_n)$ water vapor feedback on longwave | EBM | ∅ |
| $\beta_2$, $\beta_3$ | Solved coefficients for $f_{\alpha A}(T_n) * f_{\alpha S}(T_n)$, atmosphere and surface albedo feedbacks. | EBM | ∅ |
| $i_{n,0}$ $i_{n,1}$ | Exponential mixture random variables to determine the interval between major eruptions | Volcanoes | years |
| $h_n$ | Exponential random variable to determine size of a particular major eruption | Volcanoes | ∅ (AOD) |
| $a_{-1}$, $a_1$ , $a_2$, $a_0$ | Truncated gaussian distributions to determine the atmospheric optical depth in eruption-adjacent and non-eruption years. | Volcanoes | ∅ (AOD) |

Table C1: Glossary of Mathematical Symbols

# REFERENCES


Annan, J. D., J. C. Hargreaves, N. R. Edwards and R. Marsh (2005). "Parameter estimation in an intermediate complexity earth system model using an ensemble Kalman filter." Ocean Modelling **8**(1): 135-154 DOI: https://doi.org/10.1016/j.ocemod.2003.12.004.

Armour, K. C., C. M. Bitz and G. H. Roe (2013). "Time-Varying Climate Sensitivity from Regional Feedbacks." Journal of Climate **26**(13): 4518-4534 DOI: https://doi.org/10.1175/JCLI-D-12-00544.1.

Benhamou, E. (2018). "Kalman filter demystified: from intuition to probabilistic graphical model to real case in financial markets." arXiv e-prints **Statistical Finance (q-fin.ST)**(arXiv:1811.11618) DOI: https://doi.org/10.48550/arXiv.1811.11618.

Boltzmann, L. (1884). "Ableitung des Stefan'schen Gesetzes, betreffend die Abhängigkeit der Wärmestrahlung von der Temperatur aus der electromagnetischen Lichttheorie." Annalen der Physik **258**(6): 291-294 DOI: https://doi.org/10.1002/andp.18842580616.

Bouttier, F. (1996). Application of Kalman filtering to numerical weather prediction. Workshop on non-linear aspects of data assimilation, Shinfield Park, Reading, ECMWF.

Budyko, M. I. (1969). "The effect of solar radiation variations on the climate of the Earth." Tellus **21**(5): 611-619 DOI: 10.3402/tellusa.v21i5.10109.

Buizza, R., M. Milleer and T. N. Palmer (1999). "Stochastic representation of model uncertainties in the ECMWF ensemble prediction system." Quarterly Journal of the Royal Meteorological Society **125**(560): 2887-2908 DOI: https://doi.org/10.1002/qj.49712556006.

Carré, M., J. P. Sachs, J. M. Wallace and C. Favier (2012). "Exploring errors in paleoclimate proxy reconstructions using Monte Carlo simulations: paleotemperature from mollusk and coral geochemistry." Clim. Past **8**(2): 433-450 DOI: 10.5194/cp-8-433-2012.

Chen, Z., C. Heckman, S. Julier and N. Ahmed (2018). Weak in the NEES?: Auto-Tuning Kalman Filters with Bayesian Optimization DOI: 10.23919/ICIF.2018.8454982.

Chen, Z., C. Heckman, S. J. Julier and N. R. Ahmed (2021). "Time Dependence in Kalman Filter Tuning." 2021 IEEE 24th International Conference on Information Fusion (FUSION): 1-8.

Cheng, L., K. E. Trenberth, J. Fasullo, T. Boyer, J. Abraham and J. Zhu (2017). "Improved estimates of ocean heat content from 1960 to 2015." Science Advances **3**(3): e1601545 DOI: 10.1126/sciadv.1601545.

Cheng, L., K. von Schuckmann, J. P. Abraham, K. E. Trenberth, M. E. Mann, L. Zanna, M. H. England, J. D. Zika, J. T. Fasullo, Y. Yu, Y. Pan, J. Zhu, E. R. Newsom, B. Bronselaer and X. Lin (2022). "Past and future ocean warming." Nature Reviews Earth & Environment **3**(11): 776-794 DOI: 10.1038/s43017-022-00345-1.

Coddington, O., J. L. Lean, D. Lindholm, P. Pilewskie, M. Snow and N. C. Program (2017). NOAA Climate Data Record (CDR) of Total Solar Irradiance (TSI), NRLTSI Version 2.1. N. N. C. f. E. Information DOI: https://doi.org/10.7289/V56W985W.

Collins, M., R. Knutti, J. Arblaster, J. L. Dufresne, T. Fichefet, P. Friedlingstein, X. Gao, W. J. Gutowski, T. Johns, G. Krinner, M. Shongwe, C. Tebaldi, A. J. Weaver and M. Wehner (2013). Long-term climate change: Projections, commitments and irreversibility. Climate Change 2013: The Physical Science Basis. Contribution of Working Group I to the Fifth Assessment Report of the Intergovernmental Panel on Climate Change. T. F. Stocker, D. Qin,

G. K. Plattner et al. Cambridge, UK, Cambridge University Press: 1029-1136 DOI: 10.1017/CBO9781107415324.024.

Compo, G. P., J. S. Whitaker, P. D. Sardeshmukh, N. Matsui, R. J. Allan, X. Yin, B. E. Gleason, R. S. Vose, G. Rutledge, P. Bessemoulin, S. Brönnimann, M. Brunet, R. I. Crouthamel, A. N. Grant, P. Y. Groisman, P. D. Jones, M. C. Kruk, A. C. Kruger, G. J. Marshall, M. Maugeri, H. Y. Mok, Ø. Nordli, T. F. Ross, R. M. Trigo, X. L. Wang, S. D. Woodruff and S. J. Worley (2011). "The Twentieth Century Reanalysis Project." Quarterly Journal of the Royal Meteorological Society **137**(654): 1-28 DOI: https://doi.org/10.1002/qj.776.

Duffy, M. L., B. Medeiros, A. Gettelman and T. Eidhammer (2023). "Perturbing parameters to understand cloud contributions to climate change." Journal of Climate **[Preprint]**.

Edwards, T. L., S. Nowicki, B. Marzeion, R. Hock, H. Goelzer, H. Seroussi, N. C. Jourdain, D. A. Slater, F. E. Turner, C. J. Smith, C. M. McKenna, E. Simon, A. Abe-Ouchi, J. M. Gregory, E. Larour, W. H. Lipscomb, A. J. Payne, A. Shepherd, C. Agosta, P. Alexander, T. Albrecht, B. Anderson, X. Asay-Davis, A. Aschwanden, A. Barthel, A. Bliss, R. Calov, C. Chambers, N. Champollion, Y. Choi, R. Cullather, J. Cuzzone, C. Dumas, D. Felikson, X. Fettweis, K. Fujita, B. K. Galton-Fenzi, R. Gladstone, N. R. Golledge, R. Greve, T. Hattermann, M. J. Hoffman, A. Humbert, M. Huss, P. Huybrechts, W. Immerzeel, T. Kleiner, P. Kraaijenbrink, S. Le clec'h, V. Lee, G. R. Leguy, C. M. Little, D. P. Lowry, J.-H. Malles, D. F. Martin, F. Maussion, M. Morlighem, J. F. O'Neill, I. Nias, F. Pattyn, T. Pelle, S. F. Price, A. Quiquet, V. Radić, R. Reese, D. R. Rounce, M. Rückamp, A. Sakai, C. Shafer, N.-J. Schlegel, S. Shannon, R. S. Smith, F. Straneo, S. Sun, L. Tarasov, L. D. Trusel, J. Van Breedam, R. van de Wal, M. van den Broeke, R. Winkelmann, H. Zekollari, C. Zhao, T. Zhang and T. Zwinger (2021). "Projected land ice contributions to twenty-first-century sea level rise." Nature **593**(7857): 74-82 DOI: 10.1038/s41586-021-03302-y.

Emile-Geay, J., N. P. McKay, D. S. Kaufman, L. von Gunten, J. Wang, K. J. Anchukaitis, N. J. Abram, J. A. Addison, M. A. J. Curran, M. N. Evans, B. J. Henley, Z. Hao, B. Martrat, H. V. McGregor, R. Neukom, G. T. Pederson, B. Stenni, K. Thirumalai, J. P. Werner, C. Xu, D. V. Divine, B. C. Dixon, J. Gergis, I. A. Mundo, T. Nakatsuka, S. J. Phipps, C. C. Routson, E. J. Steig, J. E. Tierney, J. J. Tyler, K. J. Allen, N. A. N. Bertler, J. Björklund, B. M. Chase, M.-T. Chen, E. Cook, R. de Jong, K. L. DeLong, D. A. Dixon, A. A. Ekaykin, V. Ersek, H. L. Filipsson, P. Francus, M. B. Freund, M. Frezzotti, N. P. Gaire, K. Gajewski, Q. Ge, H. Goosse, A. Gornostaeva, M. Grosjean, K. Horiuchi, A. Hormes, K. Husum, E. Isaksson, S. Kandasamy, K. Kawamura, K. H. Kilbourne, N. Koç, G. Leduc, H. W. Linderholm, A. M. Lorrey, V. Mikhalenko, P. G. Mortyn, H. Motoyama, A. D. Moy, R. Mulvaney, P. M. Munz, D. J. Nash, H. Oerter, T. Opel, A. J. Orsi, D. V. Ovchinnikov, T. J. Porter, H. A. Roop, C. Saenger, M. Sano, D. Sauchyn, K. M. Saunders, M.-S. Seidenkrantz, M. Severi, X. Shao, M.-A. Sicre, M. Sigl, K. Sinclair, S. St. George, J.-M. St. Jacques, M. Thamban, U. Kuwar Thapa, E. R. Thomas, C. Turney, R. Uemura, A. E. Viau, D. O. Vladimirova, E. R. Wahl, J. W. C. White, Z. Yu, J. Zinke and P. A. k. Consortium (2017). "A global multiproxy database for temperature reconstructions of the Common Era." Scientific Data **4**(1): 170088 DOI: 10.1038/sdata.2017.88.

Feng, R., B. L. Otto-Bliesner, E. C. Brady and N. Rosenbloom (2020). "Increased Climate Response and Earth System Sensitivity From CCSM4 to CESM2 in Mid-Pliocene Simulations." Journal of Advances in Modeling Earth Systems **12**(8): e2019MS002033 DOI: https://doi.org/10.1029/2019MS002033.

Filar, J. A., P. S. Gaertner and M. A. Janssen (1996). An Application of Optimization to the Problem of Climate Change. State of the Art in Global Optimization: Computational Methods and Applications. C. A. Floudas and P. M. Pardalos. Boston, MA, Springer US**:** 475-498 DOI: 10.1007/978-1-4613-3437-8_29.

Forster, P., T. Storelvmo, K. Armour, W. Collins, J. L. Dufresne, D. Frame, D. J. Lunt, T. Mauritsen, M. D. Palmer, M. Watanabe, M. Wild and H. Zhang (2021). The Earth's Energy Budget, Climate Feedbacks, and Climate Sensitivity. Climate Change 2021: The Physical Science Basis. Contribution of Working Group I to the Sixth Assessment Report of the Intergovernmental Panel on Climate Change. V. Masson-Delmotte, P. Zhai, A. Pirani et al. Cambridge, United Kingdom and New York, NY, USA, Cambridge University Press**:** 923–1054 DOI: 10.1017/9781009157896.009.

Forster, P. M., C. J. Smith, T. Walsh, W. F. Lamb, R. Lamboll, M. Hauser, A. Ribes, D. Rosen, N. Gillett, M. D. Palmer, J. Rogelj, K. von Schuckmann, S. I. Seneviratne, B. Trewin, X. Zhang, M. Allen, R. Andrew, A. Birt, A. Borger, T. Boyer, J. A. Broersma, L. Cheng, F. Dentener, P. Friedlingstein, J. M. Gutiérrez, J. Gütschow, B. Hall, M. Ishii, S. Jenkins, X. Lan, J. Y. Lee, C. Morice, C. Kadow, J. Kennedy, R. Killick, J. C. Minx, V. Naik, G. P. Peters, A. Pirani, J. Pongratz, C. F. Schleussner, S. Szopa, P. Thorne, R. Rohde, M. Rojas Corradi, D. Schumacher, R. Vose, K. Zickfeld, V. Masson-Delmotte and P. Zhai (2023). "Indicators of Global Climate Change 2022: annual update of large-scale indicators of the state of the climate system and human influence." Earth Syst. Sci. Data **15**(6): 2295-2327 DOI: 10.5194/essd-15-2295-2023.

Fox-Kemper, B., H. T. Hewitt, C. Xiao, G. Aðalgeirsdóttir, S. S. Drijfhout, T. L. Edwards, N. R. Golledge, M. Hemer, R. E. Kopp, G. Krinner, A. Mix, D. Notz, S. Nowicki, I. S. Nurhati, L. Ruiz, J. B. Sallée, A. B. A. Slangen and Y. Yu (2021). Ocean, Cryosphere and Sea Level Change. Climate Change 2021: The Physical Science Basis. Contribution of Working Group I to the Sixth Assessment Report of the Intergovernmental Panel on Climate Change. V. Masson-Delmotte, P. Zhai, A. Pirani et al. Cambridge, United Kingdom and New York, NY, USA, Cambridge University Press**:** 1211–1362 DOI: 10.1017/9781009157896.011.

Friedrich, T., A. Timmermann, M. Tigchelaar, O. Elison Timm and A. Ganopolski (2016). "Nonlinear climate sensitivity and its implications for future greenhouse warming." Science Advances **2**(11): e1501923 DOI: doi:10.1126/sciadv.1501923.

Fujimori, S., T. Hasegawa, T. Masui, K. Takahashi, D. S. Herran, H. Dai, Y. Hijioka and M. Kainuma (2017). "SSP3: AIM implementation of Shared Socioeconomic Pathways." Global Environmental Change **42**: 268-283 DOI: https://doi.org/10.1016/j.gloenvcha.2016.06.009.

Geoffroy, O., D. Saint-Martin, G. Bellon, A. Voldoire, D. J. L. Olivié and S. Tytéca (2013). "Transient Climate Response in a Two-Layer Energy-Balance Model. Part II: Representation of the Efficacy of Deep-Ocean Heat Uptake and Validation for CMIP5 AOGCMs." Journal of Climate **26**(6): 1859-1876 DOI: https://doi.org/10.1175/JCLI-D-12-00196.1.

Geoffroy, O., D. Saint-Martin, D. J. L. Olivié, A. Voldoire, G. Bellon and S. Tytéca (2013). "Transient Climate Response in a Two-Layer Energy-Balance Model. Part I: Analytical Solution and Parameter Calibration Using CMIP5 AOGCM Experiments." Journal of Climate **26**(6): 1841-1857 DOI: https://doi.org/10.1175/JCLI-D-12-00195.1.

Gerlach, T. (2011). "Volcanic versus anthropogenic carbon dioxide." Eos, Transactions, American Geophysical Union **92**(24): 201-202 DOI: 10.1029/2011EO240001.

Gettelman, A., C. Hannay, J. T. Bacmeister, R. B. Neale, A. G. Pendergrass, G. Danabasoglu, J. F. Lamarque, J. T. Fasullo, D. A. Bailey, D. M. Lawrence and M. J. Mills (2019). "High

Climate Sensitivity in the Community Earth System Model Version 2 (CESM2)." Geophysical Research Letters **46**(14): 8329-8337 DOI: https://doi.org/10.1029/2019GL083978.

Gregory, J. M. (2000). "Vertical heat transports in the ocean and their effect on time-dependent climate change." Climate Dynamics **16**(7): 501-515 DOI: 10.1007/s003820000059.

Gregory, J. M. and T. Andrews (2016). "Variation in climate sensitivity and feedback parameters during the historical period." Geophysical Research Letters **43**(8): 3911-3920 DOI: https://doi.org/10.1002/2016GL068406.

Grewal, M. S. and A. P. Andrews (2001). Kalman Filtering: Theory and Practice Using MATLAB, Wiley.

Gulev, S. K., P. W. Thorne, J. Ahn, F. J. Dentener, C. M. Domingues, S. Gerland, D. Gong, D. S. Kaufman, H. C. Nnamchi, J. Quaas, J. A. Rivera, S. Sathyendranath, S. L. Smith, B. Trewin, K. von Schuckmann and R. S. Vose (2021). Changing State of the Climate System. Climate Change 2021: The Physical Science Basis. Contribution of Working Group I to the Sixth Assessment Report of the Intergovernmental Panel on Climate Change. V. Masson-Delmotte, P. Zhai, A. Pirani et al. Cambridge, United Kingdom and New York, NY, USA, Cambridge University Press**:** 287–422 DOI: 10.1017/9781009157896.004.

Guttman, N. B. (1989). "Statistical Descriptors of Climate." Bulletin of the American Meteorological Society **70**(6): 602-607 DOI: 10.1175/1520-0477(1989)070<0602:SDOC>2.0.CO;2.

Hakim, G. J., J. Emile-Geay, E. J. Steig, D. Noone, D. M. Anderson, R. Tardif, N. Steiger and W. A. Perkins (2016). "The last millennium climate reanalysis project: Framework and first results." Journal of Geophysical Research: Atmospheres **121**(12): 6745-6764 DOI: https://doi.org/10.1002/2016JD024751.

Hall, G. and B. Fox-Kemper (2023). "Regional mixed layer depth as a climate diagnostic and emergent constraint." Geophysical Research Letters **[Preprint, personal communication]**.

Harshvardhan and M. D. King (1993). "Comparative Accuracy of Diffuse Radiative Properties Computed Using Selected Multiple Scattering Approximations." Journal of the Atmospheric Sciences **50**(2): 247-259 DOI: 10.1175/1520-0469(1993)050<0247:caodrp>2.0.co;2.

Horvat, C. (2021). "Marginal ice zone fraction benchmarks sea ice and climate model skill." Nature Communications **12**(1): 2221 DOI: 10.1038/s41467-021-22004-7.

Houtekamer, P. L. and H. L. Mitchell (1998). "Data Assimilation Using an Ensemble Kalman Filter Technique." Monthly Weather Review **126**(3): 796-811 DOI: https://doi.org/10.1175/1520-0493(1998)126<0796:DAUAEK>2.0.CO;2.

Hu, S. and A. V. Fedorov (2017). "The extreme El Niño of 2015-2016 and the end of global warming hiatus." Geophysical Research Letters **44**(8): 3816-3824 DOI: 10.1002/2017GL072908.

Huguenin, M. F., R. M. Holmes and M. H. England (2022). "Drivers and distribution of global ocean heat uptake over the last half century." Nature Communications **13**(1): 4921 DOI: 10.1038/s41467-022-32540-5.

Hummels, R., M. Dengler and B. Bourlès (2013). "Seasonal and regional variability of upper ocean diapycnal heat flux in the Atlantic cold tongue." Progress in Oceanography **111**: 52-74 DOI: https://doi.org/10.1016/j.pocean.2012.11.001.

Ishii, M., Y. Fukuda, S. Hirahara, S. Yasui, T. Suzuki and K. Sato (2017). "Accuracy of Global Upper Ocean Heat Content Estimation Expected from Present Observational Data Sets." SOLA **13**: 163-167 DOI: 10.2151/sola.2017-030.

Jones, C. D., J. E. Hickman, S. T. Rumbold, J. Walton, R. D. Lamboll, R. B. Skeie, S. Fiedler, P. M. Forster, J. Rogelj, M. Abe, M. Botzet, K. Calvin, C. Cassou, J. N. S. Cole, P. Davini, M. Deushi, M. Dix, J. C. Fyfe, N. P. Gillett, T. Ilyina, M. Kawamiya, M. Kelley, S. Kharin, T. Koshiro, H. Li, C. Mackallah, W. A. Müller, P. Nabat, T. van Noije, P. Nolan, R. Ohgaito, D. Olivié, N. Oshima, J. Parodi, T. J. Reerink, L. Ren, A. Romanou, R. Séférian, Y. Tang, C. Timmreck, J. Tjiputra, E. Tourigny, K. Tsigaridis, H. Wang, M. Wu, K. Wyser, S. Yang, Y. Yang and T. Ziehn (2021). "The Climate Response to Emissions Reductions Due to COVID-19: Initial Results From CovidMIP." Geophysical Research Letters **48**(8): e2020GL091883 DOI: https://doi.org/10.1029/2020GL091883.

Jones, P. D. and C. Harpham (2013). "Estimation of the absolute surface air temperature of the Earth." Journal of Geophysical Research: Atmospheres **118**(8): 3213-3217 DOI: https://doi.org/10.1002/jgrd.50359.

Jones, P. D. and P. M. Kelly (1996). The Effect of Tropical Explosive Volcanic Eruptions on Surface Air Temperature. The Mount Pinatubo Eruption, Berlin, Heidelberg, Springer Berlin Heidelberg.

Julier, S. J. and J. K. Uhlmann (1997). New extension of the Kalman filter to nonlinear systems. Proc.SPIE DOI: 10.1117/12.280797.

Kalman, R. E. (1960). "A New Approach to Linear Filtering and Prediction Problems." Journal of Basic Engineering **82**(1): 35-45 DOI: 10.1115/1.3662552.

Kalman, R. E. and R. S. Bucy (1961). "New Results in Linear Filtering and Prediction Theory." Journal of Basic Engineering **83**(1): 95-108 DOI: 10.1115/1.3658902.

Kalnay, E. (2002). Atmospheric Modeling, Data Assimilation and Predictability. Cambridge, Cambridge University Press DOI: DOI: 10.1017/CBO9780511802270.

Kaufman, D., N. McKay, C. Routson, M. Erb, B. Davis, O. Heiri, S. Jaccard, J. Tierney, C. Dätwyler, Y. Axford, T. Brussel, O. Cartapanis, B. Chase, A. Dawson, A. De Vernal, S. Engels, L. Jonkers, J. Marsicek, P. Moffa-Sánchez, C. Morrill, A. Orsi, K. Rehfeld, K. Saunders, P. S. Sommer, E. Thomas, M. Tonello, M. Tóth, R. Vachula, A. Andreev, S. Bertrand, B. Biskaborn, M. Bringué, S. Brooks, M. Caniupán, M. Chevalier, L. Cwynar, J. Emile-Geay, J. Fegyveresi, A. Feurdean, W. Finsinger, M.-C. Fortin, L. Foster, M. Fox, K. Gajewski, M. Grosjean, S. Hausmann, M. Heinrichs, N. Holmes, B. Ilyashuk, E. Ilyashuk, S. Juggins, D. Khider, K. Koinig, P. Langdon, I. Larocque-Tobler, J. Li, A. Lotter, T. Luoto, A. Mackay, E. Magyari, S. Malevich, B. Mark, J. Massaferro, V. Montade, L. Nazarova, E. Novenko, P. Pařil, E. Pearson, M. Peros, R. Pienitz, M. Płóciennik, D. Porinchu, A. Potito, A. Rees, S. Reinemann, S. Roberts, N. Rolland, S. Salonen, A. Self, H. Seppä, S. Shala, J.-M. St-Jacques, B. Stenni, L. Syrykh, P. Tarrats, K. Taylor, V. Van Den Bos, G. Velle, E. Wahl, I. Walker, J. Wilmshurst, E. Zhang and S. Zhilich (2020). "A global database of Holocene paleotemperature records." Scientific Data **7**(1) DOI: 10.1038/s41597-020-0445-3.

Keil, P., H. Schmidt, B. Stevens and J. Bao (2021). "Variations of Tropical Lapse Rates in Climate Models and Their Implications for Upper-Tropospheric Warming." Journal of Climate **34**(24): 9747-9761 DOI: https://doi.org/10.1175/JCLI-D-21-0196.1.

Kirtman, B., S. B. Power, A. J. Adedoyin, G. J. Boer, R. Bojariu, I. Camilloni, F. Doblas-Reyes, A. M. Fiore, M. Kimoto, G. Meehl, M. Prather, A. Sarr, C. Schär, R. Sutton, G. J. van Oldenborgh, G. Vecchi and H. J. Wang (2013). Near-term climate change. Projections and predictability, Cambridge University Press. **9781107057999:** 953-1028 DOI: 10.1017/CBO9781107415324.023.

Kravitz, B., D. G. MacMartin, H. Wang and P. J. Rasch (2016). "Geoengineering as a design problem." Earth System Dynamics **7**(2): 469-497 DOI: 10.5194/esd-7-469-2016.

Kravitz, B., P. J. Rasch, H. Wang, A. Robock, C. Gabriel, O. Boucher, J. N. S. Cole, J. Haywood, D. Ji, A. Jones, A. Lenton, J. C. Moore, H. Muri, U. Niemeier, S. Phipps, H. Schmidt, S. Watanabe, S. Yang and J. H. Yoon (2018). "The climate effects of increasing ocean albedo: an idealized representation of solar geoengineering." Atmos. Chem. Phys. **18**(17): 13097-13113 DOI: 10.5194/acp-18-13097-2018.

Lacey, T. (1998). "Tutorial: The kalman filter." Computer Vision.

Lauritzen, S. L. (1981). "Time Series Analysis in 1880: A Discussion of Contributions Made by T.N. Thiele." International Statistical Review / Revue Internationale de Statistique **49**(3): 319-331 DOI: 10.2307/1402616.

Lauritzen, S. L. and T. N. Thiele (2002). Thiele: Pioneer in Statistics, Oxford University Press.

Lee, J. H. and N. L. Ricker (1994). "Extended Kalman Filter Based Nonlinear Model Predictive Control." Industrial and Engineering Chemistry Research **33**(6): 1530-1541 DOI: 10.1021/ie00030a013.

Lee, J. Y., J. Marotzke, G. Bala, L. Cao, S. Corti, J. P. Dunne, F. Engelbrecht, E. Fischer, J. C. Fyfe, C. Jones, A. Maycock, J. Mutemi, O. Ndiaye, S. Panickal and T. Zhou (2021). Future Global Climate: Scenario-Based Projections and Near-Term Information. Climate Change 2021: The Physical Science Basis. Contribution of Working Group I to the Sixth Assessment Report of the Intergovernmental Panel on Climate Change. V. Masson-Delmotte, P. Zhai, A. Pirani et al. Cambridge, United Kingdom and New York, NY, USA, Cambridge University Press**:** 553–672 DOI: 10.1017/9781009157896.006.

Lenssen, N. J. L., G. A. Schmidt, J. E. Hansen, M. J. Menne, A. Persin, R. Ruedy and D. Zyss (2019). "Improvements in the GISTEMP Uncertainty Model." Journal of Geophysical Research: Atmospheres **124**(12): 6307-6326 DOI: https://doi.org/10.1029/2018JD029522.

Loeb, N. G., B. A. Wielicki, D. R. Doelling, G. L. Smith, D. F. Keyes, S. Kato, N. Manalo-Smith and T. Wong (2009). "Toward Optimal Closure of the Earth's Top-of-Atmosphere Radiation Budget." Journal of Climate **22**(3): 748-766 DOI: 10.1175/2008jcli2637.1.

MacMartin, D. G., B. Kravitz and D. W. Keith (2014). Geoengineering: The world's largest control problem. 2014 American Control Conference, IEEE.

Marotzke, J. and P. M. Forster (2015). "Forcing, feedback and internal variability in global temperature trends." Nature **517**(7536): 565-570 DOI: 10.1038/nature14117.

McClelland, H. L. O., I. Halevy, D. A. Wolf-Gladrow, D. Evans and A. S. Bradley (2021). "Statistical Uncertainty in Paleoclimate Proxy Reconstructions." Geophysical Research Letters **48**(15): e2021GL092773 DOI: https://doi.org/10.1029/2021GL092773.

McCormick, M. P., L. W. Thomason and C. R. Trepte (1995). "Atmospheric effects of the Mt Pinatubo eruption." Nature **373**(6513): 399-404 DOI: 10.1038/373399a0.

McDougall, T. J., P. M. Barker, R. M. Holmes, R. Pawlowicz, S. M. Griffies and P. J. Durack (2021). "The interpretation of temperature and salinity variables in numerical ocean model output and the calculation of heat fluxes and heat content." Geosci. Model Dev. **14**(10): 6445-6466 DOI: 10.5194/gmd-14-6445-2021.

Meehl, G. A., R. Moss, K. E. Taylor, V. Eyring, R. J. Stouffer, S. Bony and B. Stevens (2014). "Climate Model Intercomparisons: Preparing for the Next Phase." Eos, Transactions American Geophysical Union **95**(9): 77-78 DOI: https://doi.org/10.1002/2014EO090001.

Meinshausen, M., Z. R. J. Nicholls, J. Lewis, M. J. Gidden, E. Vogel, M. Freund, U. Beyerle, C. Gessner, A. Nauels, N. Bauer, J. G. Canadell, J. S. Daniel, A. John, P. B. Krummel, G. Luderer, N. Meinshausen, S. A. Montzka, P. J. Rayner, S. Reimann, S. J. Smith, M. van den Berg, G. J. M. Velders, M. K. Vollmer and R. H. J. Wang (2020). "The shared socio-economic pathway (SSP) greenhouse gas concentrations and their extensions to 2500." Geosci. Model Dev. **13**(8): 3571-3605 DOI: 10.5194/gmd-13-3571-2020.

Merchant, C. J., O. Embury, C. E. Bulgin, T. Block, G. K. Corlett, E. Fiedler, S. A. Good, J. Mittaz, N. A. Rayner, D. Berry, S. Eastwood, M. Taylor, Y. Tsushima, A. Waterfall, R. Wilson and C. Donlon (2019). "Satellite-based time-series of sea-surface temperature since 1981 for climate applications." Scientific Data **6**(1) DOI: 10.1038/s41597-019-0236-x.

Miller, R. N. (1996). Introduction to the Kalman filter. Seminar on Data Assimilation, 2-6 September 1996, Shinfield Park, Reading, ECMWF.

Montgomery, D. C. and G. C. Runger (2013). Applied Statistics and Probability for Engineers. New York, NY, John Wiley & Sons.

Morice, C. P., J. J. Kennedy, N. A. Rayner, J. P. Winn, E. Hogan, R. E. Killick, R. J. H. Dunn, T. J. Osborn, P. D. Jones and I. R. Simpson (2021). "An Updated Assessment of Near-Surface Temperature Change From 1850: The HadCRUT5 Data Set." Journal of Geophysical Research: Atmospheres **126**(3): e2019JD032361 DOI: https://doi.org/10.1029/2019JD032361.

Myers, M. A. and R. H. Luecke (1991). "Process control applications of an extended Kalman filter algorithm." Computers & Chemical Engineering **15**(12): 853-857 DOI: https://doi.org/10.1016/0098-1354(91)80030-Y.

Nasa/Larc/Sd/Asdc (2018). Global Space-based Stratospheric Aerosol Climatology Version 2.0.

Nazarenko, L. S., N. Tausnev, G. L. Russell, D. Rind, R. L. Miller, G. A. Schmidt, S. E. Bauer, M. Kelley, R. Ruedy, A. S. Ackerman, I. Aleinov, M. Bauer, R. Bleck, V. Canuto, G. Cesana, Y. Cheng, T. L. Clune, B. I. Cook, C. A. Cruz, A. D. Del Genio, G. S. Elsaesser, G. Faluvegi, N. Y. Kiang, D. Kim, A. A. Lacis, A. Leboissetier, A. N. LeGrande, K. K. Lo, J. Marshall, E. E. Matthews, S. McDermid, K. Mezuman, L. T. Murray, V. Oinas, C. Orbe, C. P. García-Pando, J. P. Perlwitz, M. J. Puma, A. Romanou, D. T. Shindell, S. Sun, K. Tsigaridis, G. Tselioudis, E. Weng, J. Wu and M.-S. Yao (2022). "Future Climate Change Under SSP Emission Scenarios With GISS-E2.1." Journal of Advances in Modeling Earth Systems **14**(7): e2021MS002871 DOI: https://doi.org/10.1029/2021MS002871.

Newsom, E., L. Zanna and J. M. Gregory (2023). Background Pycnocline depth constrains Future Ocean Heat Uptake Efficiency. arXiv DOI: 10.48550/arXiv.2307.11902.

Ogorek, B. (2019) "Yet Another Kalman Filter Explanation Article." Towards Data Science.

Okada, M., K. Yamanishi and N. Masuda (2020). "Long-tailed distributions of inter-event times as mixtures of exponential distributions." Royal Society Open Science **7**: 191643 DOI: 10.1098/rsos.191643.

Palmer, M., G. Harris and J. Gregory (2018). "Extending CMIP5 projections of global mean temperature change and sea level rise due to thermal expansion using a physically-based emulator." Environmental Research Letters **13** DOI: 10.1088/1748-9326/aad2e4.

Papale, P. (2018). "Global time-size distribution of volcanic eruptions on Earth." Scientific Reports **8**(1): 6838 DOI: 10.1038/s41598-018-25286-y.

Pielke Jr, R., M. G. Burgess and J. Ritchie (2022). "Plausible 2005–2050 emissions scenarios project between 2 °C and 3 °C of warming by 2100." Environmental Research Letters **17**(2): 024027 DOI: 10.1088/1748-9326/ac4ebf.

Quevedo, H. and G. Gonzalez (2017). "Non-normal Distribution of Temperatures in the United States of America during 1895-2016: A Challenge to the Central Limit Theorem." Pinnacle Environmental & Earth Sciences **4**: 1182.

Rauch, H. E., F. Tung and C. T. Striebel (1965). "Maximum likelihood estimates of linear dynamic systems." AIAA Journal **3**(8): 1445-1450 DOI: 10.2514/3.3166.

Roach, L. A., J. Dörr, C. R. Holmes, F. Massonnet, E. W. Blockley, D. Notz, T. Rackow, M. N. Raphael, S. P. O'Farrell, D. A. Bailey and C. M. Bitz (2020). "Antarctic Sea Ice Area in CMIP6." Geophysical Research Letters **47**(9): e2019GL086729 DOI: https://doi.org/10.1029/2019GL086729.

Rodgers, K. B., S. S. Lee, N. Rosenbloom, A. Timmermann, G. Danabasoglu, C. Deser, J. Edwards, J. E. Kim, I. R. Simpson, K. Stein, M. F. Stuecker, R. Yamaguchi, T. Bódai, E. S. Chung, L. Huang, W. M. Kim, J. F. Lamarque, D. L. Lombardozzi, W. R. Wieder and S. G. Yeager (2021). "Ubiquity of human-induced changes in climate variability." Earth Syst. Dynam. **12**(4): 1393-1411 DOI: 10.5194/esd-12-1393-2021.

Rosenblum, E. and I. Eisenman (2017). "Sea Ice Trends in Climate Models Only Accurate in Runs with Biased Global Warming." Journal of Climate **30**(16): 6265-6278 DOI: https://doi.org/10.1175/JCLI-D-16-0455.1.

Sætrom, J. and H. Omre (2013). "Uncertainty Quantification in the Ensemble Kalman Filter." Scandinavian Journal of Statistics **40**(4): 868-885 DOI: 10.111/sjos.12039.

Särkkä, S. (2013). Bayesian Filtering and Smoothing, Cambridge University Press.

Sato, M., J. E. Hansen, M. P. McCormick and J. B. Pollack (1993). "Stratospheric aerosol optical depths, 1850-1990." J. Geophys. Res. **98**: 22987-22994 DOI: 10.1029/93JD02553.

Schmidt, S. F. (1981). "The Kalman filter - Its recognition and development for aerospace applications." Journal of Guidance and Control **4**(1): 4-7 DOI: 10.2514/3.19713.

Schwartz, S. E. (2007). "Heat capacity, time constant, and sensitivity of Earth's climate system." Journal of Geophysical Research **112**(D24): D24S05-D24S05 DOI: 10.1029/2007JD008746.

Schwartz, S. E., n. Harshvardhan and C. M. Benkovitz (2002). "Influence of anthropogenic aerosol on cloud optical depth and albedo shown by satellite measurements and chemical transport modeling." Proceedings of the National Academy of Sciences **99**(4): 1784-1789 DOI: 10.1073/pnas.261712099.

Sellers, W. D. (1969). "A Global Climatic Model Based on the Energy Balance of the Earth-Atmosphere System." Journal of Applied Meteorology (1962-1982) **8**(3): 392-400.

Smith, C. J., P. M. Forster, S. Berger, W. Collins, B. Hall, D. Lunt, M. D. Palmer, M. Watanabe, M. Cain, G. Harris, N. J. Leach, M. Ringer and M. Zelinka (2021). Figure and data generation for Chapter 7 of the IPCC's Sixth Assessment Report, Working Group 1 (plus assorted other contributions). I. P. o. C. Change DOI: https://doi.org/10.5281/zenodo.5211357.

Smith, S. W. (2003). Chapter 15 - Moving Average Filters. Digital Signal Processing. S. W. Smith. Boston, Newnes**:** 277-284 DOI: https://doi.org/10.1016/B978-0-7506-7444-7/50052-2.

Soden, B. J., R. T. Wetherald, G. L. Stenchikov and A. Robock (2002). "Global Cooling After the Eruption of Mount Pinatubo: A Test of Climate Feedback by Water Vapor." Science **296**(5568): 727-730 DOI: doi:10.1126/science.296.5568.727.

Stratonovich, R. L. (1959). "Optimum nonlinear systems which bring about a separation of a signal with constant parameters from noise." Radiofizika **2**(6): 892-901.

Stratonovich, R. L. (1960). "Application of the Markov processes theory to optimal filtering." Radio Engineering and Electronic Physics **5**(11): 1-19.

Susskind, J., G. A. Schmidt, J. N. Lee and L. Iredell (2019). "Recent global warming as confirmed by AIRS." Environmental Research Letters **14**(4): 044030 DOI: 10.1088/1748-9326/aafd4e.

Swerling, P. (1959). First-Order Error Propagation in a Stagewise Smoothing Procedure for Satellite Observations. Santa Monica, CA, RAND Corporation.

Tebaldi, C., K. Debeire, V. Eyring, E. Fischer, J. Fyfe, P. Friedlingstein, R. Knutti, J. Lowe, B. O'Neill, B. Sanderson, D. van Vuuren, K. Riahi, M. Meinshausen, Z. Nicholls, K. B. Tokarska, G. Hurtt, E. Kriegler, J. F. Lamarque, G. Meehl, R. Moss, S. E. Bauer, O. Boucher, V. Brovkin, Y. H. Byun, M. Dix, S. Gualdi, H. Guo, J. G. John, S. Kharin, Y. Kim, T. Koshiro, L. Ma, D. Olivié, S. Panickal, F. Qiao, X. Rong, N. Rosenbloom, M. Schupfner, R. Séférian, A. Sellar, T. Semmler, X. Shi, Z. Song, C. Steger, R. Stouffer, N. Swart, K. Tachiiri, Q. Tang, H. Tatebe, A. Voldoire, E. Volodin, K. Wyser, X. Xin, S. Yang, Y. Yu and T. Ziehn (2021). "Climate model projections from the Scenario Model Intercomparison Project (ScenarioMIP) of CMIP6." Earth Syst. Dynam. **12**(1): 253-293 DOI: 10.5194/esd-12-253-2021.

Tebaldi, C. and R. Knutti (2018). "Evaluating the accuracy of climate change pattern emulation for low warming targets." Environmental Research Letters **13** DOI: 10.1088/1748-9326/aabef2.

van Katwyk, P., B. Fox-Kemper, H. Seroussi, S. Nowicki and K. J. Bergen (2023). "A variational LSTM emulator of sea level contribution from the Antarctic ice sheet." Journal of Advances in Modeling Earth Systems **Submitted**.

van Vuuren, D. P., M. G. J. den Elzen, P. L. Lucas, B. Eickhout, B. J. Strengers, B. van Ruijven, S. Wonink and R. van Houdt (2007). "Stabilizing greenhouse gas concentrations at low levels: an assessment of reduction strategies and costs." Climatic Change **81**(2): 119-159 DOI: 10.1007/s10584-006-9172-9.

van Vuuren, D. P., E. Stehfest, D. E. H. J. Gernaat, J. C. Doelman, M. van den Berg, M. Harmsen, H. S. de Boer, L. F. Bouwman, V. Daioglou, O. Y. Edelenbosch, B. Girod, T. Kram, L. Lassaletta, P. L. Lucas, H. van Meijl, C. Müller, B. J. van Ruijven, S. van der Sluis and A. Tabeau (2017). "Energy, land-use and greenhouse gas emissions trajectories under a green growth paradigm." Global Environmental Change **42**: 237-250 DOI: https://doi.org/10.1016/j.gloenvcha.2016.05.008.

Vernier, J., L. Thomason, J. P. Pommereau, A. Bourassa, J. Pelon, A. Garnier, A. Hauchecorne, L. Blanot, C. Trepte, D. Degenstein and F. Vargas (2011). "Major influence of tropical volcanic eruptions on the stratospheric aerosol layer during the last decade." GEOPHYSICAL RESEARCH LETTERS **38** DOI: 10.1029/2011GL047563.

Wan, E. A. and R. Van Der Merwe (2000). The unscented Kalman filter for nonlinear estimation, Institute of Electrical and Electronics Engineers Inc. DOI: 10.1109/ASSPCC.2000.882463.

Wielicki, B. A., B. R. Barkstrom, E. F. Harrison, R. B. Lee, G. Louis Smith and J. E. Cooper (1996). "Clouds and the Earth's Radiant Energy System (CERES): An Earth Observing System Experiment." Bulletin of the American Meteorological Society **77**(5): 853-868 DOI: 10.1175/1520-0477(1996)077<0853:catere>2.0.co;2.

Wild, M., D. Folini, M. Z. Hakuba, C. Schär, S. I. Seneviratne, S. Kato, D. Rutan, C. Ammann, E. F. Wood and G. König-Langlo (2015). "The energy balance over land and oceans: an assessment based on direct observations and CMIP5 climate models." Climate Dynamics **44**(11): 3393-3429 DOI: 10.1007/s00382-014-2430-z.

Wild, M., M. Z. Hakuba, D. Folini, P. Dörig-Ott, C. Schär, S. Kato and C. N. Long (2019). "The cloud-free global energy balance and inferred cloud radiative effects: an assessment based on direct observations and climate models." Climate Dynamics **52**(7): 4787-4812 DOI: 10.1007/s00382-018-4413-y.

Willner, D., C.-B. Chang and K.-P. Dunn (1977). Kalman filter algorithms for a multi-sensor system DOI: 10.1109/CDC.1976.267794.

Winton, M., K. Takahashi and I. M. Held (2010). "Importance of Ocean Heat Uptake Efficacy to Transient Climate Change." Journal of Climate **23**(9): 2333-2344 DOI: https://doi.org/10.1175/2009JCLI3139.1.

Wunsch, C. (2020). "Is the Ocean Speeding Up? Ocean Surface Energy Trends." Journal of Physical Oceanography **50**(11): 3205-3217 DOI: 10.1175/jpo-d-20-0082.1.

Wunsch, C. and P. Heimbach (2007). "Practical global oceanic state estimation." Physica D: Nonlinear Phenomena **230**(1): 197-208 DOI: https://doi.org/10.1016/j.physd.2006.09.040.

Yang, S., Z. Li, J.-Y. Yu, X. Hu, W. Dong and S. He (2018). "El Niño–Southern Oscillation and its impact in the changing climate." National Science Review **5**(6): 840-857 DOI: 10.1093/nsr/nwy046.

Youngjoo, K. and B. Hyochoong (2018). Introduction to Kalman Filter and Its Applications. Introduction and Implementations of the Kalman Filter. G. Felix. Rijeka, IntechOpen DOI: 10.5772/intechopen.80600.

Zanna, L., S. Khatiwala, J. M. Gregory, J. Ison and P. Heimbach (2019). "Global reconstruction of historical ocean heat storage and transport." Proceedings of the National Academy of Sciences **116**(4): 1126-1131 DOI: 10.1073/pnas.1808838115.

Zhang, A. and M. Atia (2020). "An Efficient Tuning Framework for Kalman Filter Parameter Optimization using Design of Experiments and Genetic Algorithms." Navigation - Journal of The Institute of Navigation **In press** DOI: 10.1002/navi.399.

Zhong, W. and J. Haigh (2013). "The greenhouse effect and carbon dioxide." Weather **68**: 100-105 DOI: 10.1002/wea.2072.

Zhu, J., B. L. Otto-Bliesner, E. C. Brady, A. Gettelman, J. T. Bacmeister, R. B. Neale, C. J. Poulsen, J. K. Shaw, Z. S. McGraw and J. E. Kay (2022). "LGM Paleoclimate Constraints Inform Cloud Parameterizations and Equilibrium Climate Sensitivity in CESM2." Journal of Advances in Modeling Earth Systems **14**(4): e2021MS002776 DOI: https://doi.org/10.1029/2021MS002776.

This manuscript has been submitted for publication to JOURNAL OF CLIMATE (AMS). Please note that this manuscript has yet to undergo a second round of peer review or be formally accepted for publication. Subsequent versions of this manuscript may differ slightly in content.

SUPPLEMENT TO

# Efficient Estimation of Climate State and Its Uncertainty Using Kalman Filtering with Application to Policy Thresholds and Volcanism


J. Matthew Nicklas,[a] Baylor Fox-Kemper,[a] Charles Lawrence.[a]

[a] *Brown University, Providence, Rhode Island.*

*Corresponding author*: J. Matthew Nicklas, john_nicklas@brown.edu


## *Section A: RTS Smoother*

$$\hat{\hat{K}}_n = \mathrm{P}_n \Phi_n (\mathrm{P}_{n|n-1})^{-1} \quad \text{back-updated Kalman gain} \quad \text{(SA1)}$$

$$\hat{\hat{x}}_n = \hat{x}_n + \hat{\hat{K}}_n \left(\hat{\hat{\mathrm{x}}}_\mathrm{n} - \mathbf{F}(\hat{x}_n; u_{n+1})\right) \quad \text{back-updated state estimate} \quad \text{(SA2)}$$

$$\hat{\hat{P}}_n = \mathrm{P}_n + \hat{\hat{K}}_n (\hat{\hat{P}}_{n+1} - \mathrm{P}_{n|n-1}) \hat{\hat{K}}_n^{\mathrm{T}} \quad \text{back-updated state covariance} \quad \text{(SA3)}$$

This RTS has a theoretical advantage of blending abrupt changes in the model state over greater time periods, while also slightly reducing the state covariance. For instance, if the measurements suddenly and persistently diverged from the blind, forward EBM (unrelated to a known volcanic eruption), an EBM-Kalman Filter model state would only react as these measurements diverge, whereas an EBM-RTS would slightly foreshadow this jump because it can see future as well as past measurements. This occurred in 1900: even though the EBM-KF estimated state is trending up, the EBM-RTS state moves cooler to reflect the colder GMST measurements from 1902-1907, colder than the EBM predicted from the Santa Marina volcanic eruption alone (see Fig. 2). Generally, the EBM-RTS just provides a second “nudge” toward measurements. However, for the purposes of this paper, these distinctions make little difference between $\hat{\hat{\boldsymbol{x}}}_{\boldsymbol{n}}$ and $\hat{\boldsymbol{x}}_\mathrm{n}$, as is demonstrated in Supp. Fig. 1 below.

## *Section B: Miscellaneous Additional Figures*

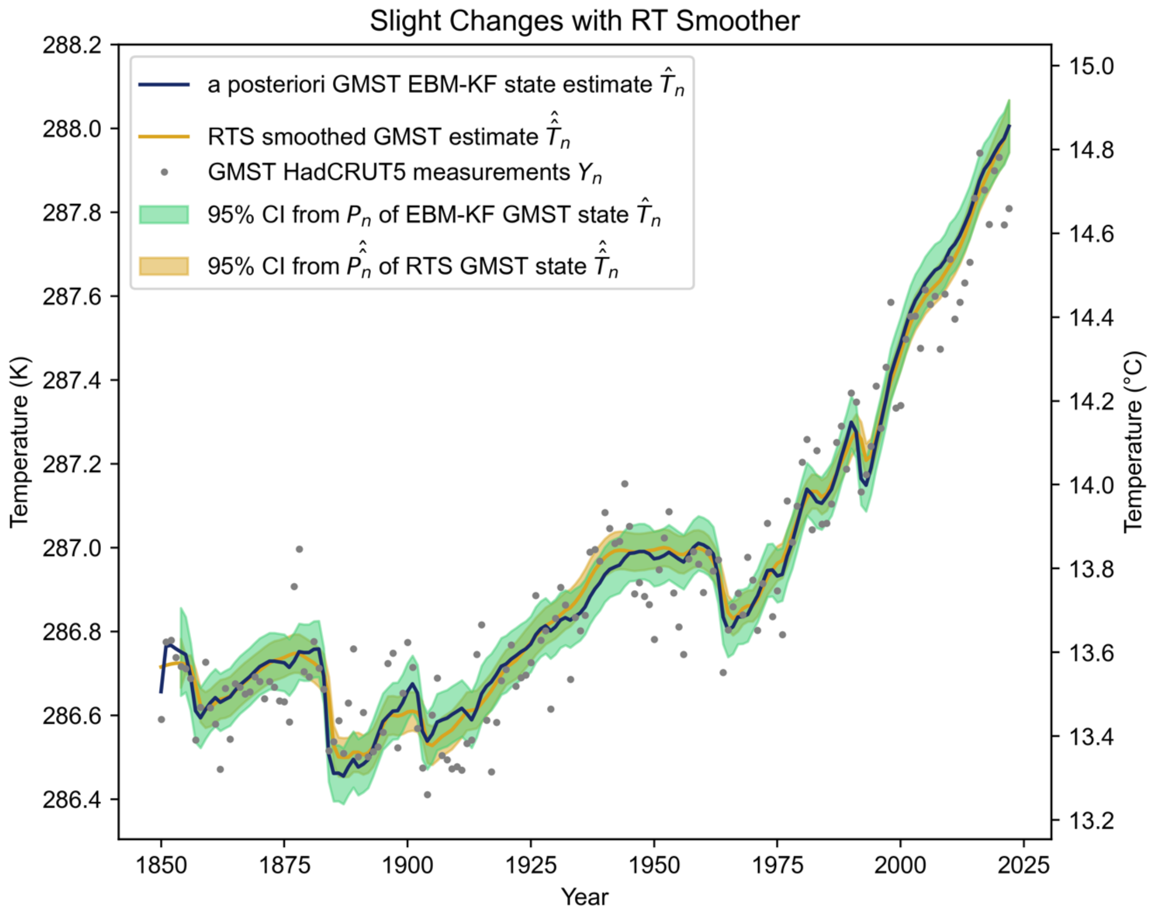


Supp. Fig. 1: Comparisons of the original EBM-Kalman Filtered climate state (navy blue line with green 1σ uncertainty window) with an EBM-RTS climate state (orange line with orange 95% uncertainty window). Note that the temperatures on y-axis are zoomed in relative to all other figures to demonstrate these minute differences. From 1905-1930 and 2000-2020 when there are repeated cooler GMST temperature measurements than the EMB-KF state prediction, the EBM-RTS climate state doubly takes these annual temperature measurements into account, so it has a greater cooling deflection in these periods. Other years are warmer in the EBM-RTS than the EBM-KF climate state, although even these differences are slight - at most 0.1K during years of volcanic activity. However, there is greater certainty in the state estimate with the EBM-RTS: $\hat{\hat{P}}_n$ shrinks relative to $P_n$ (see Supp. Fig. 10) by factors of 2.25 and 2.84 for the GMST and OHCA components respectively (everywhere except at the start and tail end of the timeseries). The off-diagonal heat-transfer uncertainty component of $\hat{\hat{P}}_n$ is negative and 29 times smaller than those of $P_n$.

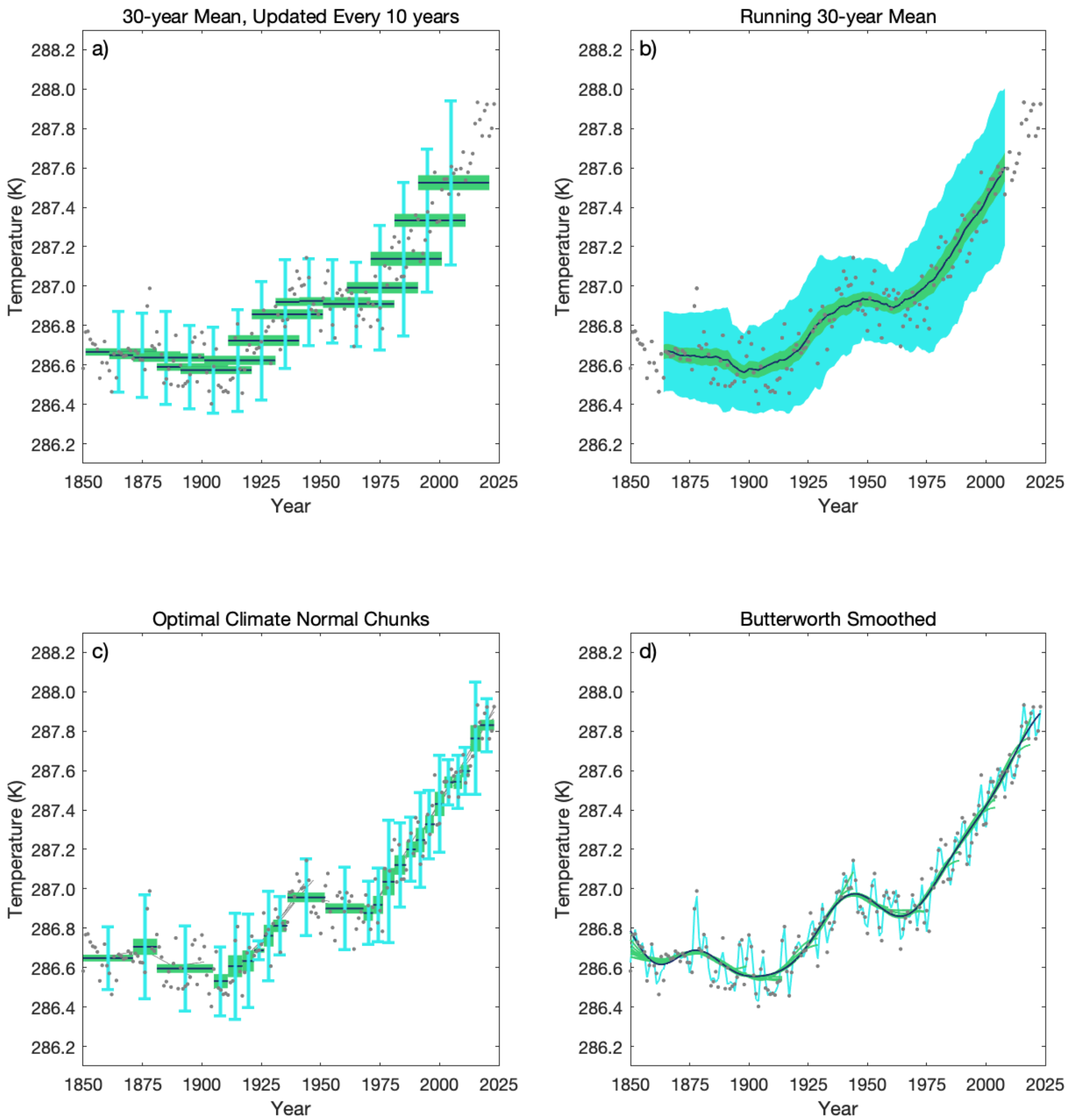


Supp. Fig. 2: Comparison of Prior Methods for Filtering or Smoothing the Climate as applied to the HadCRUT5 temperature dataset. (Morice, Kennedy et al. 2021) All metrics analogous to standard deviation are plotted at the 2σ level in light blue, and all metrics analogous to the standard error are plotted at the 1σ level in light green.  a) The 30-year climate normals, updated every 10 years as per the World Meteorological Association in 1935. b) A running 30-year average. c) Adaptive periods of multiyear averages, known as the optimal climate normal (OCN). (Livezey, Vinnikov et al. 2007). Chunks became smaller as the rate of climate change increased in recent decades. d) The Butterworth Smoother applied to this temperature dataset. (Mann 2008) For the “standard error” highly smoothed lines, the lowpass adaptive, lowpass mean padded, and lowpass methods were applied to chunks of the timeseries data ranging from 50 to 170 years in increments of 15 years with a cutoff frequency of 1/30years. The black “best” line a lowpass adaptive curve extended to 2021. The blue “standard deviation” line is a lowpass mean padded filter with a cutoff frequency of 1/5years.

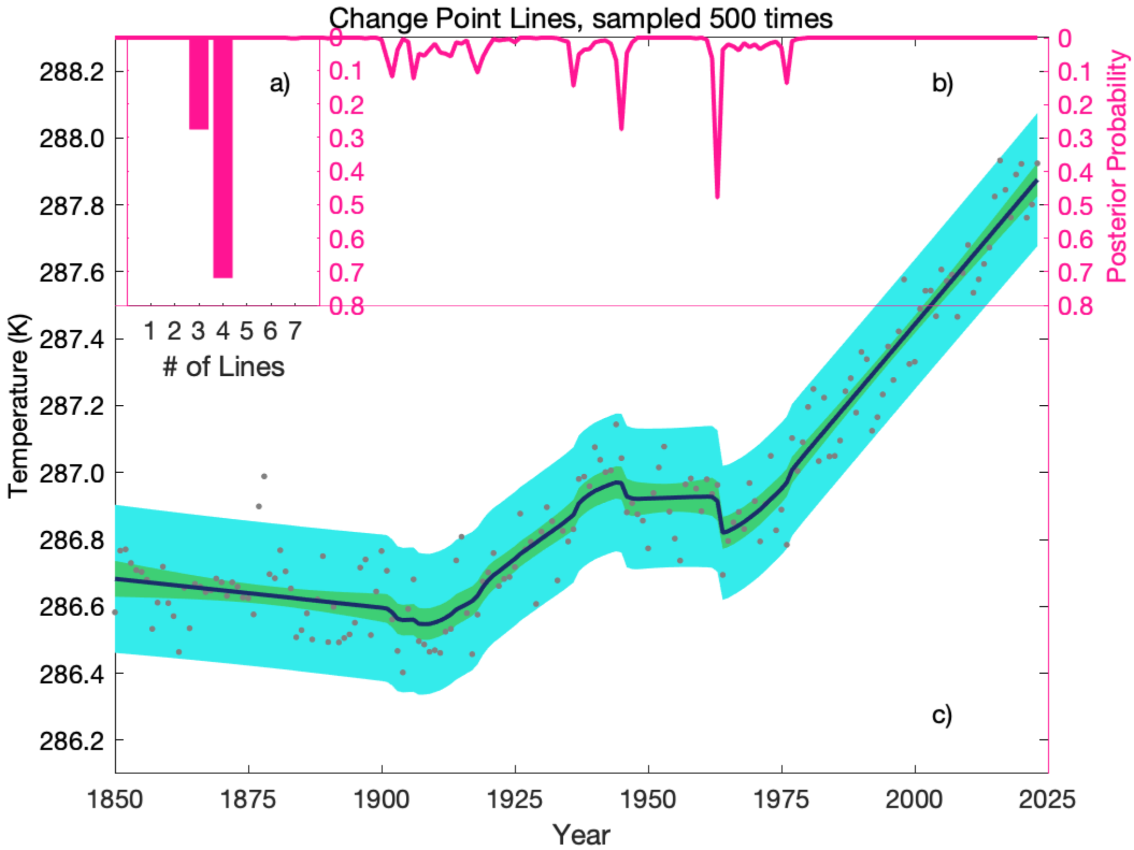


Supp. Fig. 3: Utilization of Bayesian Change Point on the HadCRUT5 data. (Ruggieri and Antonellis 2016) a) There are likely 4 trendlines with 72% of the posterior probability, and the remaining posterior probability on 3 trendlines. b) The posterior probability plot of where trendlines are most likely to occur: 51.2% of all samplings have a change point occur in 1963, and 26.4% of samplings have a change point occur in 1945. c) The posterior distribution of the trendlines in GMST, again with blue shading to indicate 2σ confidence interval of the data and green shading to indicate 2σ confidence interval of the mean trendline. These trend lines do not have to be continuous (note the dip at 1963), but over many samplings the average trend is smoothed.

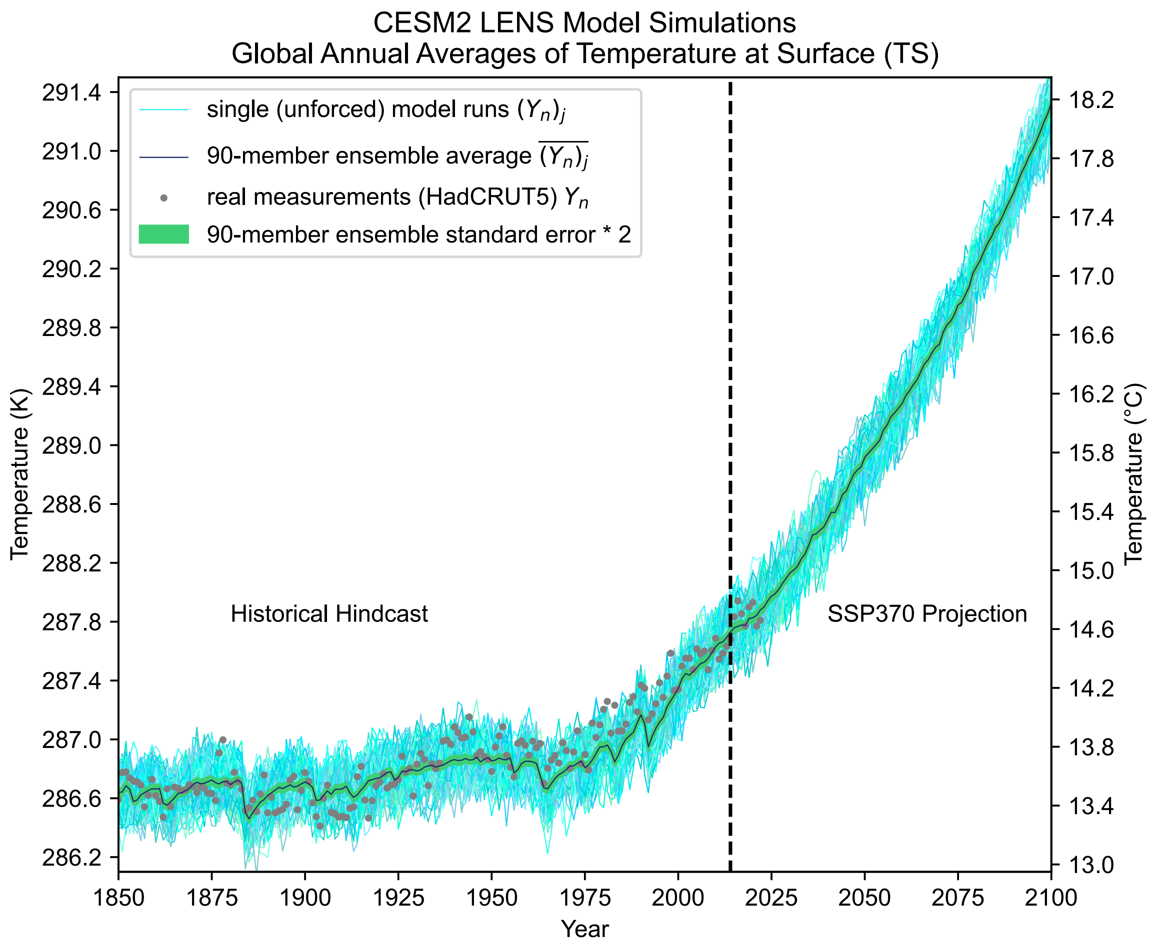


Supp. Fig. 4: Comparison of the CESM2 Large Ensemble (LENS2) GSAT (Rodgers, Lee et al. 2021) with HadCRUT5 GMST measurements. The various shades of thin light blue and turquoise lines represent each individual simulation $(Y_n)_j$ of the 90-member ensemble. The ensemble mean is plotted in a navy-blue line, and the ensemble mean standard error is plotted around this line in green. This standard error is twice the standard deviation divided by the square root of the number of ensemble members at that moment and shows the 2σ uncertainty in the yearly simulated climate is roughly 0.026K. The ensemble mean has $r^2 = 0.83$ relative to the HadCRUT5 measurements, lower than for the blind EBM ($r^2$=0.88). The dashed vertical line represents when LENS transitions from historical to future forcing (SSP3-7.0).

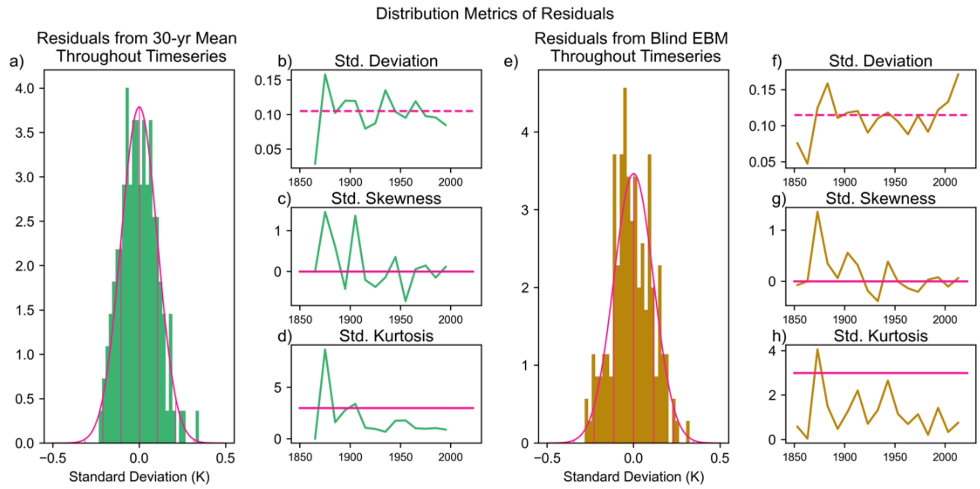


Supp. Fig. 5: Left panels show statistical features of the residuals between the HadCRUT5 measurements with respect to their 30-year running mean, which have a bias of -0.00339K. Pink lines in the histogram in (a) depict an ideal Gaussian distribution with standard deviation of 0.105K, and vertical lines drawn for each of these standard deviations. The dashed pink line (b) indicates the overall standard deviation. Solid pink lines for the skewness = 0.147 (c) and kurtosis = 1.904 (d) indicate the ideal values for a Gaussian distribution.
Right panels show statistical features of the differences between the HadCRUT5 measurements with respect to the blind EBM, which have a bias of -0.00104K. Pink lines in the histogram in (e) depict an ideal Gaussian distribution with standard deviation of 0.115K, and vertical lines drawn for each of these standard deviations. The dashed pink line (f) indicates the overall standard deviation. The skewness = 0.123 (g) and kurtosis = 1.208 (h) differ from the ideal values for a Gaussian distribution indicated by solid pink lines.

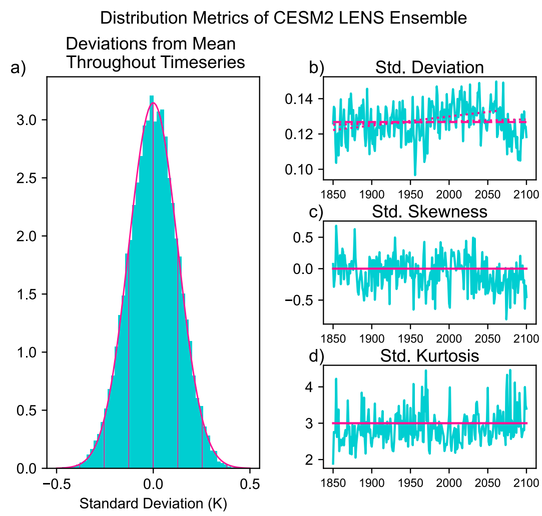


Supp. Fig. 6: Statistical Features of the CESM2 Large Ensemble. (Rodgers, Lee et al. 2021). Pink lines in the histogram in (a) depict an ideal Gaussian distribution with standard deviation of 0.127K, and vertical lines drawn for each of these standard deviations. The observed trend (b) up until 2065 ($p<0.001$) and overall ($p=0.168$) in the standard deviation over time is plotted in a dotted pink, while the dashed line indicates the overall standard deviation of 0.127K. The skewness = -0.069 (c) and kurtosis = 2.87 (d) differ from the ideal values for a Gaussian distribution indicated by solid pink lines.

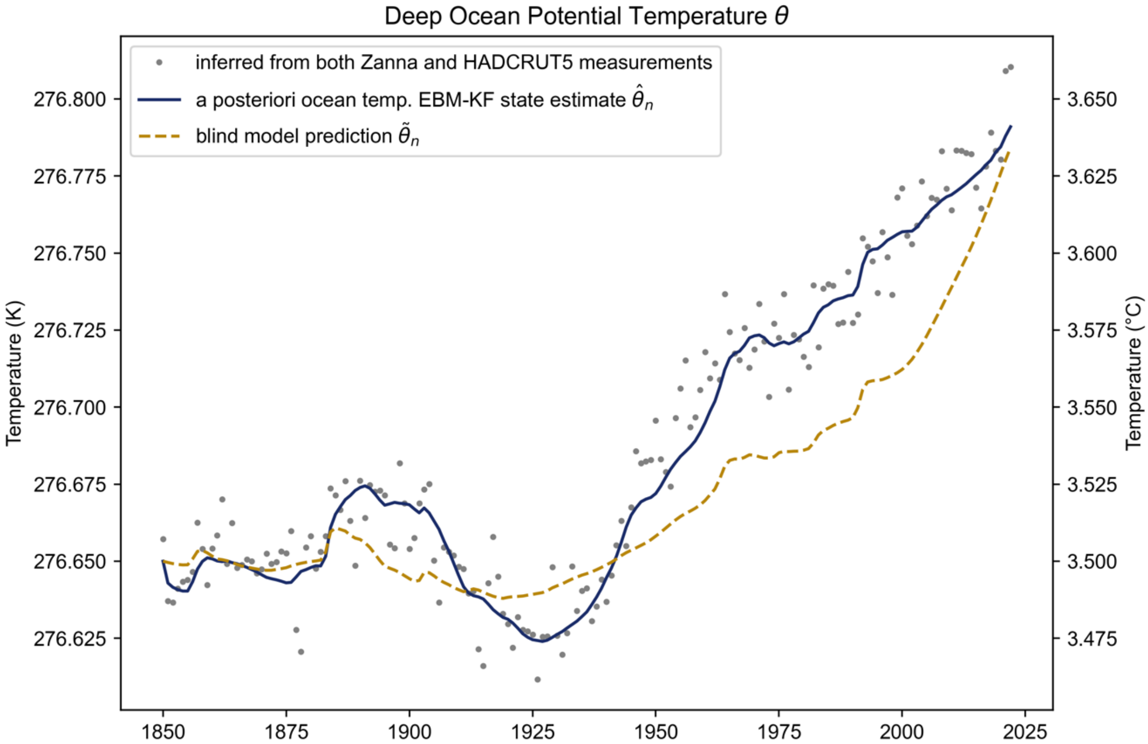


Supp. Fig. 7: As in Fig. 2, but regarding the deep ocean potential temperature. A comparison of the blind model EBM, the a posteriori EKF state estimate, and the inferred deep ocean potential by combining the Zanna (2019) and HadCRUT5 measurements with the surface and deep ocean heat capacities specified in Section 2a and Appendix A.

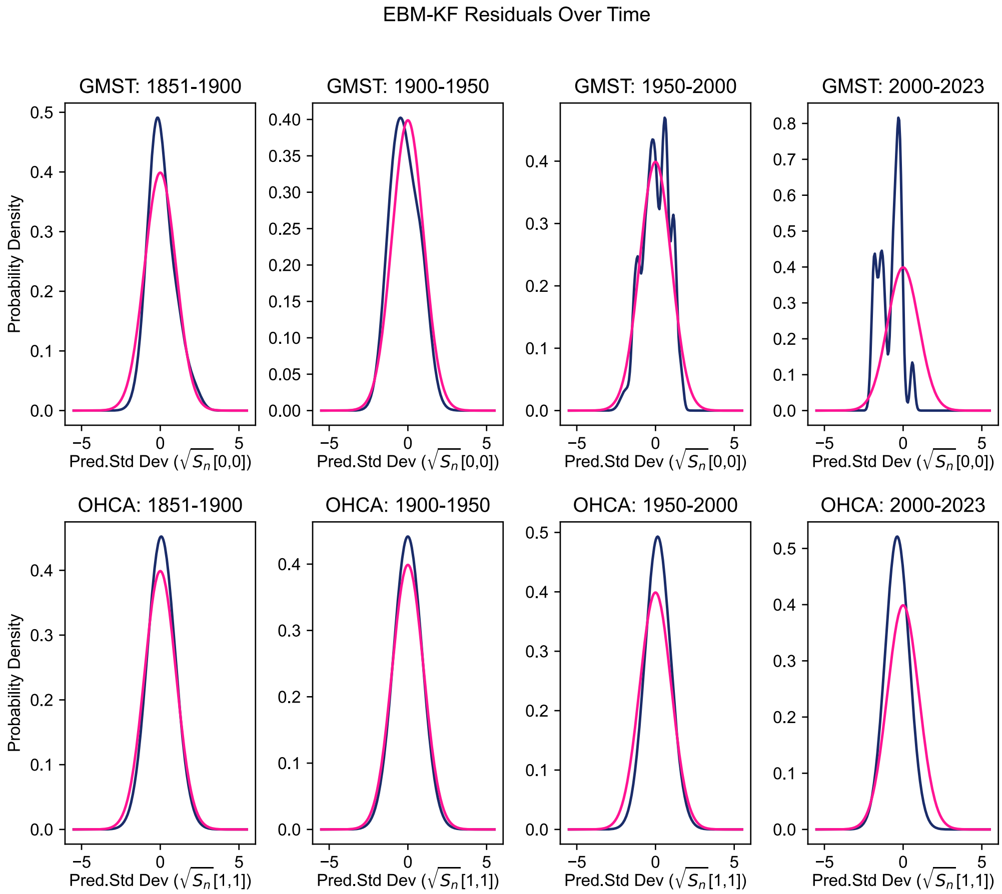


Supp. Fig. 8: Deviation between the projected climate state (pink) and empirical PDFs of the Gaussian mixture of measurements with associated uncertainty (purple), plotted relative to the ideal distribution given by the innovation covariance. Each column indicates a different time window of the EMB-KF model's run length. The top row displays the empirical PDFs of the GMST HadCRUT measurements relative to the model's estimate of GMST state, whereas the bottom row displays empirical PDFs of the OHCA Zanna 2019 measurements relative to the model's estimate of OHCA state. Note the initial period begins at 1851 (and the 1850 measurement is excluded from main text Fig. 3 and 4) because this has comparison involves $P_0$, which was intentionally over-estimated (resulting in relatively too-narrow measurement kernel). Also note that the last period is less than half the time of the others, so the GMST empirical distribution is much choppier. The observations from this most recent period 2000-2023 are also shifted slightly colder than the EMB-KF predictions, possibly indicating that some of the parameters could be better tuned than the original literature values.

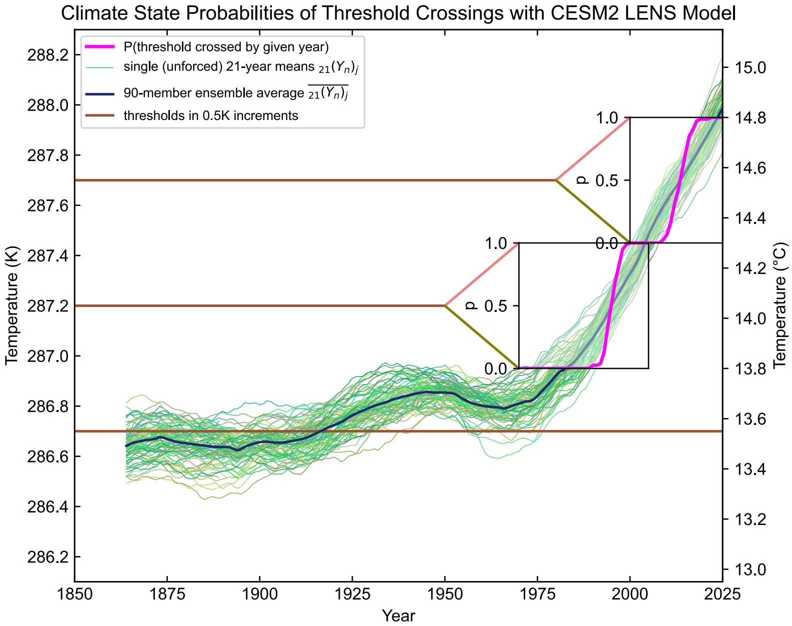


Supp. Fig. 9: As in Fig. 5 within the main text, except the climate state policy threshold crossing calculations are performed on the LENS2 ensemble. The 21-year running means of individual simulations in light green lines, the two inset boxes indicate threshold crossing probability, given by the fraction of these light green lines that have crossed the indicated threshold.

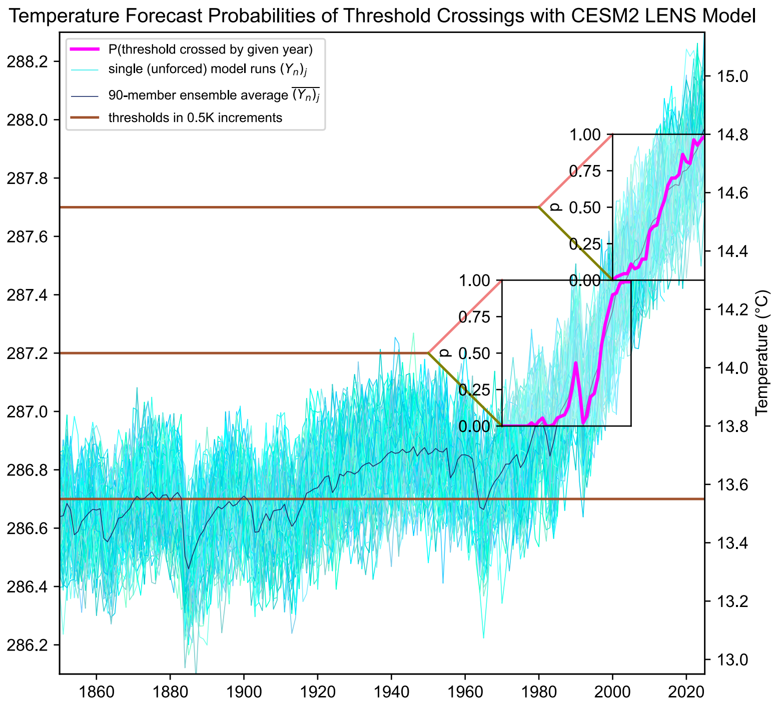


Supp. Fig. 10: Temperature forecast policy thresholds, showing a cloud of the possible next-year measurements in light blue from the simulations, and again the two inset boxes indicate the fraction of these light blue lines that have crossed the threshold.

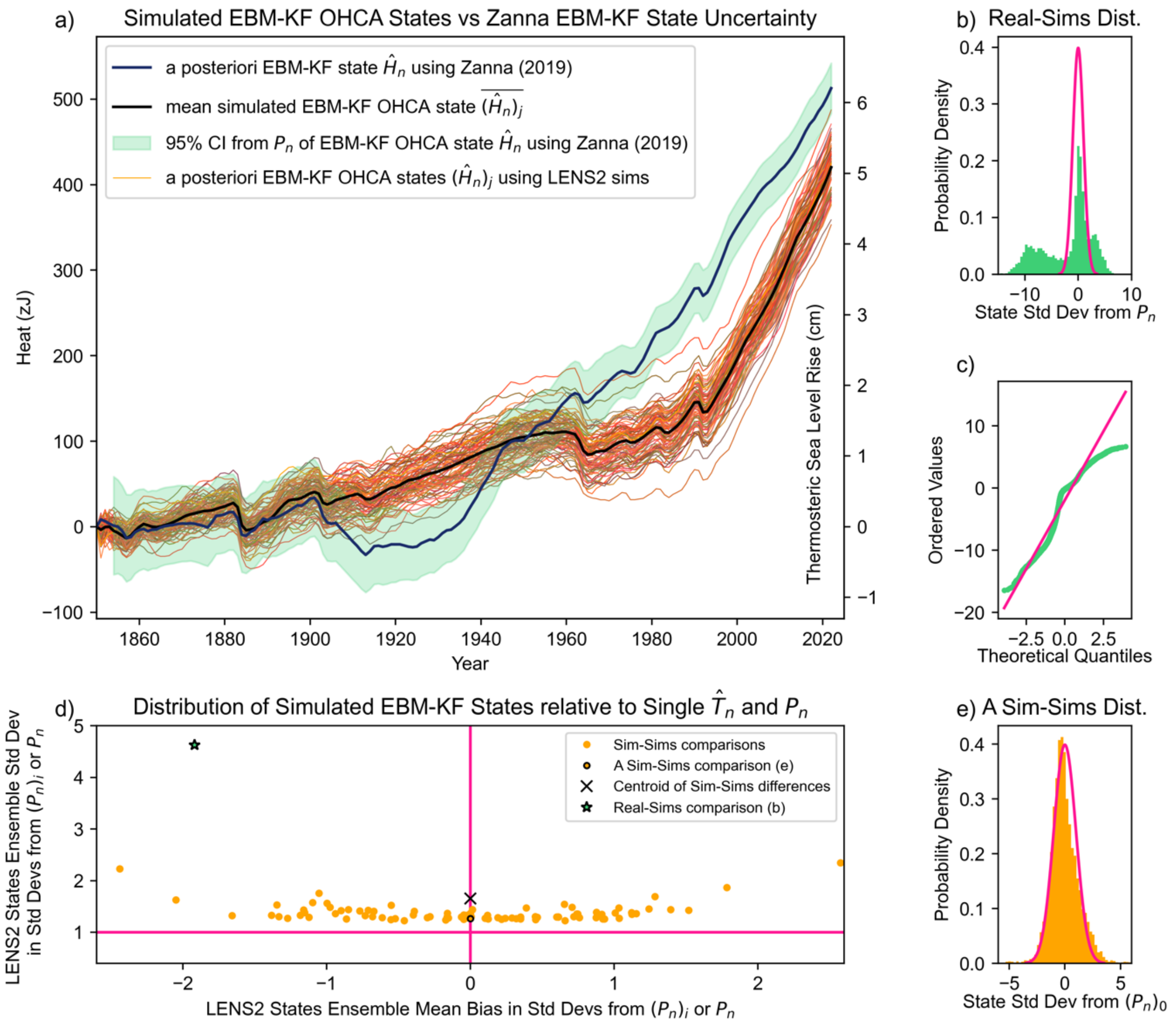


Supp. Fig. 11: As in Fig. 7, but focusing on the OHCA component rather than GMST. a) The EBM-KF *a posteriori* from Zanna (2019) state estimate (thick blue) and its 95% confidence interval (light green), along with EBM-KF state estimates for each individual CESM2 ensemble member (orange lines) and their mean (thick black line). b) The differences between the "real" measurement based Zanna (2019) climate state and all LENS2 climate states, scaled by the state standard deviation and plotted against the ideal normal distribution. This is a particularly ill-fitting distribution because the LENS timeseries of OHCA differ substantially from the Zanna (2019) observation. c) In the quantile-quantile plot, this disagreement is apparent between the "real" measurement based Zanna (2019) climate state and all LENS2 climate states of OHCA. d) Climate states and associated uncertainties arising from each of 90 LENS2 simulations and Zanna (2019) are compared to all other LENS2 climate states, and the bias and standard deviation respect to a particular $(\sqrt{P_n})_i$ of the resulting empirical distributions are plotted. e) An example of these empirical distributions is graphed, indicated by the point circled in black within the scatterplot. The expected difference across an entire simulation run between $(\widehat{H}_n)_i$ and $\overline{(\widehat{H}_n)_j}$ is $\pm 0.721(\sqrt{P_n})_i$ with range (-2.439 - 2.574), or 12.72ZJ with range (-40.47 - 42.85)ZJ.

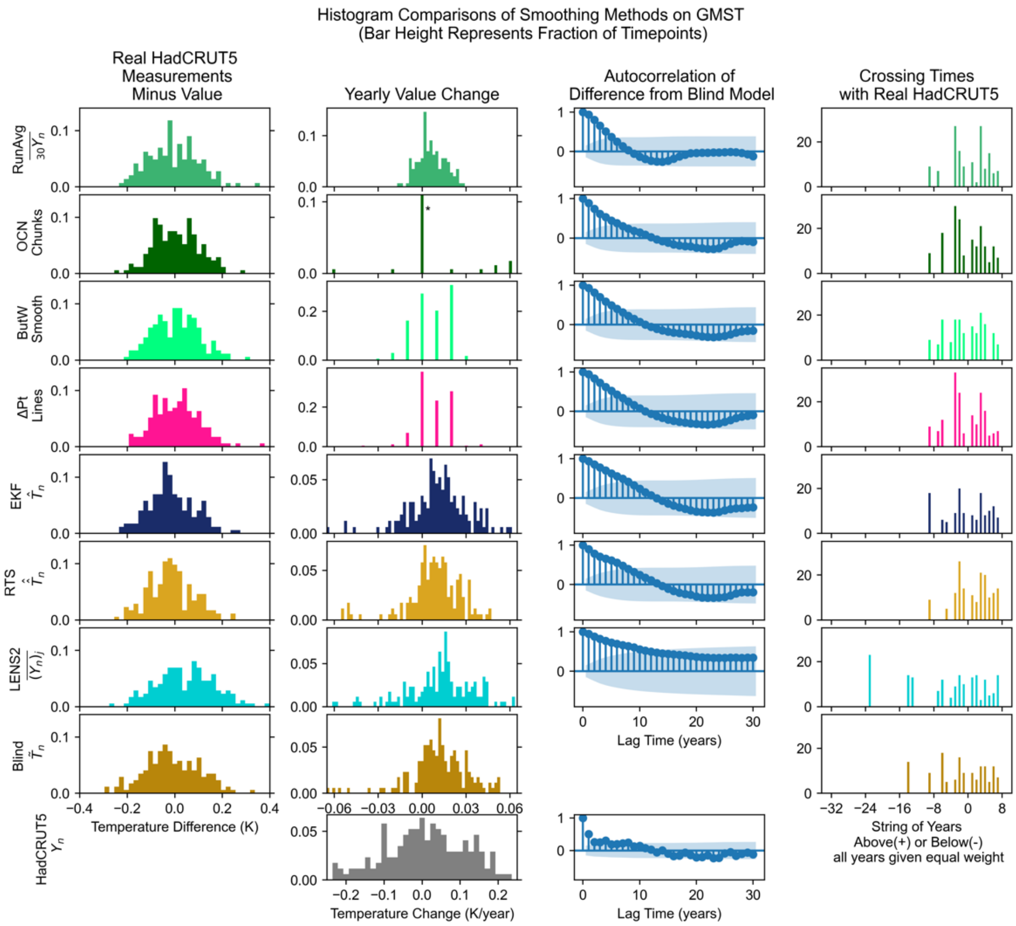


Supp. Fig. 12: Histogram comparisons of several aspects of many of the smoothing methods for generating a climate timeseries. The far-left column represents the absolute differences between the HadCRUT5 measurements and all the other models. All look similar in this respect. The center-left column shows the annual changes in the temperatures reported by each model. In this respect, the real HadCRUT5 measurements are the most spread out, because the stochastic change each year is large, whereas in most years the OCN Chunks do not change. The center-right column shows an autocorrelation plot, which demonstrates that every other model aside from HadCRUT5 (and to a lesser extent the running average) are autocorrelated with the blind energy-balance model to similar degrees. The far-right column shows how many continuous years are spent above or below HadCRUT5: both the LENS2 ensemble average and the blind energy-balance model had >20 year spans for which they were colder than the “real” HadCRUT5 data, illustrating the benefit of data assimilation.

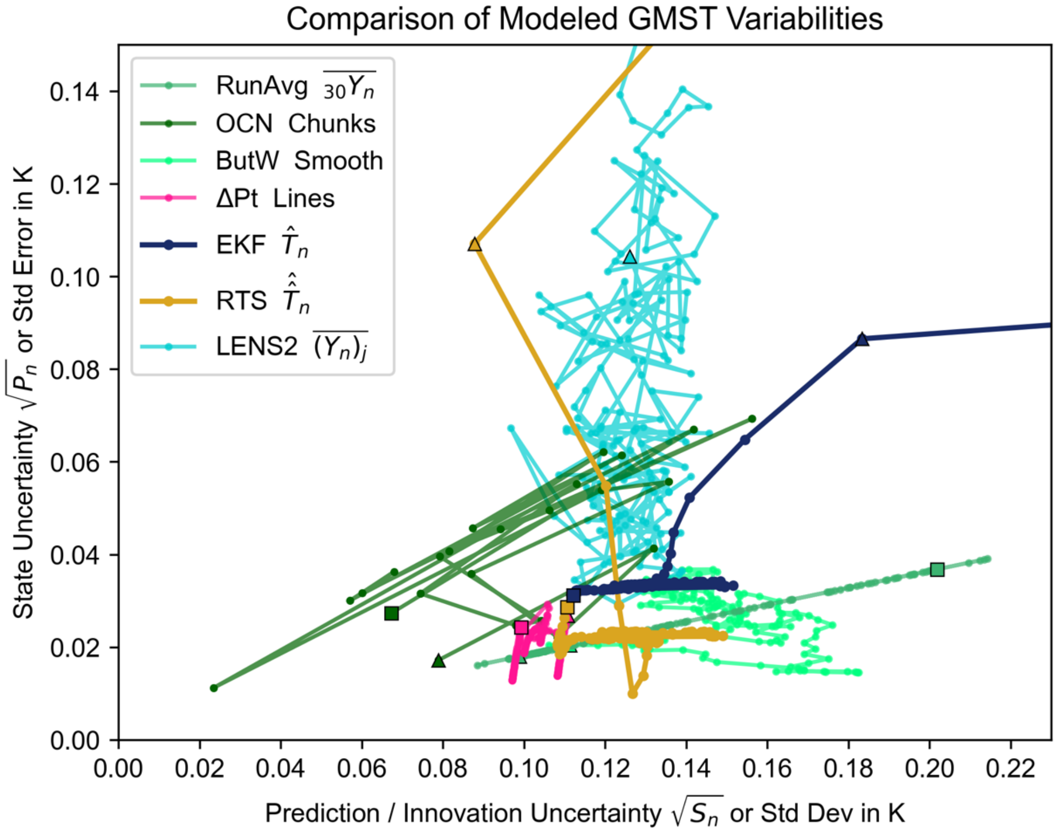


Supp. Fig. 13: Comparisons of the state and prediction (or equivalent) uncertainties of the smoothing methods for generating a climate timeseries. The x-axis represents the state uncertainty (colored light green in all other figures), and the y-axis represents the prediction uncertainty (colored light blue and doubled in all other figures). As these quantities change over time, all points in these smoothing timeseries are connected with colored lines, with the triangle △ representing the value of these quantities in 1850 or the first point that they entered the frame limits of this graph, and the square □ representing the value of these quantities in 2021 or the last point that they were within the frame limits. For instance, the running average draws a straight line because standard deviation and standard error are linearly correlated by a favor of 1/√30, and latter points have larger quantities for each variability due to the changing climate. The Butterworth Smoother traces a curve roughly in this region, with both the standard deviations and standard errors being twice the 15-year running average of the maximum of the absolute value of differences between colored and black curves. The EKF and RTS methods rapidly converge to an innovation uncertainty of 0.11-0.15K and state uncertainties of 0.034K and 0.023K respectively. The Change Point Regression variance also fluctuate the same region as the RTS, although change point method's standard error twice drops to 0.014K, and the prediction uncertainty is slightly smaller, 0.10-0.11K. Both the OCN and the LENS2 climates have standard errors that are above the other methods at most times. For LENS2, the standard deviation within the CESM2 ensemble generally remains between 0.11K and 0.14K, whereas the state uncertainty is taken to be the standard deviation of the 20 ensembles comprising CMIP6 in October 2021. (Meehl, Moss et al. 2014) These metrics are unrelated to Figure 10 in the main text. Within CMIP6, the 20 ensembles are closest to agreement in 1939, when the state uncertainty dipped down to only 0.029K between ensemble means, but this uncertainty was much greater at earlier and later time points, reaching 0.183K by 2014.

***Section C: Justification that the EKF is sufficient, will not diverge***

The issue of nonlinearity arises not in the computation of $\hat{x}_{n|n-1}=\mathrm{F}(\hat{x}_{n-1})$ but rather the covariance distribution $\mathrm{P}_n$ of points (infinitesimal probability masses) neighboring $\hat{x}_{n-1}$, which are assumed to scale linearly around this transformation to maintain a normal distribution. The OHCA part of the model can be ignored since it is purely linear. Nonlinear distortion may pile more probability density onto a state other than the transformed original projection $\mathrm{F}(\hat{x}_{n-1})$, necessitating a new computation of $\hat{x}_{n|n-1}$ as the mean of this distorted PDF. Thus, for an arbitrary point that is $z$ standard deviations away from $\hat{x}_{n-1}$, the remainder error $\mathrm{R}_1$ (Lagrange mean-value form) induced in a single cycle is:

$$\mathrm{F}\left(\hat{x}_{n-1}+z\sqrt{\mathrm{P}_n};u_n\right) - \mathrm{F}(\hat{x}_{n-1}) - \frac{\partial \mathrm{F}(x;u_n)}{\partial x} z\sqrt{\mathrm{P}_n}=$$

$$\mathrm{R}_1\left(\hat{x}_{n-1}+z\sqrt{\mathrm{P}_n}\right)=\frac{\partial^2 \mathrm{F}(\xi_\mathrm{L};u_n)}{\partial \xi_\mathrm{L}^2}\frac{\left(z\sqrt{\mathrm{P}_n}\right)^2}{2} \quad \text{for} \quad \xi_\mathrm{L}\in\left[\hat{x}_{n-1}-|z|\sqrt{\mathrm{P}_n},\hat{x}_{n-1}+|z|\sqrt{\mathrm{P}_n}\right] \tag{SC1}$$

$$=\left(\frac{0.441}{\mathrm{AOD_n}+9.73}(0.00159)-(0.00005546)(1-0.0655\log_{10}([\mathrm{CO_2}]_\mathrm{n}))1.385\left(\xi_\mathrm{L}\right)^{0.385}\right)\frac{z^2\mathrm{P}_n}{2} \tag{SC2}$$

$$-0.5(10^{-5})\, z^2\mathrm{P}_n<\mathrm{R}_1\left(\hat{x}_{n-1}+z\sqrt{\mathrm{P}_n}\right)< 0.5\,(10^{-5})\, z^2\mathrm{P}_n \tag{SC3}$$

$$\left|\mathrm{R}_1\left(\hat{x}_{n-1}+z\sqrt{\mathrm{P}_n}\right)\right|< 10^{-5}\, z^2\, 0.5\,(0.032)^2<|z|*5*10^{-9} \tag{SC4}$$

This means that all probability masses that are within $|z|< 20$ standard deviations will have an one-step error of <0.000002K. Even if the error accumulates in the same direction in each cycle of the EKF, over the 173 year timeseries, the error will be within 0.0004K compared to a particle method such as the Unscented Kalman Filter. (Julier and Uhlmann 1997; Wan and Van Der Merwe 2000)